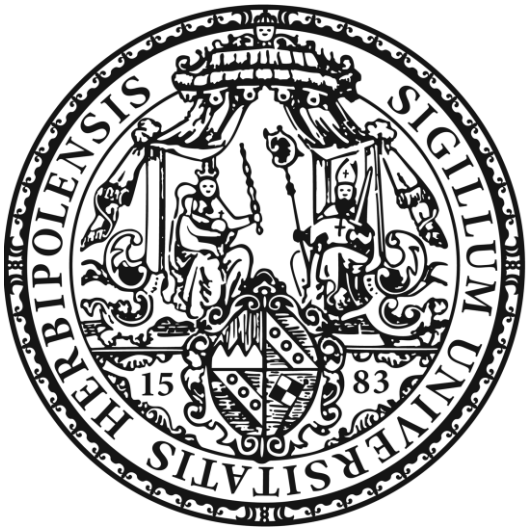

Organization and dynamics of class C GPCR nanodomains in neurons visualized by single-molecule microscopy

Visualisierung der Anordnung und Dynamik von Klasse C GPCR-Nanodomänen in Neuronen durch Einzelmolekülmikroskopie

---

Doctoral thesis for a doctoral degree

at the Graduate School of Life Sciences,

Julius-Maximilians-Universität Würzburg,

Section Biomedicine

submitted by

Sana Siddig Abdelrahman Mohamedgamil

From
Khartoum, Sudan

Würzburg**,** 2019

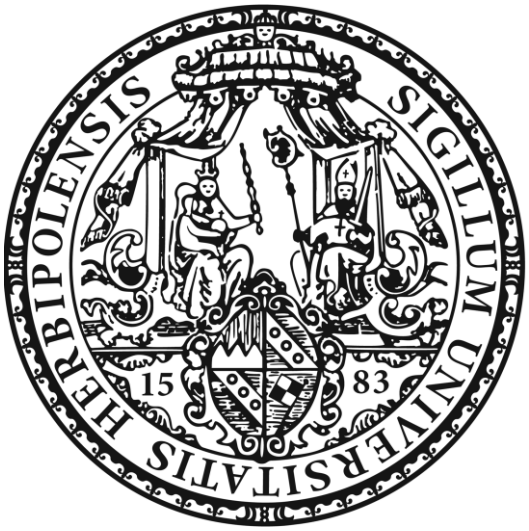

Organization and dynamics of class C GPCR nanodomains in neurons visualized by single-molecule microscopy

Visualisierung der Anordnung und Dynamik von Klasse C GPCR-Nanodomänen in Neuronen durch Einzelmolekülmikroskopie

---

Doctoral thesis for a doctoral degree

at the Graduate School of Life Sciences,

Julius-Maximilians-Universität Würzburg,

Section Biomedicine

submitted by

Sana Siddig Abdelrahman Mohamedgamil

From
Khartoum, Sudan

Würzburg**,** 2019

Submitted on: ……..……..

Office stamp

Members of the *Promotionskomitee*:

Chairperson: Prof. Alexander Buchberger

Primary Supervisor: Prof. Davide Calebiro

Supervisor (Second): Prof. Markus Sauer

Supervisor (Third): Prof. Manfred Heckmann

Date of Public Defense: ……..……

Date of Receipt of Certificates: ……

Affidavit

I hereby confirm that my thesis entitled “Organization and dynamics of class C GPCR nanodomains in neurons visualized by single-molecule microscopy” is the result of my own work. I did not receive any help or support from commercial consultants. All sources and / or materials applied are listed and specified in the thesis.

Furthermore, I confirm that this thesis has not yet been submitted as part of another examination process neither in identical nor in similar form.

Place, Date — Signature

Würzburg, 28.1.2019

Eidesstattliche Erklärung

Hiermit erkläre ich an Eides statt, die Dissertation “Visualisierung der Anordnung und Dynamik von Klasse C GPCR-Nanodomänen in Neuronen durch Einzelmolekülmikroskopie” eigenständig, d.h. insbesondere selbständig und ohne Hilfe eines kommerziellen Promotionsberaters, angefertigt und keine anderen als die von mir angegebenen Quellen und Hilfsmittel verwendet zu haben.

Ich erkläre außerdem, dass die Dissertation weder in gleicher noch in ähnlicher Form bereits in einem anderen Prüfungsverfahren vorgelegen hat.

Ort, Datum — Unterschrift

Würzburg, 28.1.2019

A picture is worth a thousand words

Ein Bild sagt mehr als tausend Worte

Contents

Abbreviations

AC: adenylyl cyclase
AChR: acetylcholine receptor
AMPA: α-amino-3-hydroxy-5-methyl-4-isoxazole-propionic acid
AZ: active zone
AKAP: A-kinase anchoring protein
β-MEA: β-mercaptoethylamine
BBE: bounding box elongation
BRET: bioluminescence resonance energy transfer
cAMP: cyclic adenosine monophosphate
CaR: calcium receptor
CAZ: cytomatrix at the active zone
CHO: chinese hamster ovary
CMV promoter: cytomegalovirus promoter
CNS: central nervous system
CRD: cysteine-rich domain
D: diffusion coefficient
DAG: diacylglycerol
DIV: days in vitro
DMEM: Dulbecco's Modified Eagle Medium
*d*STORM: *direct* stochastic optical reconstruction microscopy
D1: dopamine receptor 1
ECL: extracellular loop
EM: electron microscopy
EMCCD: electron-multiplying charge coupled device
ER: endoplasmic reticulum
fPALM: fluorescence photoactivation localization microscopy
FCS: fluorescence correlation spectroscopy
FRAP: fluorescence recovery after photobleaching
FRET: fluorescence resonance energy transfer
GABA: γ-aminobutyric acid
$GABA_BR$: γ-Aminobutyric acid subtype B receptor
GAPs: GTPase activating proteins
GDP: guanosine diphosphate

GEFs: guanine-nucleotide exchange factors

GIRK: G protein-activated inward rectifying potassium channels

GL: granule cell layer

GPCR: G protein-coupled receptor

GRKs: G protein-coupled receptor kinases

GTP: guanosine triphosphate

hAGT: human DNA repair protein O^6-alkylguanine-DNA alkyltransferase

HD: heptahelical domain

ICL: intracellular loop

IF: immunofluorescence

IME: inertia moment eccentricity

IP3: inositol 1, 4, 5-trisphosphate

KCTD: K^+ channel tetramerization-domain

K_{ir}: inwardly rectifying potassium channels

LTD: long-term depression

LTP: long-term potentiation

MAP: mitogen-activated protein

mGluR: metabotropic glutamate receptor

mGluR4: metabotropic glutamate receptor sub-type 4

ML: molecular layer

MSD: mean square displacement

NAMs: negative allosteric modulators

NMDAR: N-methyl-D-aspartate receptor

NMJ: neuromuscular junction

OBS: orthosteric binding site

PALM: photoactivation localization microscopy

PAMs: positive allosteric modulators

PBS: phosphate-buffered saline

PC: Purkinje cell

PCR: polymerase chain reaction

PF: parallel fiber

PFA: paraformaldehyde

PF-PC synapse: parallel fiber-Purkinje cell synapse

PIP2: phosphatidylinositol-4,5-bisphosphate

PKA: protein kinase A

PKC: protein kinase C

PL: Purkinje cell layer

PLC: phospholipase C

PSD: postsynaptic density

PSD-95: postsynaptic density protein 95

RET: Resonance energy transfer

RGS: regulator of G protein signaling

RIM: Rab3-interacting molecule

ROI: Region of interest

RRP: readily releasable pool

RT: room temperature

SIM: structured illumination microscopy

SM protein: Sec1/Munc 18-like protein

SMLM: single-molecule localization microscopy

SNAP-25: synaptosome-associated protein of 25 kDa

SNARE: soluble N-ethylmaleimide-sensitive factor (NSF) attachment protein receptor

SRM: superresolution microscopy

SSTR2A: somatostatin receptor type 2A SSTR2A

STED: stimulated emission depletion microscopy

STP: short-term plasticity

SV: synaptic vesicle

SYN: synapsin

TGN: trans-Golgi network

TIRF: total internal reflection fluorescence microscopy

TMD: transmembrane domain

trFRET: time-resolved fluorescence resonance energy transfer

T1R: taste receptor

VDCC: voltage-dependent calcium channels

VFT: venus flytrap domain

V2R: pheromone receptor

σ: localization precision

List of figures

List of tables

Abstract

Despite the large number of G protein-coupled receptors (GPCRs) expressed in the central nervous system (CNS), little is known about their location, organization, and dynamics in functional nanodomains at synapses. Class C GPCRs including metabotropic glutamate receptors (mGluRs) and the γ-aminobutyric acid subtype B receptor ($GABA_BR$) mediate several key functions in synaptic transmission. However, it is still insufficiently understood how these receptors function at synapses to modulate neurotransmission. One limitation is the availability of techniques to examine receptors with high spatiotemporal resolution in physiologically relevant cells. To investigate the distribution and spatiotemporal dynamics of mGluR4 and $GABA_BR$ in cerebellar slices and cultured hippocampal neurons, I used advanced imaging techniques, including single-molecule imaging and superresolution microscopy with high spatial (10-20 nm) and temporal (20 ms) resolution.

The presynaptic active zone (AZ) is a highly organized structure that specializes in neurotransmitter release. mGluR4 is a prototypical presynaptic class C GPCR. mGluR4 mediates an inhibitory effect on presynaptic glutamate release mainly via the inhibition of *P/Q type* voltage dependent calcium channels ($Ca_V2.1$). In this study, I analyzed the organization of mGluR4 at the synapse between parallel fibers and Purkinje cells in the mouse cerebellum with near-molecular resolution using two-color *direct* stochastic optical reconstruction microscopy (*d*STORM). Quantitative analyses revealed a four-fold mGluR4 enrichment at parallel fiber AZs. I found that an AZ contains 29 mGluR4 nanoclusters on average. Each nanocluster contains one or two mGluR4s, with few nanoclusters containing three or more receptors. To assess the spatial distribution of mGluR4 relative to functional active zone elements such as $Ca_V2.1$ and Munc 18-1 (an essential component of the synaptic secretory machinery), a distance-based colocalization analysis was used. The analysis revealed positive correlation between mGluR4 and both proteins at a distance of 40 nm. Interestingly, mGluR4 showed a higher positive correlation to Munc 18-1 in comparison to $Ca_V2.1$. These results suggest that mGluR4 might directly inhibit the exocytotic machinery to reduce glutamate release from the synaptic vesicles in addition to its role in the inhibition of presynaptic calcium influx. The revealed high degree of mGluR4 organization may provide a new ultrastructural basis to explain the depressive effect of mGluR4 on the neurotransmission.

Moreover, I directly imaged $GABA_BR$ dynamic behavior with high spatiotemporal resolution in living hippocampal neurons utilizing single-molecule total internal reflection fluorescence microscopy (TIRFM). To this purpose, the $GABA_{B1}$ subunit was engineered with an N-terminal

SNAP-tag to enable specific labeling with bright organic fluorophores. On the plasma membrane surface, immobile and mobile $GABA_BRs$ were detected at both synaptic and extrasynaptic compartments. A mean square displacement analysis (MSD) revealed characteristic dynamic patterns of $GABA_BR$ depending on receptor location inside or outside of the synapses. The majority of receptors belonging to the extrasynaptic pool displayed rapid and free diffusion. In contrast, approximately 80% of receptors residing at the synaptic compartments were immobile or confined within limited regions. Receptors located at pre- and post-synaptic sites showed a similar behavior. $GABA_BR$ lateral diffusion patterns inside and outside synapses might be important for the regulation of efficacy of synaptic inhibition.

Altogether, this study puts forward previously unknown GPCR nanoscopic details in functional nanodomains. GPCR spatial organization might be important for the efficiency, fidelity, and rapid signaling required for synaptic transmission.

Zusammenfassung

Trotz der großen Anzahl an G Protein-gekoppelten Rezeptoren (GPCRs) die im zentralen Nervensystem (ZNS) exprimiert werden, ist deren Lokalisierung, Anordnung und Dynamik in funktionellen Nanodomänen an Synapsen gegenwärtig weitgehend unbekannt. Klasse C GPCRs, einschließlich metabotroper Glutamatrezeptoren (mGluRs) und des γ-Aminobuttersäure-B-Rezeptors ($GABA_BR$), vermitteln einige Schlüsselfunktionen der synaptischen Übertragung. Grundlegende Prinzipien wie diese Rezeptoren an Synapsen funktionieren, um die Neurotransmission zu modulieren, sind jedoch nur unvollständig verstanden. Eine Schwierigkeit ist die Verfügbarkeit von Techniken zur Untersuchung von Rezeptoren mit hoher raum-zeitlicher Auflösung in physiologisch relevanten Zellen. Um die Anordnung und die raum-zeitliche Dynamik von mGluR4 und $GABA_BR$ in Kleinhirnschnitten und kultivierten hippocampalen Neuronen zu untersuchen, verwendete ich neue optische Verfahren wie Einzelmolekül- und hochauflösende Mikroskopie (*d*STORM) mit hoher räumlicher (10-20 nm) und zeitlicher Auflösung (20 ms).

Die präsynaptische aktive Zone (AZ) ist eine hoch organisierte Struktur, die auf die Transmitterausschüttung spezialisiert ist. Der mGluR4 ist ein prototypischer, präsynaptischer Klasse C GPCR. Hauptsächlich durch die Inhibierung spannungsgesteuerter Calciumkanäle des P/Q-Typs ($Ca_V2.1$) vermittelt mGluR4 eine inhibitorische Wirkung auf die Glutamatfreisetzung.In dieser Arbeit analysierte ich die Organisation des mGluR4 an der Synapse zwischen parallelen Fasern und Purkinje-Zellen im Kleinhirn der Maus unter Verwendung der Zweifarben direkten stochastischen optischen Rekonstruktionsmikroskopie (*d*STORM). Quantitative Analysen zeigten eine vierfache höhere Anreicherung von mGluR4 an den Parallelfaser-AZs. Ich fand heraus, dass eine AZ im Durchschnitt 29 mGluR4-Nanocluster enthält. Jeder Nanocluster enthält ein oder zwei mGluR4s, wobei wenige Nanocluster drei oder mehr Rezeptoren enthalten. Um die räumliche Verteilung von mGluR4 relativ zu funktionellen Elementen aktiver Zonen, wie $Ca_V2.1$ und Munc 18-1(ein wichtiges Protein der exozytotischen Maschinerie), zu bestimmen, wurde die Abstandsbasierte-Co-Lokalisierung-Analyse verwendet. Co-Lokalisierung wurde zwischen mGluR4 und beiden Proteinen in einem Abstand von 40 nm detektiert. Interessanterweise wurde für Munc 18-1 eine höhere positive Korrelation zu mGluR4 identifiziert. Dies deutet darauf hin, dass mGluR4, zusätzlich zu seiner Rolle bei der Hemmung des präsynaptischen Calciumeinstroms, die exozytotische Maschinerie zur Verringerung der Freisetzung von Glutamat aus sekretorischen Organellen direkt hemmen könnte. Der gezeigte hohe Grad der mGluR4-Organisation könnte

eine neue ultrastrukturelle Grundlage zur Erklärung der depressiven Wirkung von mGluR4 auf die synaptische Übertragung liefern.

Außerdem habe ich das dynamische Verhalten von $GABA_BR$ direkt mit hoher räumlicher und zeitlicher Auflösung in lebenden hippocampalen Neuronen durch Einzelmolekül-TIRFM visualisiert. Zu diesem Zweck wurde die $GABA_{B1}$-Untereinheit mit einem N-terminalen SNAP-Tag konstruiert, um eine spezifische Markierung mit hellen organischen Fluorophoren zu ermöglichen. Auf der Oberfläche der Plasmamembran wurden immobile und mobile $GABA_BRs$ in synaptischen und extrasynaptischen Kompartimenten nachgewiesen. Die mittlere quadratische Verschiebung (mean square displacment analysis (MSD)) zeigte charakteristische dynamische Muster von $GABA_BR$ in Abhängigkeit der Position der Rezeptoren innerhalb oder außerhalb der Synapsen. Die Mehrheit der Rezeptoren im extrasynaptischen Pool zeigte schnelle und freie Diffusion. Im Gegensatz dazu waren ungefähr 80% der synaptischen Rezeptoren immobile oder auf begrenzte Regionen beschränkt. Rezeptoren an prä- und postsynaptischen Stellen zeigten ein ähnliches Verhalten. $GABA_BR$- Diffusionsmuster innerhalb und außerhalb von Synapsen könnten außerdem für die Regulierung der Wirksamkeit der synaptischen Hemmung von Bedeutung sein.

Insgesamt zeigen diese Ergebnisse bisher unbekannte Erkenntnisse zu nanoskopischen Einzelheiten von GPCRs in funktionellen Nanodomänen. Die räumliche Organisation von GPCR kann für die Effizienz, Genauigkeit und schnelle Signalisierung der Neurotransmission wichtig sein.

Introduction

1.1 G protein-coupled receptors (GPCRs)

G protein-coupled receptors (GPCR) represent the largest and most versatile family of transmembrane receptors. Over 800 genes (~3% of the human genome) encode GPCR receptors. They are also known as seven transmembrane receptors because their transmembrane (TM) domain crosses the plasma membrane seven times in a snake-like configuration[1]. GPCRs mediate most actions of neurotransmitters, hormones, immune modulators, pheromones, odorants, light (photons), ions, and other stimulants to allow the cell to sense its environment[2]. Because of this broad range of stimulants, GPCRs regulate diverse physiological and biological actions where their main function is to translate an external stimulus into cellular messages. As a result of this, GPCRs are important therapeutic targets and at least 40% of all drugs currently on the market target one or more of these receptors[3].

Major discoveries within the GPCR field have been recognized and awarded with Nobel prizes. George Wald shared the prize for physiology or medicine in 1967 for groundbreaking contributions to understand the biochemistry of the photoreceptor rhodopsin[4]. Earl Sutherland won the prize for physiology or medicine in 1971 for discovering how the cyclic adenosine monophosphate (cAMP) functions as a secondary messenger to trigger hormone actions[5]. Alfred Gilman and Martin Rodbell shared the prize for physiology or medicine in 1994 for their discovery of G proteins[6]. Richard Axel and Linda Buck were awarded the prize for physiology or medicine in 2004 for discovering the gene family encoding olfactory receptors[7, 8]. Most recently, the prize for chemistry in 2012 was awarded jointly to Robert Lefkowitz and Brian Kobilka for their crucial work to reveal the basic mechanisms behind GPCR functions[2].

GPCRs are classified into six classes named from A - F based on their amino acid sequence and functional similarity. Class A (rhodopsin-like family) is the largest class and includes rhodopsin and adrenergic receptors; Class B (secretin receptor family) is regulated mostly by peptide hormones and contains receptors for secretin and glucagon; Class C (metabotropic glutamate family) is characterized by a large extracellular N-terminal domain and includes mGluRs and $GABA_BRs$; class D (fungal mating pheromone receptors); class E (cAMP receptors); class F (Frizzled/smoothened receptors)[9, 10]. All GPCRs have a common topology: an extracellular N-terminal domain, seven TM domains (termed as TM 1-7) connected by three intracellular (named as ICL 1-3) and three extracellular loops (named as ECL 1-3) and an intracellular C-terminal domain. Agonist binding to the receptor leads to structural

rearrangement mainly via the movements of TM6 as revealed by experiments conducted mainly on rhodopsin and the β_2-adrenergic receptor[11, 12, 13]. Subsequently, ligand-bound receptor activates the heterotrimeric G protein (αβγ subunits) attached to the intracellular side of the plasma membrane by promoting the exchange of the bound guanosine diphosphate (GDP) with cytosolic guanosine triphosphate (GTP). The active G protein dissociates into Gα subunit and Gβγ dimer, which both modulate multiple effectors. Recently, GPCR actions were found to be mediated not only by classical G protein-dependent mechanisms and sequential activation of second messenger pathways but also via G protein-independent mechanisms as explained in more detail in section 1.6[14, 15].

GPCR activation is terminated by hydrolysis of the GTP bound to Gα subunit to GDP, mediated by the intrinsic GTPase activity of the Gα subunit. This process is accelerated by GTPase activating proteins (GAPs) such as the regulator of G protein signaling (RGS) proteins. Gα and Gβγ subunits then re-associate to form the Gαβγ heterotrimer. GPCRs are desensitized as a result of phosphorylation by a family of kinases known as G protein-coupled kinases (GRKs)[16]. Subsequently, β-arrestin binds to the phosphorylated receptor to sterically block further G protein activation. β-arrestin also acts as an adaptor for clathrin-mediated endocytosis to reduce the number of receptors at the surface of plasma membrane[17]. Following internalization, receptors are either degraded in the lysosomes or recycled back to the plasma membrane.

1.2 Structural features, pharmacology, and signaling of class C GPCRs

Class C GPCRs are divided into four phylogenetic groups. Group I includes the calcium-sensing receptor (CaSR), the taste 1 receptors (T1Rs), and the vomeronasal receptor 2 (V2R). Group II consists of the metabotropic glutamate receptor family (mGluR1-8). Group III includes the γ-aminobutyric acid subtype B receptor B1 and B2 ($GABA_{B1-2}R$). Group IV includes several orphan receptors[18]. Class C GPCRs are distinguished by a constitutive homo-, heterodimerization at the cell surface. This leads to distinct activation modes. This subfamily is also characterized by a large extracellular N-terminal domain (~ 600 residues), that harbors the agonist binding domain[19].

The first domain is the extracellular N-terminal domain. It is composed of two parts: the ligand-binding domain or orthosteric binding site (OBS) – also called Venus flytrap domain (VFT) – and the cysteine-rich domain (CRD). In contrast to members of class C GPCRs, $GABA_BRs$ lack the CRD[20]. The VFT is composed of two lobes and the agonist binding takes place in the cleft between these two lobes[21]. The VFT resembles domains found in the ligand-gated ion

channels and tyrosine kinase receptors[22]. Due to the VFT structural similarity between mGluR and the CaSR, some of the mGluRs were found to be activated/regulated by divalent cations (Ca2+, Mg2+) in the absence of glutamate[23].

The second domain is the TM domain. The VFT is connected to the TM domain via the CRD. Agonist binding leads to a structural rearrangement (conformational change) which is transmitted to the intracellular side via the CRD and the TM domain and subsequently activates G proteins. G proteins mainly interact with the second intracellular loop of the receptor[24, 25].

The third domain is an intracellular C-terminal domain. Enzymes, ion channels and receptors interact with the C-terminal domain to modulate the receptor function. Scaffolds and cytoskeleton proteins bind to this domain as well to anchor the receptors at certain compartments[26]. Additionally, alternative splicing takes place in this region to encode receptor variants [27].

I will discuss in further detail mGluRs and $GABA_BRs$ because they are the focus of this work. mGluRs are the metabotropic receptor targets for glutamate, the major excitatory neurotransmitter in the CNS[27, 28, 29]. mGluRs are encoded by multiple genes with several splice variants. They are sub-classified into three groups based on sequence homology, susceptibility to pharmacological ligands, and their preferred second messenger system. Group I receptors (mGluR1/mGluR5) are specifically activated by 3,5-dihydroxyphenylglycine (3,5-DHPG) and generally have a positive modulatory effect on neurotransmission. Active receptors couple to Gq/11 and activate phospholipase C (PLC). PLC catalyzes the hydrolysis of phosphatidylinositol-4, 5-bisphosphate (PIP2) to inositol 1, 4, 5-trisphosphate (IP3) and diacylglycerol (DAG) This cascade eventually releases the intracellular calcium and activates the protein kinase C (PKC), respectively[30]. Group I mGluRs also couple to Gs, leading to an increase in cAMP production. Alternative pathways, such as activation of the MAP/ERK pathway by group I receptors, were also described in several studies[31, 32, 33]. Group II (mGluR2/3) and group III receptors (mGluR 4/7/8) have negative effects on synaptic transmission and couple to Gi/o, leading to less cAMP production via inhibition of adenylyl cyclase (AC). Additionally, the Gβγ dimer released upon receptor activation regulates the ion channels by inhibiting voltage-dependent calcium channels (VDCC) and activating G protein-activated inward rectifying potassium (GIRK) channels [34, 35]. An exception within group III is mGluR6, which is expressed exclusively in retinal bipolar cells and regulates synaptic transmission[36]. Members of group II and III are activated by LY379268 and L-2-amino-4-phosphonobutyrate, respectively.

$GABA_BR$ is a model group III GPCR; it is a metabotropic receptor target for GABA that modulates synaptic transmission, signal propagation, and plasticity[37, 38]. $GABA_BR$ is an obligatory heterodimer formed of $GABA_{B1}$ ($GABA_{B1}$ exists in two isoforms $GABA_{B1a}$ and $GABA_{B1b}$) and $GABA_{B2}$ subunits and four auxiliary K^+ channel tetramerization-domain (KCTD) proteins (named KCTD 8, 12, 12b, and 16)[37]. The heterodimerization of $GABA_{B1}$ and $GABA_{B2}$ subunits is necessary for the formation of functional receptor and for the receptor trafficking to the plasma membrane. This is because $GABA_{B1}$ subunit bears the agonist-binding site at its N-terminal domain but it cannot couple to G proteins. On the other hand, $GABA_{B2}$ subunit cannot bind GABA yet it couples to Gi/o and mediates signal transduction[39]. $GABA_{B1}$ subunit carries an endoplasmic reticulum (ER) retention motif (RXRR) at its C-terminal domain, which prevent the escape of the unassembled subunit from the ER. The assembly of $GABA_{B1}$ and $GABA_{B2}$ subunits via the C-terminal coiled-coil domains is necessary to mask the ER retention motif, allowing the plasma membrane insertion of the functional receptor[40, 41, 42]. KCTD proteins stabilize G protein binding and control signaling kinetics. $GABA_BR$ inhibits the neurotransmitter release by Gβγ subunit mediated inhibition of VDCC. Gβγ also activates GIRK channels to generate slow inhibitory postsynaptic potentials[43, 44, 45]. $GABA_BRs$ are also negatively coupled to cAMP production via AC pathway.

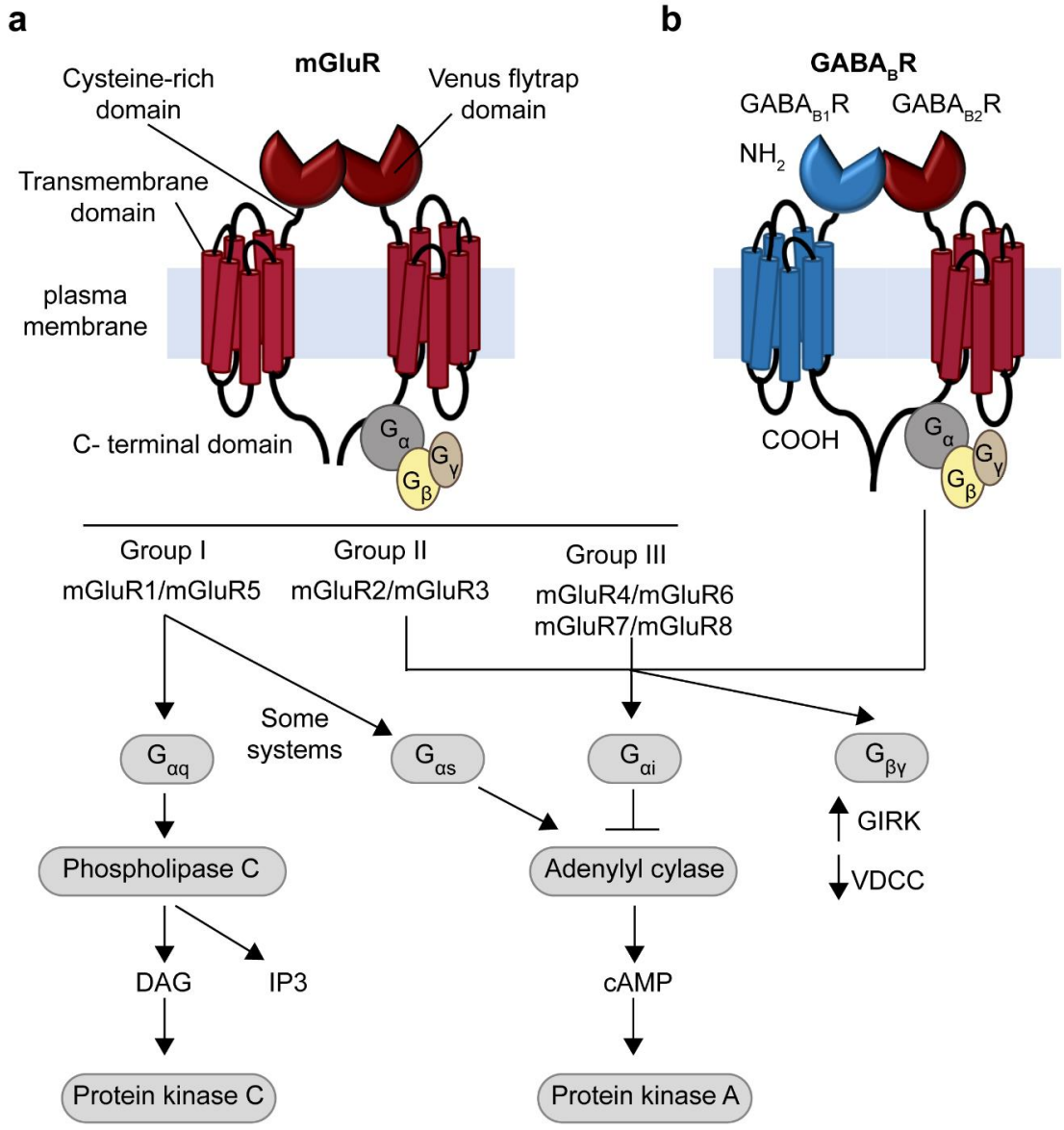

Figure 1: Schematic diagram showing the general structure of class C GPCRs (mGluR and GABA$_B$R) and their signaling cascades. The large extracellular N-terminal domain of class C GPCRs is composed of a Venus flytrap domain and Cysteine-rich domain, a transmembrane domain spanning the plasma membrane 7 times, and an intracellular C-terminal domain. The figure also describes the classification and signaling pathways of **(a)** mGluRs and **(b)** GABA$_B$R.

1.3 Oligomeric state of class C GPCRs

It is highly debated whether GPCRs are present at the cell surface as monomers, dimers, or higher order oligomers and how this special organization might be related to the receptor function[46]. Regarding class A GPCRs, it has been hypothesized that they exist in a dynamic equilibrium between monomeric and dimeric forms and the receptor treatment with an agonist may shift this equilibrium[47, 48]. On the other hand, Class C GPCRs exist as constitutive homo- and/or heterodimers and can potentially form dynamic tetramers or higher order oligomers[49]. Therefore, they represent an interesting model to study GPCR dimerization/oligomerization.

Receptors of class C GPCRs form hetero- or homodimers by association of two non-identical or identical subunits, respectively. $GABA_B$Rs and T1Rs heterodimers are not covalently linked and heterodimerization is a prerequisite for signaling and the receptor trafficking to the cell surface[42, 50, 49]. Homodimerization of mGluRs and CaSRs is believed to be induced by the intermolecular disulfide bond formed between the lateral CRDs in two adjacent receptors[51, 52, 53, 54]. An additional level of complexity is added by the possibility of heterodimerization among different mGluRs, as verified by time-resolved FRET performed on SNAP/CLIP-tagged mGluRs expressed in a mammalian cell line[55]. In the case of mGluR heterodimers, studies suggest that electrostatic interactions between the intracellular domains of adjacent subunits is suggested to be the general mechanism for the heterodimerization[56]. It is still under intense debate whether the binding of glutamate to just one receptor is sufficient to initiate the receptor signaling. Some reports verified that glutamate binding to both dimer subunits is an absolute requirement and the dimeric protein architecture is necessary for signaling by the endogenous agonist glutamate[57, 58]. Meanwhile, there is evidence showing that a disulfide bond between dimers is not necessary for G protein activation and the mGluR heptahelical domains (HD) can couple G proteins behaving similarly to the rhodopsin-like receptors[58]. In contrast, binding of GABA to the $GABA_{B1}$ subunit is sufficient for proper signaling[59]. It is suggested that different GPCRs form dimers with different interfaces[60, 61, 62, 63]. A recent report has shown that there are multiple interfaces for transient dimers of neurotensin receptor 1 providing evidence for the dynamic regulation of receptor signaling[64].

Various methods were applied to study GPCR oligomerization. The resonance energy transfer (RET) and single-molecule microscopy are the most convenient and popular. Maurel et al. used time-resolved FRET (trFRET) on SNAP-tagged receptors expressed in HEK 293 cells. He reported that the mGluRs and $GABA_B$Rs assemble into dimers and dimers of dimers, respectively[65]. A single-molecule TIRFM study performed on SNAP-tagged receptors confirmed these findings. Calebiro et al. reported that $GABA_B$Rs are organized in the form of

dimers and tetramers of heterodimers when expressed at physiological levels. Moreover, real-time tracking of the receptors showed that agonist stimulation did not change the receptor oligomeric state[47]. The $GABA_BR$ oligomers are formed through assembly of the extracellular domains of $GABA_{B1}$ subunits of heterodimers[66]. The formed oligomers are stable and do not dissociate upon insertion of new $GABA_BRs$ to the surface of transfected cells[66].

There are very few reports of experiments conducted on native tissues with any functional consequences of receptor oligomerization. For instance, Moller and his colleagues showed that mGluR2 is a strict homodimer while $GABA_BR$ forms larger complexes of heterodimers in hippocampal neurons[67]. Moreover, there is evidence by trFRET showing that $GABA_BR$ forms higher order oligomers in the brain[68]. The functional consequence of $GABA_BR$ oligomerization is a reduction in the coupling efficiency, as the $GABA_BR$ tetramers had lower G protein coupling efficacy in comparison to heterodimers. Interestingly, in a study based on Western blot, the authors showed differential mGluR1 and mGluR5 monomeric and dimeric expression profiles following phencyclidine (NMDA receptor antagonist) treatment. These samples were obtained from neurodevelopmental model of schizophrenia in rats[69]. The authors suggested that the monomeric and dimeric states of group I mGluRs might be important during neuronal development and the development of schizophrenia[69].

1.4 Synaptic transmission

Synaptic transmission is necessary for signal propagation from the presynaptic neuron to the postsynaptic neuron. In chemical transmission, signals are received at presynaptic neurons in the form of action potentials, then this electrical message is transmitted to the postsynaptic neurons via chemical signals (neurotransmitters)[70]. Neurotransmitters are stored within synaptic vesicles (SVs) (~ 5000 molecules per SV) and subsequent exocytosis takes place exclusively at the presynaptic terminal AZs. The arrival of an action potential causes membrane depolarization and triggers Ca^{2+} influx via the VDCC. The concept that calcium functions as an intracellular messenger to achieve the coupling between action potentials and neurotransmitter exocytosis was introduced by Katz and his colleague in 1969[71]. Increased calcium concentration provokes events that cause docking, priming, and finally fusion of SVs to the plasma membrane of presynaptic neurons. As a result of this, neurotransmitters are released from the SVs to the synaptic cleft (~ 100 nm wide)[72, 73, 74]. VDCCs exist in a close proximity to sites where neurotransmitter exocytosis takes place. Via these channels, calcium ions influx and generate microdomains of high Ca^{2+} concentration (~ 100 µM or higher) in comparison to the rest of the presynaptic cytosol (100 nM). Therefore, there is only a 0.2 ms delay between calcium ions entry and the synaptic vesicle fusion[75].

The first step of synaptic vesicle maturation is docking, which is defined as the alignment of SVs and the presynaptic neuron to prepare for fusion. Rab3 guides SVs to the AZ. Then, synaptobrevin (SV protein) and syntaxin-1 (presynaptic plasma membrane protein) recognize each other and facilitate the docking of SVs. In the second step, which is known as priming, the docked SVs become fusion-competent. It is believed that the (soluble N-ethylmaleimide-sensitive factor (NSF) attachment protein receptor) SNARE is essential for priming and fusion[76]. A favorable model is that energy released by formation of SNARE high-affinity complex is used to provide the driving force required for priming via NSF-driven hydrolysis of ATP[77, 78]. SNARE is composed of three proteins: synaptobrevin, syntaxin-1, and synaptosome-associated protein of 25 kDa (SNAP-25) and forms four coiled-coil domains. Munc 18-1 plays complementary roles to SNARE proteins to drive exocytosis. It is suggested to have two roles: the first role is inhibitory, where it interacts with syntaxin-1 to inhibit premature SNARE complex assembly[79, 80]. The second role, is to prevent SNARE protein dissociation by helping in maintaining the correct orientation for fusion. This theory is supported by reports showing complete neurotransmitter release blockage phenotype in Munc 18-1 knockout mice[81, 82]. Third step is fusion: a second calcium influx leads to the pulling of the lipid bilayers of SV and AZ plasma membranes to form a small hydrophilic pore, similar to a gap junction, which then dilates to allow exocytosis. The calcium sensor protein, synaptotagmin, is an essential SV plasma membrane protein for SV fusion and is activated by the calcium influx[83]. Synaptotagmin is not involved in the actual fusion events but it assists in pulling SVs and presynaptic plasma membranes within close proximity and triggers conformational changes in SNARE. In the absence of calcium, synaptotagmin inhibits the pore formation by acting as a clamp[84].

The released neurotransmitters bind to receptors located on the postsynaptic neuron to open or close ion channels inducing excitatory or inhibitory postsynaptic potentials. Receptors for the released neurotransmitters are organized and anchored on the plasma membrane of the postsynaptic neuron via interactions with a scaffolding meshwork known as the post synaptic density (PSD)[85, 86].

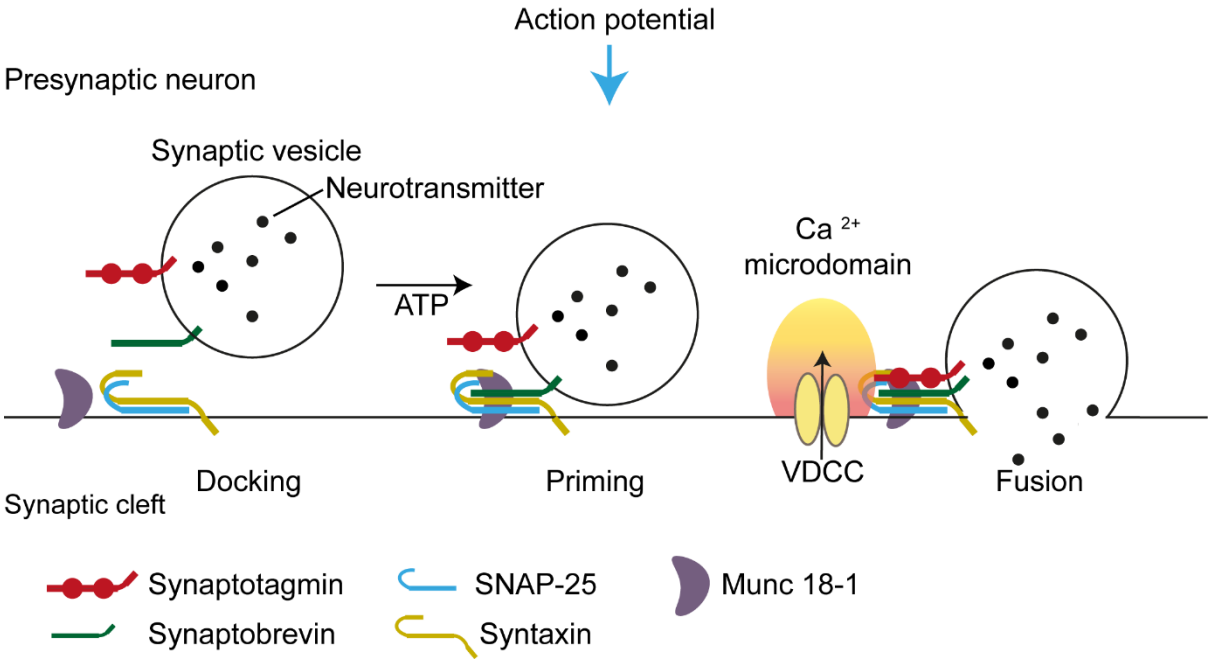

Figure 2: Schematic representation of vesicle docking, priming, and fusion at the presynaptic plasma membrane. The arrival of action potential leads to recruitment of SVs at the AZs in a process called docking. SNARE complex pulls the synaptic vesicle and presynaptic plasma membranes in close proximity. Subsequently, SVs are primed to prepare for the release of neurotransmitters. A calcium microdomain is formed around open calcium channels in the vicinity of exocytosis sites. Finally, calcium influx triggers the formation of the fusion pore between the primed SV and the presynaptic plasma membranes to release stored neurotransmitters into the synaptic cleft.

1.5 The presynaptic active zone (AZ)

The presynaptic active zone (AZ) is a specialized structure on the cytoplasmic side of presynaptic neuron terminals where synaptic vesicles (SVs) are released and calcium channels are anchored[87]. The AZ faces the postsynaptic neuron that harbors postsynaptic receptor clusters. Electron microscopy (EM) has revealed that AZs consist of a dense protein structuer[88]. AZ morphological features vary among species, between different synapses, and even between the same neuron forming synapses with other types of neurons[89]. Each presynaptic neuron contains one to four AZs[90] and each AZ is composed of: the plasma membrane, the presynaptic dense projections, and the cytomatrix at the active zone (CAZ). In vertebrate central synapses, the AZ has a disc-like shape that is 200 - 500 nm in diameter with pyramid-like dense projections into the cytosol where synaptic vesicles are tethered[91, 92, 93]. AZs of the neuromuscular junction (NMJ) adopt a more elongated shape (1000 – 2000 nm) with its long axis parallel to the presynaptic membrane and the synaptic vesicles are attached

through ribs to the beams[94]. In the NMJ of the Drosophila, synaptic vesicles cluster around more elaborated T-shaped dense projections[95, 96]. Similarly, the ribbon synapse found in the visual and auditory systems of vertebrates has a large dense projection (ribbon body) that is located perpendicular to the plasma membrane[97]. The function of the large T-shape and ribbon body dense projections is to increase the readily releasable pool (RRP) by increasing the number of tethered synaptic vesicles. Subsequently, this facilitates sustained transmitted release over long time periods[97, 98]. Vertebrate CNS synapses and NMJs have smaller size dense projections (less than 100 nm); therefore, they are considered as CAZ[98].

The main function of the AZ is to facilitate the conversion of neuronal information as action potential into chemical message via neurotransmitter release. It has additional important functions such as the priming and docking of SVs, recruitment of voltage-dependent calcium channels (VDCCs) to the AZ for efficient excitation coupling, alignment of pre- and postsynaptic elements via the trans-synaptic cell-adhesion molecules, and regulation of short- and long-term presynaptic plasticity.

The primary constituents of the AZ include but may not be limited to rab3-interacting molecule (RIM), mammalian uncoordinated-13 (munc 13), bassoon/piccolo, ELKS, and Liprin-α. Some of these proteins are expressed in non-neuronal cells such as secretory cells, suggesting that they have additional functions[99, 100]. However, the entire and comprehensive molecular architecture of AZ proteins has not yet been fully revealed. RIM proteins are scaffolding proteins expressed ubiquitously at the presynaptic neurons. They have a central role in connecting AZ proteins to each other. They interact directly with rab3 and munc-13 to mediate SV fusion[101]. RIM proteins also promote VDCC accumulation at the AZ[102] via the PDZ-domain of RIM[103]. They play an important role for docking and priming SVs[104] in addition to their role in short-term plasticity (STP) and long-term potentiation (LTP)[105, 106]. Munc 13 has an essential role for priming SVs by enabling syntaxin-1 to form the SNARE complex. It mainly catalyzes the alteration of the closed syntaxin-1 complex with Munc 18-1 to the open syntaxin-1 conformation to allow SNARE complex assembly[107]. It also has important role in mediating presynaptic short-term plasticity (STP)[108]. Bassoon and Piccolo are very large multidomain scaffolding proteins that are structurally related. They recruit and tether clusters of SVs near AZs[109]. Bassoon deletion causes synapses inactivation, while the loss of Piccolo has no significant effect on synapse formation and neurotransmitter release[109, 110].

Furthermore, the membrane fusion machinery soluble SNARE and SM proteins are located at the AZ and they play a complementary in SV fusion. However, they are not exclusively located at the AZ but rather distributed over the plasma membrane due to their involvement in multiple types of exocytosis[111].

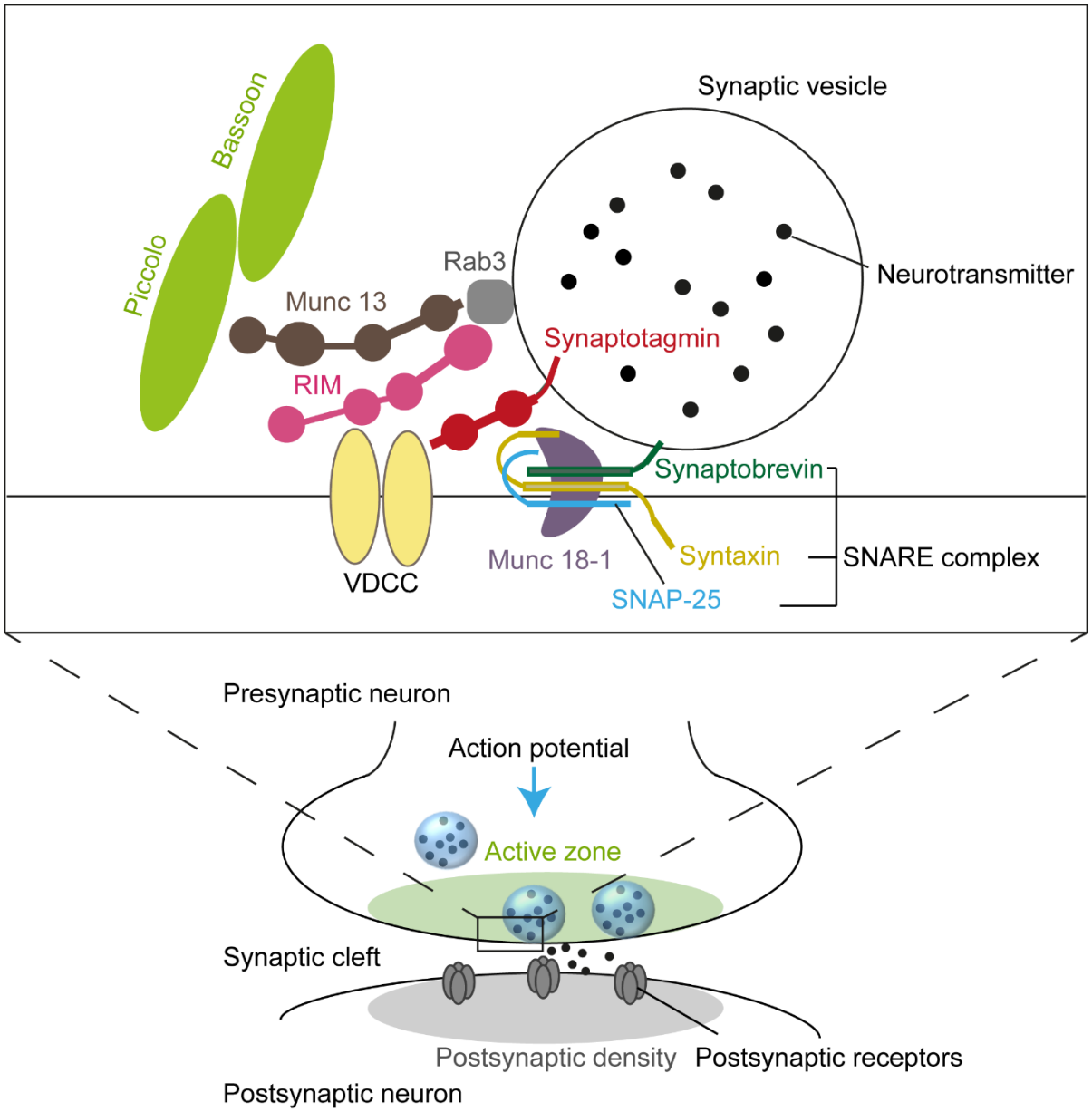

Figure 3: Schematic representation of the active zone (AZ) in a synapse and a molecular model of its main constituents. The active zone has a disc-like shape in vertebrate central synapses located at the presynaptic terminal, opposite to postsynaptic receptors cluster. Synaptic vesicle exocytosis takes place in the near vicinity of VDCC. Enlargement of the boxed region shows main AZ proteins. RIM has central role in connecting AZ proteins: it binds to VDCC via its PDZ domain and it also interacts physically with Munc 13 and Rab3. The SV protein synaptotagmin is Ca^{2+} sensor for exocytosis. The scheme also depicts the SNARE complex which is composed of the three proteins synaptobrevin, syntaxin-1, and SNAP-25. Munc 18-1 has a complementary role to SNARE complex to mediate exocytosis. Bassoon and Piccolo are large scaffolding proteins important for tethering SVs to the AZ. SV: synaptic vesicle, VDCC: voltage-dependent calcium channel.

1.6 Role of GPCRs in the regulation of synaptic transmission

GPCRs located pre- and postsynaptically are key players in modulating synaptic transmission via complex mechanisms which are still a matter of intense debate. GPCRs are reported to function through means other than the classical G protein-dependent paradigm[15]. Those G protein-independent mechanisms are not well understood especially in the context of neuronal cells[14].

(a) G protein-dependent mechanisms:

Many GPCRs mediate regulation of synaptic transmission via activation of the heterotrimeric G proteins. Upon GPCR activation, the Gβγ dimer dissociates from the α-subunit. Ion channels and exocytotic machinery proteins are regulated directly by Gβγ dimers and/or indirectly via Gα-subunits that modulate second messengers to activate or inhibit several intracellular enzymes. In this section I will explain main mechanisms behind Gβγ- and Gα-subunit signaling.

a.1. Gβγ signaling

One of the established mechanisms behind GPCR-mediated regulation of synaptic transmission is via Gi/o-proteins-coupled to auto- and heteroreceptors such as mGluRs, $GABA_BRs$, M2/M4 muscarinic receptors, μ/δ opioid receptors, and α2-adrenergic receptors. The released Gβγ dimer upon activation can act via two main mechanisms:
The first and most ubiquitous mechanism is the inhibition of VDCCs (mainly the Ca_V2 subfamily) presynaptically and the activation of G protein-activated inward rectifying potassium (GIRK) channels postsynaptically via direct interaction with the Gβγ complex[112]. This mechanism is known as “membrane-delimited modulation” because it involves a Gβγ subunit that is anchored to the plasma membrane rather than diffusing via an intracellular pathway[113]. VDCCs are essential in modulating synaptic exocytosis. Their activation upon depolarization leads to an increased influx of calcium ions that is required to provoke exocytosis. GPCR modulation of presynaptic VDCCs have a crucial effect on neurotransmitter release. Direct Gβγ subunit inhibition of VDCC is fast and is known as voltage-dependent inhibition. The main two VDCC subfamilies regulated by direct Gβγ inhibition are the *P/Q-type* ($Ca_V2.1$) and *N-type* ($Ca_V2.2$) VDCCs which are expressed presynaptically. On the other hand, other VDCC subfamilies are not regulated via direct Gβγ inhibition[114]. As an example, $GABA_BR$ agonist baclofen was found to strongly reduce Ca^{2+} current via the inhibition of presynaptic $Ca_V2.1$ mediated by the release of Gβγ subunit at auditory brainstem synapses[115]. Similarly, Ca^{2+} current was inhibited upon stimulating A1 adenosine receptor by adenosine in mossy

fiber terminals in the hippocampus. Gβγ inhibition of $Ca_v2.1$ and $Ca_v2.2$ was responsible for this inhibition[116]. The VDCC is composed of the α1 core forming subunit, intracellular β subunit, disulfide linked transmembrane α2δ complex subunit, and additionally a transmembrane γ subunit at some tissues[117]. The molecular mechanism behind Gβγ inhibition of Ca^{2+} influx is not yet understood; but most likely, G proteins bind to VDCCs in order to render them more resistant to opening[118]. Gβγ is thought to modulate VDCC via binding to the N-terminal, I-II linker, and the C-terminal of the α1 pore forming subunit[119]. GIRK channels on the other hand are members of the inwardly rectifying potassium channels (K_{ir}) that are regulated by GPCRs. Active Gβγ complexes activate postsynaptic GIRK channels to facilitate potassium ion efflux out of the neuron, leading to hyperpolarization[120, 121]. For instance, GIRK channels are activated by direct interaction with a Gβγ dimer released as a consequence of opioid receptor activation[122]. It is reported that Gβγ binds directly to the GIRK channel at its N-terminal domain, as well as the 273-462 amino acid residues at the C-terminal[123].

A second novel mechanism underlying Gβγ signaling is via regulation of neurotransmitter release from SVs. This typically happens through interruption of SNARE protein zippering, which is required for vesicle fusion. Several reports gave convincing evidence that Gβγ dimer interacts directly with exocytotic machinery proteins such as SNAP-25, syntaxin-, and synaptobrevein [112, 124]. *In vitro* studies showed that the Gβγ complex binds to the C-terminal of the SNAP-25. The authors suggested that Gβγ and synaptotagmin compete for binding to the C-terminal of the SNAP-25. Hence, Gβγ inhibits exocytosis mainly via preventing SNARE -synaptotagmin complex formation[124].

a.2. Gα signaling

As some GPCRs are located outside of the active zone, they might act primarily through the activation of Gα subunit[125]. Gα signaling regulates the phosphorylation state and activity of ion channels and other proteins involved in exocytosis indirectly via second messengers. The G proteins are classified into four main categories based on their sequence similarity to: Gs, Gi/o, Gq, and G12/13. Gαq mainly activates the PLC pathway. Whereas, Gαs and Gαi/o subunits stimulate or inhibit the activity of AC pathway, respectively to modulate cyclic AMP production and protein kinase A (PKA) activity[126]. Gα12/13 couples to the Rho guanine-nucleotide exchange factors (GEFs) activation.

GPCR-mediated regulation of VDCC occurs in a slow voltage-independent manner by second messengers such as kinases and phosphatases. This type of modulation is considered voltage-independent because strong membrane depolarization cannot reverse its action and it is slower than the voltage-dependent Gβγ mediated regulation due to the involvement of intermediate enzymes. For instance, activation of D1 dopamine receptor (which is coupled to

Gαs-protein) activates PKA. Active PKA phosphorylates protein phosphatase 1 that eventually dephosphorylates $Ca_v2.1$ and $Ca_v2.2$, leading to voltage-independent current inhibition[127]. Additionally, Gαq-coupled M1 muscarinic receptors were reported to inhibit $Ca_v2.2$ via PLC activation which sequentially hydrolyses PIP2 required for VDCC stabilization[128, 129].

VDCCs might be regulated simultaneously by the voltage-dependent and voltage-independent mechanisms. For example, $Ca_v2.2$ channel is regulated by neurokinin receptor 1 via both Gβγ and Gαq subunits[130].

As mentioned above GPCRs modulate synaptic transmission also via regulation of proteins involved in SV recruitment, docking, priming, and exocytosis via Gα activation. GPCRs main effectors are AC and PKA; these two enzymes phosphorylate SV release machinery components as reviewed in Brown et al.[131]. For example, the glutamate release from cerebrocortical nerve terminals is enhanced by cAMP-dependent PKA activated by β-adrenergic receptor[132].

(b) G protein-independent mechanisms:

Newly emerging investigations report a number of alternative mechanisms for GPCR signaling apart from the classical G protein-dependent mechanisms, such as: GPCR proximity to its effectors, signaling via β-arrestins, and interaction of GPCRs with PDZ domain scaffolding proteins.

b.1. GPCR proximity to effectors

Currently, there is substantial evidence showing that GPCRs do not exist in isolation floating in a homogenous membrane but rather they form dynamic macromolecular complexes with their cognate G proteins and effectors, such as ion channels and/or enzymes in defined microdomians[121, 122, 133, 134, 135]. Local Ca^{2+} signals produced by the opening of calcium channels are limited from tens up to hundreds of nanometers away from source channels (calcium nanodomain) within both presynaptic active zones and postsynaptic densities[136]. Thus, GPCRs are likely to be strategically arranged with respect to ion channels via direct or indirect interactions. This macromolecular arrangement might be important to guarantee specific, efficient, and rapid signaling as the molecules will not be slowed down by the burden of diffusion. For instance, some opioid and dopamine receptors were found to associate physically with $Ca_v2.2$. The authors suggested that GPCRs in this case regulate the ion channel density by enhancing channel trafficking to reach the cell surface[137, 138, 139]. Direct interaction between the C-terminal domains of mGluR1 and $Ca_v2.1$ was also reported and the

authors gave convincing evidence that this heteromeric complex is important for the temporal regulation of $Ca_v2.1$[135].

Recently, emerging reports show that GPCRs might also interact directly (in a G protein-independent manner) with exocytotic machinery elements to modulate their functions. Ramos et al. showed that native mGluR4 directly interacts with Munc 18-1 in cerebellar extracts and they suggested that mGluR4 might depress the neurotransmitter release not just by inhibition of calcium influx but also by sequestering exocytosis proteins in a G protein-independent fashion[140].

b.2. β-arrestins and c-Src kinase signaling

β-arrestins mediate GPCR internalization and it is suggested that it can initiate a variety of G protein-independent pathways[141]. G protein-coupled receptor kinases (GRK) phosphorylate GPCRs bound to agonists, leading to different phosphorylation barcodes. The β-arrestins bind to the receptor at its phosphorylated cytoplasmic surface to desensitize GPCRs by blocking further interaction with G proteins. β-arrestin also regulates GPCR trafficking where it functions as an adaptor/scaffold for c-Src to regulate GPCR internalization by stimulating tyrosine phosphorylation of dynamin (a GTPase required for internalization)[142]. Furthermore, it is reported that β-arrestin shifts GPCR signaling from traditional G protein-dependent pathway towards c-Src non-receptor tyrosine kinase signaling which is a potent stimulator of the mitogen-activated protein (MAP) kinase pathway[143, 144]. As an example, β2-adrenergic receptor was found to activate ERK1/2 in G protein independent manner via β-arrestin in GαS null cells expressing β2-adrenergic receptor mutants that do not couple to G protein[145].

b.3. Interaction with PDZ domain containing scaffolding proteins

Recently, many GPCRs were reported to interact with adaptor/scaffolding proteins to facilitate interactions with their effectors, mediate receptor specificity, and to determine the receptor location and organization at the plasma membrane. GPCRs have a long C-terminal where interactions with many proteins take place. PDZ domain containing proteins recognize variable motives at the C-terminal and bind to it. For instance, homer, which is a PDZ containing mammalian scaffolding protein, was reported in literature to interact directly with the proline-rich motif (PPXXFr) identified at the C-terminal domain of group I mGluRs (mGluR1/mGluR5). Homer regulates the organization of receptor clusters at the plasma membrane and enhances the signaling efficiency[146, 147]. Intriguingly, a previous study on mGluR7 also indicated that interaction with the PDZ domain containing protein PICK1 induces mGluR7 anchoring and clustering[148]. mGluR7 interaction with PICK1 is crucial for successful inhibition of the transmitter release and for the specific inhibition of $Ca_v2.1$ in cultured cerebellar granule

neurons[149]. Moreover, the A-kinase anchoring protein 79/150 (AKAP 79/150) was found to form a signaling complex with β2-adrenergic receptor, PKA, and PKC in cells and tissue extracts to promote the receptor phosphorylation and MAPK activation after agonist stimulation[150].

a G protein-dependent mechanisms

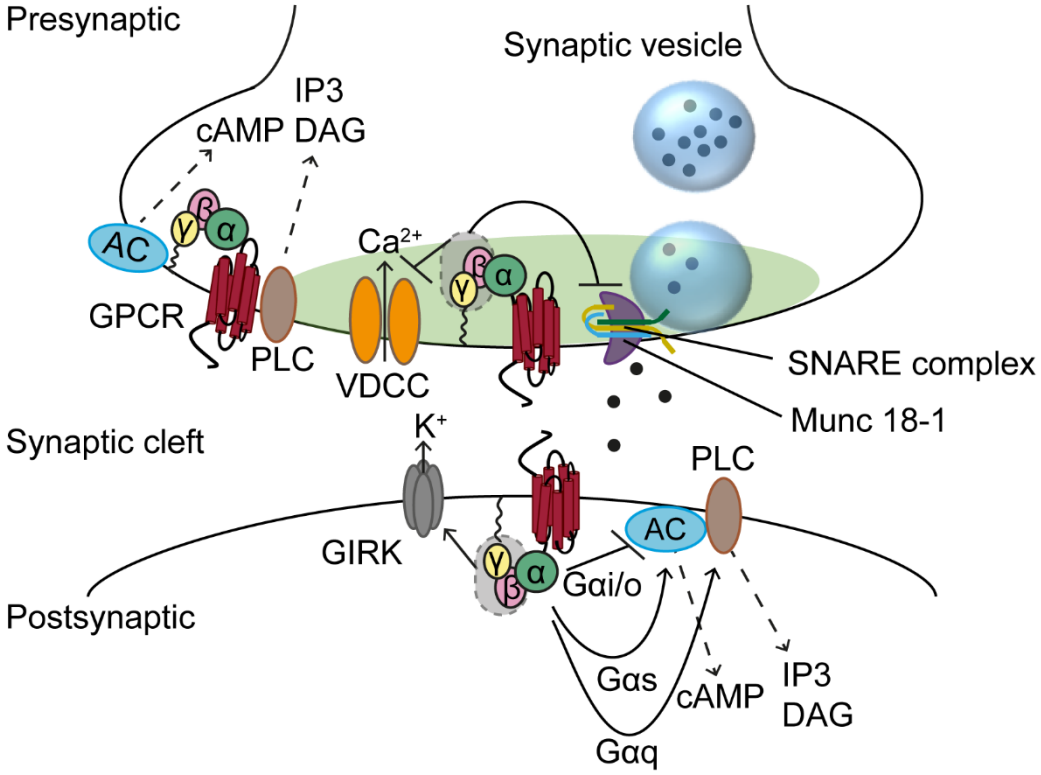

b G protein-independent mechanisms

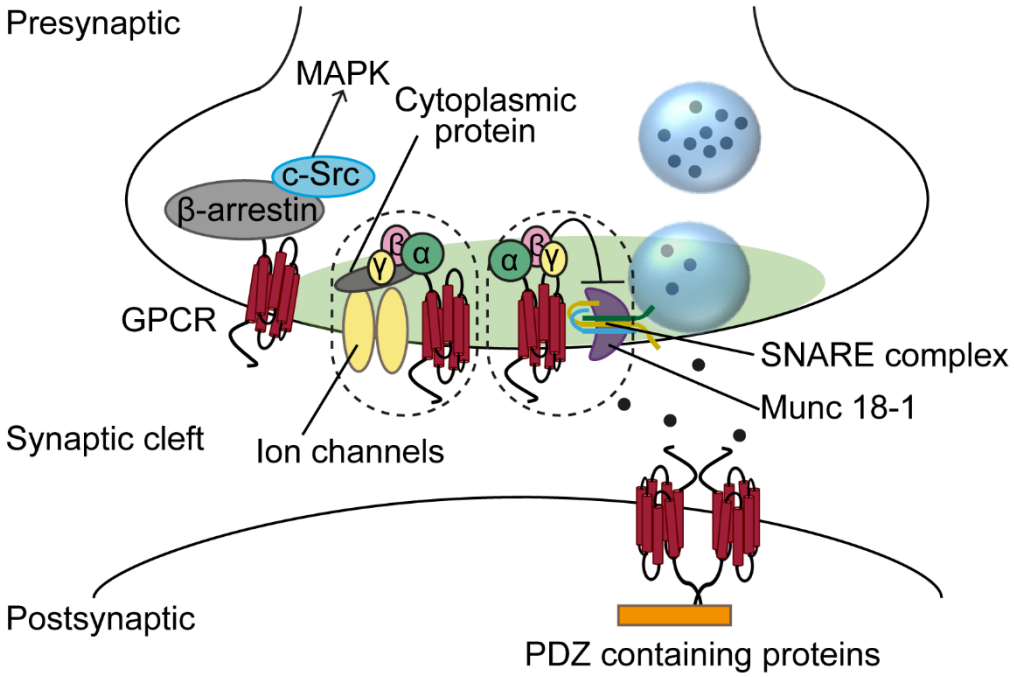

Figure 4: Overview of the mechanisms behind GPCR regulation of synaptic transmission. The scheme describes two general mechanisms behind GPCR-mediated regulation of synaptic transmission. **(a)** G protein-dependent mechanisms: a Gβγ dimer generated from active GPCR interacts with VDCC to inhibit Ca^{2+} influx, thus reducing sensitivity to depolarization. Gβγ dimer also binds with GIRK channels and increases K^+ efflux to mediate hyperpolarization. Additionally, Gβγ interacts with the SNARE complex to inhibit neurotransmitter release from SVs. Activated Gαs and Gαi/o activate and inhibit AC to increase or decrease cAMP production, respectively. Gαq activates PLC pathway to reduce PIP2 and induce DAG and IP3 transduction pathway. **(b)** G protein-independent mechanisms: The function of GPCRs is regulated by the formation of macromolecular complex with effectors (e.x: ion channels and exocytotic machinery elements). G protein-independent mechanisms are mediated as well by β-arrestin activation to initiate c-Src non-receptor tyrosine kinase signaling. PDZ domain containing scaffolding proteins interact with the C-terminal of GPCRs to determine the organization of the receptors at the cell surface.

1.7 Trafficking and lateral mobility of GPCRs at synapses

Long-term potentiation (LTP) and long-term depression (LTD) are thought to be the underlying mechanisms behind information learning and memory[151]. α-amino-3-hydroxy-5-methyl-4-isoxazole-propionic acid (AMPA) and N-methyl-D-aspartate (NMDA) glutamate receptors are the main triggers/modulators of synaptic responses during LTP and LTD[152]. $GABA_BR$ tightly regulates NMDAR mediated LTP and LTD[153]. mGluRs can induce NMDAR-independent LTD and modulate stimulation of LTP[154, 155]. Synaptic plasticity (changes in synaptic strength) is regulated by forward receptor trafficking from intracellular receptor site of synthesis to the cell surface and then to the site of degradation (exocytosis/endocytosis). The second mechanism that is receiving attention recently is the regulation of synaptic strength by the receptor lateral diffusion into and out of synaptic compartments[152, 156]. This second mechanism was reported extensively for NMDA and AMPA where receptors move rapidly between synaptic and extrasynaptic compartments to alter the number and composition of receptors available for the released neurotransmitters[157, 158, 159]. The neurotransmitter receptor functions variably depending on receptor location at synaptic or extrasynaptic compartments. For instance, NMDA receptors located at synaptic compartments regulate cell survival pathways; whereas receptors located at extrasynaptic compartments activate apoptotic pathways[160, 161]. Several scaffolding proteins were reported to anchor ionotropic receptors at excitatory and inhibitory postsynaptic specializations opposite to the neurotransmitter release sites. These proteins connect the receptors to the cytoskeleton and are also involved in the regulation of synaptic transmission[162]. The inhibitory receptors glycine and $GABA_A$ are organized in the form of

clusters and connect to the cytoskeleton elements via interaction with gephyrin[163, 164, 165]. Acetylcholine receptors (AChR) are stabilized to the NMJ via the anchoring protein rapsyn[166, 167]. NMDA receptor is anchored to excitatory synapses via PSD-95 with the cooperation of other anchoring proteins[168, 169].

However, there are only few studies reporting the detailed localization and dynamic characteristics of GPCRs among different compartments within the neurons at a level of individual protein, molecular mechanisms regulating their surface expression, and the consequences on synaptic plasticity. mGluR5 which belongs to group I mGluRs was found to diffuse faster after agonist stimulation. The receptor confinement within dynamic clusters was regulated by the scaffold protein homer1b. This study was conducted using single-particle tracking and fluorescence recovery in neurons[170, 171]. Additionally, it was reported that homer 1 regulates group I mGluRs (mGluR51/mGluR5) trafficking and surface expression via local retention of these receptors at dendritic endoplasmic reticulum (ER)[172]. Results from experiments done on group I mGluRs suggest that the receptor mobility and organization might influence synaptic strength. In a previous study using high-resolution single nanoparticle imaging, D1 dopamine receptors were found to diffuse rapidly at glutamatergic synapses in cultured hippocampal neurons. Stabilization of diffusing D1 receptors was surprisingly not regulated by the scaffold protein PSD95 but rather mediated by direct interaction with NMDAR in the postsynaptic density area providing an evidence for the glutamate-dopamine cross-talk[173]. Somatostatin receptors type 2A (SSTR2A) were found to be dynamic and mobile in hippocampal neurons using fluorescence recovery after photobleaching (FRAP) study. Agonist stimulation induced SSTR2A receptor internalization, afterwards receptor cargos were found to recycle via the trans-Golgi network (TGN)[174].

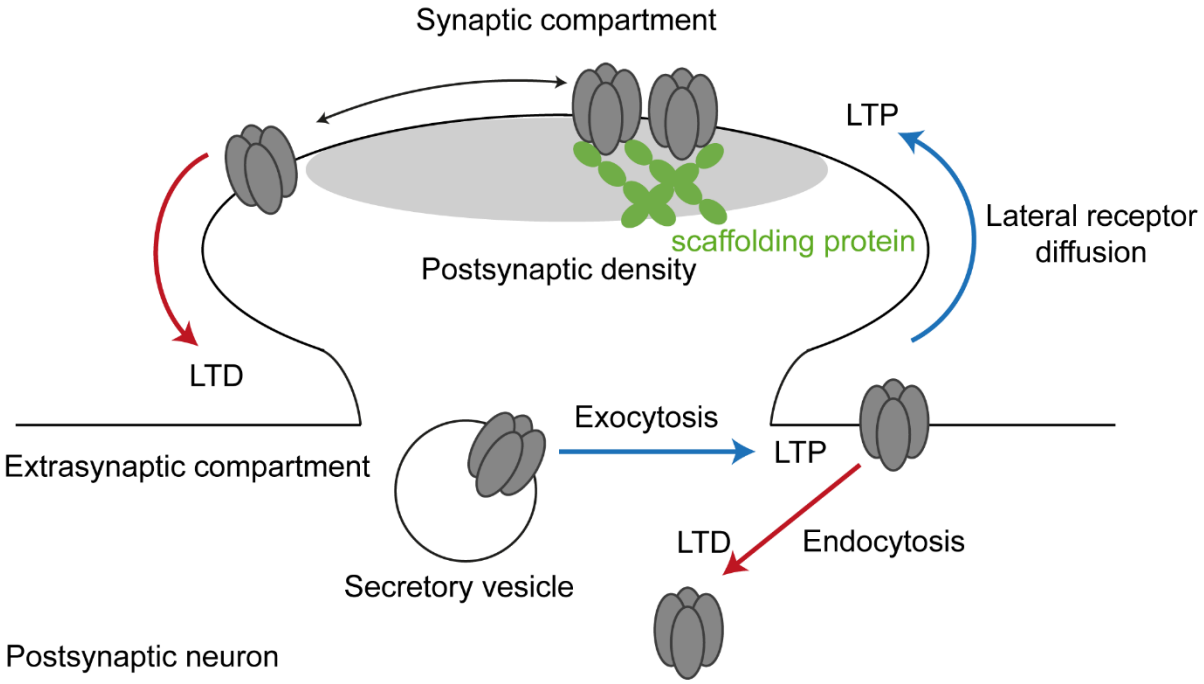

Figure 5: Schematic diagram depicting receptor trafficking and lateral diffusion events at synapses during synaptic plasticity. Receptors are anchored to the postsynaptic density through interactions with synaptic scaffolding proteins. Insertion of the receptors to the plasma membrane and internalization mediate LTP (blue arrow) and LTD (red arrow), respectively. Receptors are recruited from extrasynaptic compartment to the synaptic compartment via lateral receptor diffusion to mediate LTP (blue arrow). Similarly receptor exchange from synaptic compartment to extrasynaptic compartment to mediate LTD (red arrow).

1.8 Distribution of class C GPCRs in the CNS

There are more than 1000 GPCRs expressed in neurons activating versatile regulatory effects on synaptic transmission. Thus, selective subcellular localization must be one of the factors involved in determining the specific pharmacological profile of GPCRs. Only a handful of experiments reported the fine localization of class C GPCRs due to the lack of specific antibodies. While ionotropic receptors are located postsynaptically to mediate fast synaptic transmission, mGluRs and $GABA_BRs$ show selective localization resulting in versatile roles for the regulation of synaptic transmission[29]. mGluRs and $GABA_BRs$ are expressed in both glutamatergic and GABAergic synapses where they function as auto- and heteroreceptors[175, 176, 177].

Members of group I mGluRs (mGluR1/mGluR5) have similar distribution throughout the CNS. Intense mGluR1 expression has been detected in the cerebellar cortex, olfactory bulb, substantia nigra, thalamus, and in the hippocampus. Similarly, mGluR5 is expressed in the

cerebellar cortex, olfactory bulb, thalamus, hippocampus, and in the spinal cord[178, 179]. Group I receptors are expressed in neurons mainly postsynaptically in perisynaptic regions (regions surrounding the AZ, where synaptic vesicles endocytosis takes place) to regulate activation of the neuronal excitability[180, 181]. Additionally, mGluR5 expression was detected in handful of experiments presynaptically and in glial cells [179, 182, 183].

Group II receptors (mGluR2/mGluR3) are located in the cortex, olfactory bulb, cerebellar cortex, nucleus accumbens, striatum, amygdala, and in the hippocampus[184, 185]. They are expressed in neurons both on pre- and postsynaptic elements. On dendritic spines, they are expressed in perisynaptic sites similar to group I receptors[125, 184]. On presynaptic neurons, they are segregated from group III receptors. This is because group II receptors are concentrated on pre-terminal portions of the axons while group III receptors are concentrated in the AZs[186]. Moreover, mGluR3 is expressed abundantly in glial cells in contrast to mGluR2[182, 183].

mGluR4 and mGluR7 are widely distributed throughout the CNS. They are expressed in the cerebellum, olfactory bulb, thalamus, amygdala, and in the hippocampus. mGluR8 shows more limited distribution in olfactory bulb, thalamus, cerebellum, and in the hippocampus[29, 187, 188, 189]. An exception from group III receptors is mGluR6, which is located exclusively in the bipolar retinal cells postsynaptically[190, 191]. Group III receptors (mGluR4/mGluR7/mGluR8) are almost exclusively concentrated in the presynaptic AZs to mediate depression of synaptic transmission[186, 192]. However, some studies have reported postsynaptic location of mGluR7 in the cerebellar cortex of rodents and human[193].

$GABA_BRs$ are distributed in all neuronal types and glial cells. $GABA_BR$ is expressed abundantly in the hippocampus, cerebellum, interpeduncular nucleus, cerebral cortex, and in the spinal cord[177, 194, 195]. The receptor is expressed at excitatory and inhibitory terminals to function as hetero- and autoreceptors, respectively, to mediate inhibitory responses. On the subcellular level, presynaptic $GABA_BR$ subunits are expressed in the synaptic compartments and more abundantly at the extrasynaptic sites of glutamatergic and GABAergic axon terminals. Dominant expression is found on postsynaptic specializations with more abundant localization at the extrasynaptic membrane of the spines and dendritic shafts of neurons and interneurons as detected in the hippocampus of rats[177]. $GABA_BRs$ are expressed in astrocytes and in microglial cells[196].

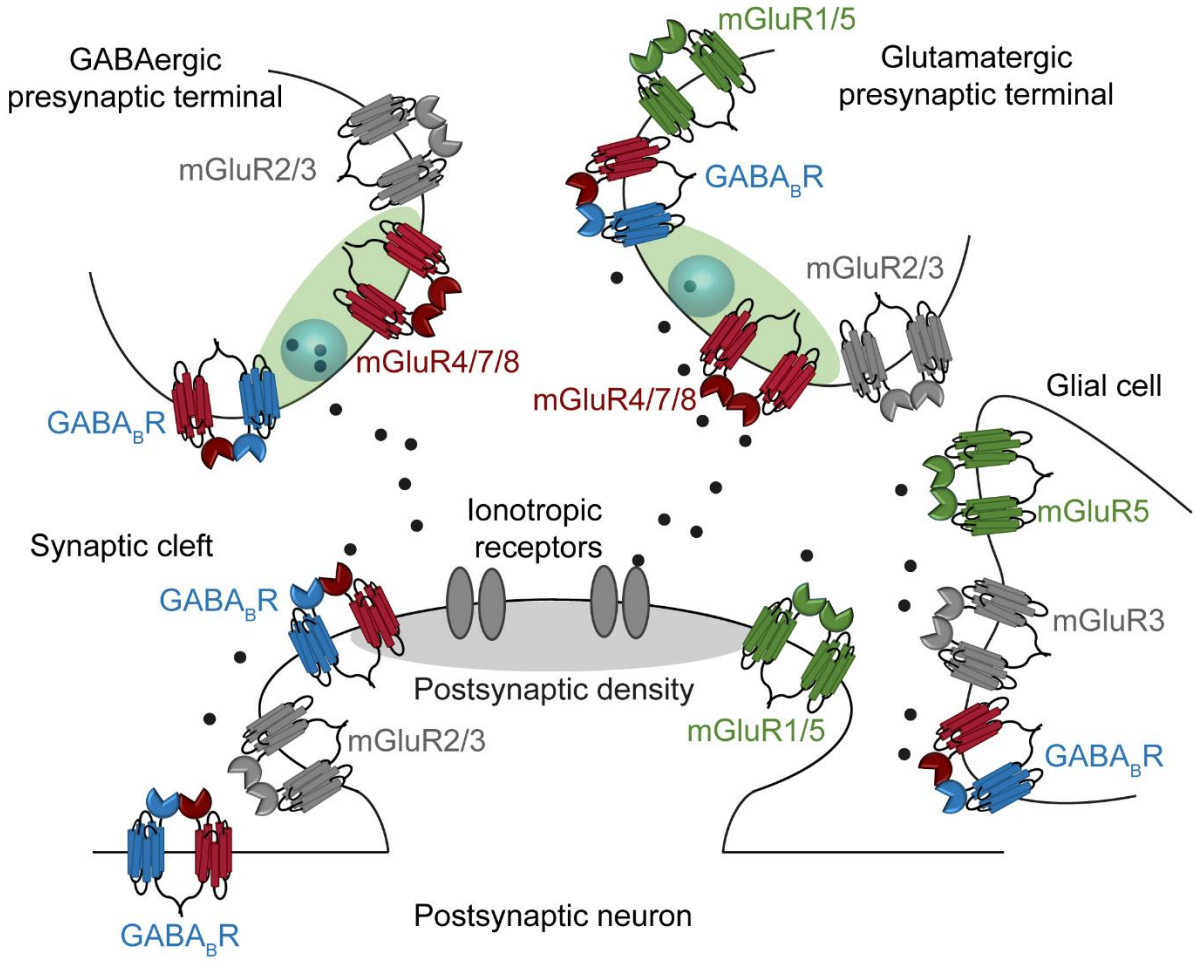

Figure 6: Schematic drawing describing the location of mGluRs and GABA$_B$R at the synapse. Group I mGluRs (mGluR1/mGluR5) (green) are located mainly on postsynaptic elements in regions surrounding the postsynaptic density, with minor expression presynaptically. Group II mGluRs (mGluR2/mGluR3) (gray) are more occasionally located at pre-terminal sites of presynaptic neurons and less abundantly on postsynaptic elements. Group III mGluRs (mGluR4/mGluR7/mGluR8) (red) are almost exclusively concentrated at the presynaptic terminal AZs. GABA$_B$R (blue and red) is expressed mostly in extrasynaptic compartments of the dendritic spines and shafts and it is also located presynaptically with more dominant location at extrasynaptic compartments. Glial cells express mGluR3, mGluR5 and GABA$_B$R.

1.9 The therapeutic potentials of class C GPCRs

The existing pharmaceuticals prescribed for the treatment of neurological and psychiatric disorders have multiple adverse effects. In addition, they have low efficacy and patients do not adhere to treatment regimens with them. Hence, there is an urgent need for the development of new therapeutics to control these diseases. mGluRs and $GABA_BR$ represent promising therapeutic targets for the treatment neurological and neuropsychiatric disorders as they are ubiquitously expressed in the CNS to fine-tune synaptic transmission. In addition, differential mGluRs distribution provides a chance for development of drugs that act on a specific location to treat certain diseases. So far, Baclofen- (a $GABA_BR$ allosteric agonist) and Cinacalcet- (a positive allosteric modulator (PAM) for CaSR) are the only two FDA-approved drugs targeting class C GPCRs. Baclofen is a potent analgesic and muscle relaxant prescribed for the treatment of spasticity from multiple sclerosis but it has many side effects such as headache, dizziness, weakness, and cognitive impairments.

To date, there is no single therapeutic agent targeting mGluRs available on the market. However many preclinical and clinical trials have shown that treatment using ligands for mGluRs might be useful for the treatment of anxiety, migraine, Parkinson's disease, schizophrenia, and epilepsy. Generally, inhibition of the over-activated glutamate neurotransmission by inhibiting group I mGluRs (by antagonists or negative allosteric modulators (NAMs)) or by activating group II/III mGluRs (by orthosteric ligand or PAMs) seems like a rational approach. Many PAMs and NAMs for mGluRs have been synthesized to optimize the treatment by enhancing subtype specificity and avoiding the activation of classical orthosteric binding site of glutamate. Allosteric modulators have the additional advantages that they have a saturation (ceiling) effect and most of them do not function unless an orthosteric agonist is bound to the receptor leading to restricted signaling[197]. A number of amino acids analogs have developed for mGluRs for example LY354740, a mGluR2/3 agonist that was shown to reduce the severity of anxiety panic symptoms in human[198]. A preclinical study showed that, mGluR4 orthosteric ligand LSP4-2022 produced antiparkinsonism effects upon systemic administration in haloperidol-induced catalepsy test in rats[199].

Multiple reports showed that targeting $GABA_BR$ is a promising approach to treat drug withdrawal symptoms, chronic pain, anxiety, depression, and epilepsy. It is widely accepted that GABA is the main inhibitory neurotransmitter in the central nervous system. Subsequently, agents that activate $GABA_BR$ (orthosteric ligand or PAMs) could function as anxiolytics, suppressers of cocaine or nicotine addiction, and anti-nociceptive. In contrast, agents that cause inhibition of $GABA_BR$ (antagonist or NAMs) could function as antidepressants. For

instance, subcutaneous or intrathecal administration of CGP35024 (a novel $GABA_BR$ agonist) reversed mechanical hyperalgesia in rat chronic neuropathic model[200]. Preliminary clinical study showed that Baclofen administration reduces alcohol-intake[201]. On the other hand, only one $GABA_BR$ antagonist was tested in clinical trials due to low efficacy of the developed compounds but researchers are working on optimizing pharmacokinetic profile of this antagonist[202]. However, preclinical trials are showing promising results. As an example, $GABA_BR$ antagonist blocked absence seizers in a dose dependent fashion in rats[203].

1.10 Superresolution microscopy

Within the past two decades a range of techniques have been developed to overcome the diffraction limit of light. This limit introduced by Ernst Abbe and Lord Rayleigh in the nineteenth century stats that when the lateral distance between two molecules in a structure is less than half of a wavelength (λ) of light used for imaging, then they cannot be resolved[204, 205]. This distance for optical microscopy is about 200 nm (wavelength of far blue light is 400 nm). The enhanced spatial resolution of emerging superresolution microcopy (SRM) techniques to more than one magnitude is getting close to the electron microscopy (EM) resolution.

SRM is generally divided into two classes. The first class is referred to as the superresolved ensemble fluorophore microscopy including stimulated emission depletion microscopy (STED); a technique developed by Stephan Hell. In this technique, the fluorophores are selectively deactivated to minimize the illumination from outer part of the focal spot to generate a subdiffraction-sized emitting molecule[206, 207]. Another technique is structured illumination microscopy (SIM), which is based on the interference between two beams to generate a sinusoidal excitation pattern superimposed on a sample to reject out-of-focus blur[208, 209]. The second class of SRM techniques is single-molecule localization microscopy (SMLM). These techniques are usually easier to conduct than the previously mentioned techniques and more widely applied in biology field to address quantitative and qualitative questions. Superresolution is achieved by turning on only a sparse subset of the fluorescent molecules into the *on*-state by light. The single-molecule centroids are then determined with a few nanometers precision. The *on-, off*-states of fluorophores could be attained by genetically expressed photoactivatable or photoconvertable fluorescent proteins for photoactivation localization microscopy (PALM)[210] and fluorescent PALM (fPALM)[211]. In stochastic optical reconstruction microscopy (STORM)[212] and *direct* stochastic optical reconstruction microscopy (*d*STORM)[213], a combination of reporter and activator cyanine dyes, and conventional fluorescent probes such as the Alexa Fluor dyes are used, respectively. Many additional methods have emerged as well[214].

*d*STORM, a technique developed by Prof. Sauer's group in Würzburg is very powerful in revealing the nanoscopic cellular details of the cell, quantitative data, and the cluster size of targets[215, 216]. *d*STORM has been applied for the quantitative analysis of endogenous CAZ protein (Bruchpilot) at the Drosophila NMJ to understand how the CAZ ultrastructure is linked to the synaptic function[217]. *d*STORM was also used to compare the spatial distribution of different mitochondrial proteins[218]. This technique was successfully used to study the size, density, and distribution of plasma membrane glycans with click chemistry, where the study revealed homogenous glycan distribution on the plasma membrane.

Basically, *d*STORM takes advantage of the temporal separation of the fluorescence emission of synthetic organic fluorophores by inducing reversible switches between the *on*- and *off*-states. Photoswitching is induced by the presence of millimolar concentrations of a thiol reducing agent such as β-mercaptoethylamine[219, 220]. The reduction of first excited singlet state of the dye is not likely by thiols. However, the triplet state is energetically stabilized and can be reduced by thiols in an aqueous medium to form the corresponding radical anion and thiyl radical (refer to the Jablonski diagram in **Fig. 7a**). Upon irradiation with light, thiol presence favors the transfer of majority of the fluorophores to the reversible *off*-state, whereas only a small subset resides in an on state at a given time. The molecules enter the fluorescent cycle in a stochastic manner either spontaneously or via irradiation with a second laser. Subsequently, one fluorophore will be stochastically activated per diffraction-limited area. Finally, the fluorophores are localized by a two-dimensional Gaussian fitting of the PSF with a high localization precision. This process is repeated over thousands of frames until each fluorophore has been localized at least once to reconstruct the superresolved image[221]. The localization precision is dependent on the number of detected photons and signal-to-noise ratio.

Applying *d*STORM to detect targets via primary and secondary antibodies labeled with fluorophores has an advantage of analyzing proteins at endogenous expression levels. In other words, artificial overexpression of fusion proteins required for PALM can be avoided. Moreover, genetically fused tags might lead to misfolding and abnormal expression or location. Additionally, organic dyes used for *d*STORM are typically brighter and more photostable than the fluorescent proteins. On the other hand, *d*STORM technique suffers from some limitations such as the epitope accessibility by the antibody and/or antigen avidity during immunofluorescence (IF).

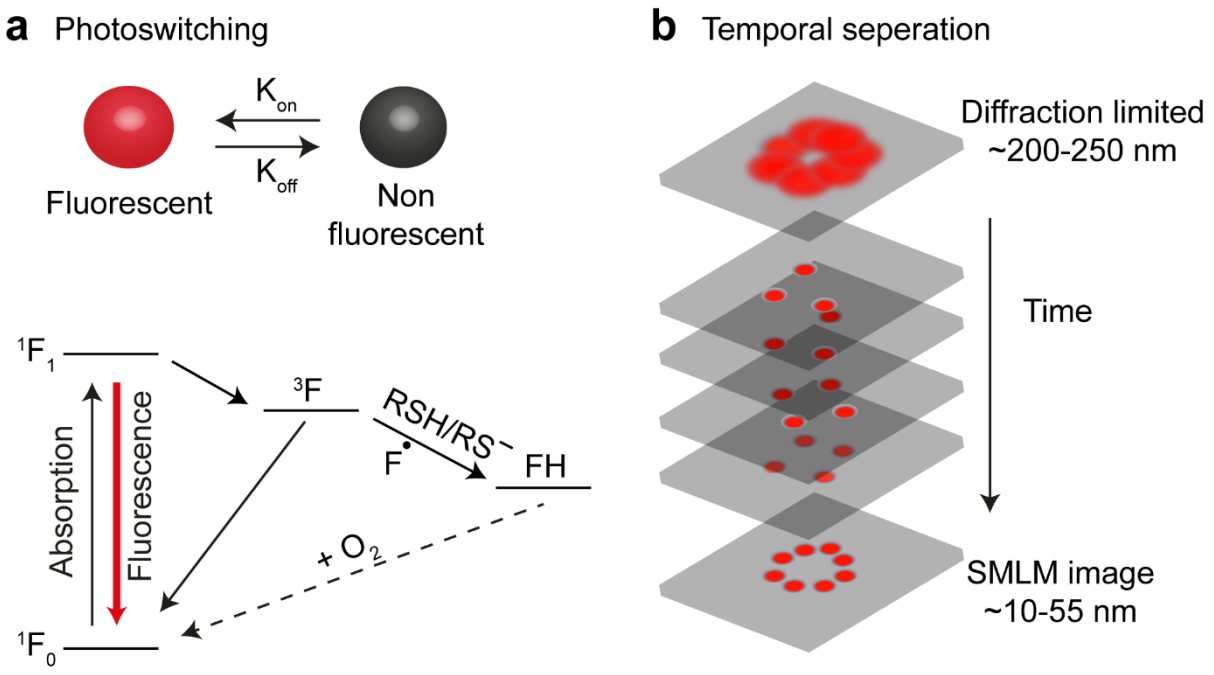

Figure 7: Schematic illustration of the *d*STORM concept. Superresolution in *d*STORM is achieved by combining **(a)** photoswitching of organic fluorophores between a fluorescent (*on*-state) and non-fluorescent (*off*-state) states in the presence of thiol with **(b)** stochastic activation and single-molecule localization. As a result, a superresolved image is reconstructed.

1.11 Single-molecule total internal reflection microscopy (TIRFM)

Understanding the behavior of GPCRs on the level of individual molecules helps us in understanding the complex macromolecular systems and the mechanisms of receptor responses to extracellular signals. There has been a surge in number of publications applying single-molecule microscopy to study the dynamic processes of GPCRs in real time in living cells[222]. Single-molecule microscopy was used to study the diffusion, oligomerization, conformational diversity, trafficking, signaling of GPCR microdomains, and G protein activation[47, 223, 224, 225, 226]. A single-molecule TIRFM based approach was established in Prof. Calebiro's group, to study the diffusion and stoichiometry/oligomerization of GPCRs on the surfaces of living cells[47, 227]. First, transmembrane receptors are labeled with bright organic fluorophores via the SNAP/CLIP-tags technology. SNAP/CLIP-tagged membrane receptors are visualized with the total internal reflection microscopy (TIRFM). These tagged receptors are labeled with fluorescent substrates and then detected and tracked to measure the coordinates and the amplitudes (intensities) of all particles. The generated single-molecule

data is analyzed to estimate the number of molecules per oligomeric assembly. Moreover, the data can be used to analyze the motion of the receptors.

GPCRs are fluorescently labeled via variable approaches to visualize individual receptors. A powerful approach for labeling GPCR[227] is based on the SNAP/CLIP-tags technology[228]. In this technique, a SNAP-tag (20kD) which is a mutant of the human DNA repair enzyme O^6-alkylguanine-DNA alkyltransferase (hAGT) is directly fused to the molecule of interest. Then, the SNAP-tag is labeled easily and specifically by small bright fluorophores via an irreversible covalent bond. For experiments where multilabeling is necessary, CLIP-tag could be introduced to the second target. A second approach to label GPCRs involves the use of ligand (agonist/antagonist) conjugated to small organic fluorophores[226, 229]. A third approach is to fuse fluorescent proteins to the targets. However, difficulties are faced with this approach due to low signal-to-noise ratio as a result of low fluorescence quantum yield of the fluorescent proteins. Additionally, high background results from the fluorescent proteins trapped in the intracellular pool[230, 231].

For a typical epifluorescence setup, a high background is generated due to the out-of-focus light. This out-of-focus fluorescence could be eliminated to enhance the signal-to-noise ratio by the application of the total internal reflection fluorescence (TIRF) configuration[232]. To achieve TIRF, an objective with a high numerical aperture (> 1.45) and two materials with different refractive index values are used. When the light beam comes with an angle θ higher than the critical angle θ(c), it will be totally reflected at the interface between the coverslip (higher refractive index) and the medium (lower refractive index). As a result, a thin electromagnetic evanescence wave of approximately 100 nm (compared to 100 µm in epifluorescence) is generated. The evanescence wave exhibits an exponential decay depending on the distance from the coverslip. The selective excitation of the fluorophores near to the coverslip results into single-molecule detection and less photobleaching. However, a major disadvantage is that the cell interior is not accessible.

The photon emission of the single-fluorescent molecules is collected with an electron-multiplying charge coupled device (EMCCD) camera. Single receptor/single complex particles are automatically detected and tracked using a noncommercial *u-track* software implemented in MATLAB environment. The location and intensity of the diffraction-limited particles are determined by the analysis. Briefly, this is done by fitting the intensity profile of the single particle (the point spread function (PSF)) with a two-dimensional Gaussian function in all frames of the movie. Hence, a high spatial resolution (10 – 55 nm) which is far below the diffraction limit of light is achieved. While the centroid of the Gaussian fit determines the lateral position, the standard deviation yields the axial position and the spatial resolution of the

imaging setup. Finally, the number of receptors per complex are calculated. This is done by estimating the intensity of single fluorophores. The intensity of single fluorophores at the end of each movie is fitted with the mixed Gaussian model as a reference for a monomer intensity distribution. Then the particle/complex intensities are measured by averaging the intensities from the beginning of the movie to the frame before the start of photobleaching (up to 20 frames). The distribution of the intensity of all particles is fitted with the mixed Gaussian model according to the equation below. The relative abundance of each underlying population (monomers, dimers, higher order oligomers) is calculated by measuring the area under the curve of each population.

$$\varphi\,(i) = \sum_{n=1}^{n_{max}} A_n \,\frac{1}{n\sigma\sqrt{2\pi}} e^{-\frac{(i-n\mu)^2}{2(n\sigma)^2}}$$

Where φ (i) is the frequency of particles with intensity i, n is the component number, A_n is the area under the curve of each underlying component, and μ and σ are the mean and standard deviation of the intensity of the employed fluorophore, respectively.

The dynamics of the receptors can be studied as well. This is done by calculating the mean square displacements (MSD) and diffusion coefficients of the trajectories derived from the TIRF images according to the following equations:

$$MSD(\Delta t) = \frac{1}{N}\sum_{i=1}^{N}[(x_{i+\Delta t} - x_i)^2 + (y_{i+\Delta t} - y_i)^2]$$

Where Δt is the time interval between frames, N is the number of steps analyzed, and x and y are the x- and y-coordinates of the particles. The diffusion coefficient (D) is computed by fitting the MSD with the following equation:

$$MSD\,(t) = 4Dt^{\alpha} + 4{\sigma_1}^2$$

Where t corresponds to time, α is the anomalous diffusion exponent, and σ_1 is the standard deviation of the Gaussian localization error (which was estimated to be ~ 23 nm). From evaluation of the MSD plot over time, the type of the trajectory motion is classified into four categories. A linear MSD increase with time suggests free Brownian motion (normal diffusion). A positive curvature indicates directed motion (super-diffusion). A negative curvature suggests confined motion (sub-diffusion). The receptors are assumed immobile when no MSD increase is observed with time.

The previously described single-molecule TIRFM approach was applied to reveal the oligomeric state, stability, and mobility of three prototypical GPCRs under physiological conditions[47]. β1- and β2-adrenergic receptors were found to diffuse freely on the plasma membrane and exist in equilibrium between a monomeric and a dimeric state. The size of the

complex increased gradually when the receptors were expressed at higher densities because they interact primarily through transient receptor-receptor interactions. $GABA_BRs$ were less motile than the β-adrenergic receptors and they formed large complexes composed of dimers or tetramers of $GABA_BR$ heterodimers. $GABA_BR$ oligomers were organized in form of arrows on the cell surface, via the receptors interaction with the actin cytoskeleton[47].

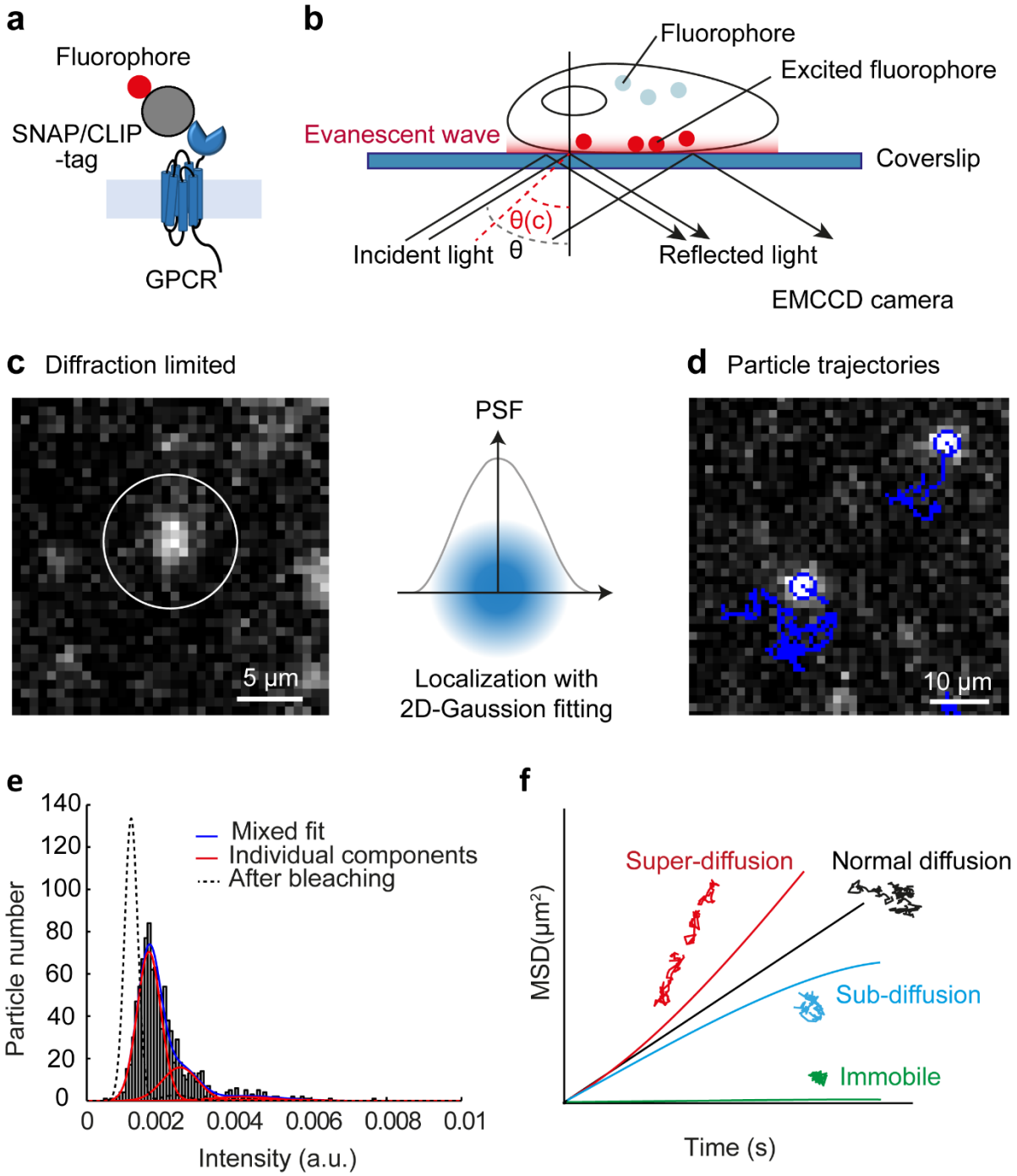

Figure 8: Visualization of GPCRs by single-molecule TIRFM in living cells and subsequent analyses. (a) Schematic drawing of a GPCR carrying an N-terminal SNAP/CLIP-tag. SNAP/CLIP-tagging system allows labeling of the receptor with a bright fluorophore. **(b)** Schematic illustration of the TIRF configuration concept. The excitation light is directed to the specimen at an angle θ greater than the critical angel θ(c) and then is totally internally reflected at the coverslip-medium interface. Fluorophores near to the interface within the generated evanescent field are excited, while those located far from the interface are not excited. **(c)** A TIRF image acquired from a cell transfected with a SNAP/CLIP-GPCR then labeled with an Alexa Fluor dye. The dot is a single receptor/complex fluorescent spot. The coordinates of the particles are determined by fitting the PSF of the diffraction-limited spot with a two-dimensional Gaussian function. **(d)** GPCR tracking. The trajectories of single diffusing receptors are derived from the TIRF image. The blue circles and trajectories indicate particle positions and motion, respectively. **(e)** Analysis of the number of receptors per complex by analyzing the distribution of intensity of all particles. The underlying populations are revealed by fitting the distribution of the intensity of particles with a mixed Gaussian model. The intensity of single fluorophores at the end of each movie is fitted with the mixed Gaussian model (dotted black line) as a reference for the intensity distribution of a monomer. **(f)** MSD plot over time. The type of the trajectory motion is classified into four categories according to the MSD plots. The four categories are super-diffusion, normal diffusion, sub-diffusion and immobile.

2 Aims of this study

The aim of my thesis was to investigate the distribution and spatiotemporal dynamics of two prototypical class C GPCRs (mGluR4 and $GABA_BR$) in neurons. I used advanced imaging techniques with high spatial (10-20 nm) and temporal (20 ms) resolution.

First, I analyzed the nanoscopic organization of mGluR4 at the presynaptic active zones (AZs) to achieve the following aims:

1- To reveal the nanoscopic distribution of mGluR4 at the model synapse between parallel fibers and Purkinje cells in the cerebellum of mouse using *d*STROM
2- To analyze the oligomeric state of mGluR4 in CHO cells using single-molecule TIRFM
3- To estimate the number and stoichiometry of mGluR4 complexes witihin the AZs
4- To correlate the localization of mGluR4 with both structural (bassoon) and functional components of the AZs ($Ca_V2.1$ channels and Mun 18-1) using a distance-based colocalization analysis

Secondly, I analyzed the dynamic patterns of $GABA_BR$ in living primary hippocampal neurons to achieve the following aims:

1- To analyze the lateral diffusion patterns of $GABA_BRs$ in the synaptic and extrasynaptic compartments in cultuerd hippocampal neurons using single-molecule TIRFM and the mean square displacment (MSD) analysis
2- To investigate the role of the actin cytoskeleton in the regulation of the spatial distribution of $GABA_BRs$

3 Materials and methods

3.1 Materials

3.1.1 Animals

Wild-type adult FVB mice were used for the preparation of hippocampal neuronal cultures and mouse cerebellar slices. The mice were housed in the animal facility of the Institute of Pharmacology and Toxicology, University of Würzburg. The mice were housed under controlled temperature and light/dark cycles with unlimited access to food and water.
All animal work was conducted according to regulations of the relevant authority, the government of Lower Franconia, Bavaria.

3.1.2 Reagents and antibodies

Reagents	Manufacture, catalogue number
Agar	Applichem, A0949
ADVASEP-7	Sigma-Aldrich, A3723-250MG
Alexa Fluor 532 Phalloidin	Thermo Fischer Scientific, A22282
β-mercaptoethylamine	Sigma-Aldrich
Bovine serum albumin	Applichem, A1391
B 27 (50 ×)	Thermo Fischer Scientific, 17504-044
CLIP-Surface® Alexa Fluor 647	New England BioLabs, S9234S
Chloroform	Sigma-Aldrich, 288306
Dimethyl sulfoxide (DMSO)	AppliChem, A1391
Ethanol	Sigma-Aldrich, 32205-2.5L-M
Ethidium bromide	Applichem, A1152.0025
Ethylenediaminetetraacetic acid (EDTA)	Applichem, A5097
Fetal bovine serum	Biochrom, S0115
FM®4-64 Dye (N-(3-Triethylammoniumpropyl)-4-(6-(4-(Diethylamino) Phenyl) Hexatrienyl) Pyridinium Dibromide)	Thermo Fischer Scientific, T3166
GlutaMAX	Thermo Fischer Scientific, 35050061
Glycine	Applichem, P110906
HEPES	Thermo Fischer Scientific,15630-056

Lipofectamine 2000	Thermo Fischer Scientific,11668-019
L-Glutamine	PAALab., M11-004
Methanol	Sigma-Aldrich, 322130,2.5L-M
Normal goat serum	Sigma-Aldrich, G9023
Paraformaldehyde (PFA)	Sigma-Aldrich, P6148
Potassium chloride (KCl)	Applichem, A3582
Phenol red-free Dulbecco's Modified Eagle Medium (DMEM)/ F-12	Thermo Fischer Scientific, 11039
Phenol red-free Neurobasal Medium	Thermo Fischer Scientific, 12348017
Phenol red-free Neurobasal-A Medium	Thermo Fischer Scientific, 12349015
Phenol red-free 10 × HBSS	Thermo Fischer Scientific, 14065056
phosphate-buffered saline	Thermo Fischer Scientific, D8537
SNAP-Surface® Alexa Fluor 647	New England BioLabs, S9136S
SNAP-Surface® Alexa Fluor 549	New England BioLabs, S9112S
Sodium chloride (NaCl)	AppliChem, A1149
Sodium dodecyl sulfate (SDS)	Applichem, A1502
Sodium hydroxide pellets	Sigma-Aldrich, S8045
Sodium phosphate dibasic	Sigma-Aldrich, 71662
Sodium phosphate monobasic	Sigma-Aldrich, 71507
TetraSpeck microspheres (0.1 µm)	Thermo Fischer Scientific, T7279
Tissue-Tek O.C.T.	Sakura Finetek, 12351753
Tris	AppliChem, A2264
Triton X-100	Applichem, A4975
Trypsin 0.05%/EDTA 0.02%	Pan Biotech, P10-023100
1 kb DNA ladder	New England Biolabs, N3232L
10,000 IU/ml penicillin 10 mg/ml streptomycin cocktail	Thermo Fischer Scientific, 15140122
10x Pfu reaction buffer	Promega, M776A
18-mm glass coverslips	Vetrini copriogetto, 41001118
3-aminopropyltriethoxysilane	Sigma-Aldrich, 440140

Table 1: Materials and reagents used in this study.

Primary antibodies	Immunogen	Supplier, catalogue number	Dilution
Guinea pig polyclonal anti-mGluR4a	Synthetic peptide corresponding to the C-terminus of rat mGluR4 (amino acid residue 890 - 912)	Prof. Ryuichi Shigomoto	1:100/ 1:200
Mouse monoclonal anti-bassoon	N.A.	Enzo, SAP7F407	1:400
Rabbit polyclonal anti-bassoon	N.A.	Synaptic systems, 141013/2	1:400
Rabbit polyclonal anti-$Ca_V2.1$	α-$_{1A}$ subunit of mouse Ca^{2+} channel *P/Q-type* (amino acid residue 856 - 888)	Synaptic Systems, 152203/6	1:200
Mouse monoclonal anti-Munc-18-1	N.A.	Synaptic systems, 116011/6	1:400
Mouse monoclonal anti-$GABA_{B1}R$	Cytoplasmic C-terminus of rat $GABA_{B1}R$ (amino acids 873 - 977)	NeuroMab, 75-183 (clone N93A/49)	1:500

Table 2: Primary antibodies used in this study. N.A.: not available.

Secondary antibodies	Type	Supplier, catalogue number	Dilution
Alexa Fluor 647-conjugated goat anti-guinea pig	Polyclonal	Thermo Fisher, A-21450	1:200
Alexa Fluor 647-conjugated goat anti-mouse	Polyclonal	Thermo Fisher, A-21237	1:200
Alexa Fluor 647-conjugated goat anti-rabbit	Polyclonal	Thermo Fisher, A-21245	1:200
Alexa Fluor 532-conjugated goat anti-mouse	Polyclonal	Thermo Fisher, A11002	1:200
Alexa Fluor 532-conjugated goat anti-rabbit	Polyclonal	Thermo Fisher, A-11009	1:200

Table 3: Secondary antibodies used in this study.

Reagents	Manufacture, catalogue number
Effectene Transfection Reagent	QIAGEN, 301425
EndoFree Plasmid Kit	QIAGEN, 12362
Neuromag starting kit	Ozbiosciences, KC 30800
Qiagen MIDI plus kit	QIAGEN,12943

Table 4: Kits used in this study.

3.2 Molecular biology methods

3.2.1 Plasmids and cloning

During this work four new plasmids were generated. The remaining plasmids were present in the laboratory or kindly provided by collaborators. An expression construct coding for mGluR4 with an HA-tag and a faster labelling variant of the SNAP-tag (SNAPf)[233] fused at its N-terminus was generated by replacing the $GABA_{B1a}R$ sequence with wild-type mouse mGluR4 cDNA and the SNAP-tag[228] with the SNAPf tag. The construct was correctly expressed on the plasma membrane and behaved like the wild-type analogue in the cAMP functional assays. The plasmids coding for an N-terminal SNAP-tagged $GABA_{B1}R$ (SNAP- $GABA_{B1}R$) and wild-type $GABA_{B2}R$ (wt- $GABA_{B2}R$) human receptors were kindly provided by Pin Jean-Philippe, Institute for Functional Genomics, Montpellier, France[65]. Three new constructs coding for $GABA_{B1a}R$ under the control of a synapsin promoter were produced. These plasmids code for $GABA_{B1a}R$ tagged at its extracellular N-terminus with an HA-tag and a SNAP-tag, or with an HA-tag and a CLIP-tag or with an HA-tag (pSYN-HA-SNAP-$GABA_{B1a}R$, pSYN-HA-CLIP-$GABA_{B1a}R$ and pSYN-HA-$GABA_{B1a}R$). Synapsin fragment was amplified from pSYN-EGFP using the polymerase chain reaction (PCR) with an extended primer pair (refer to the annex), thereby isolating the synapsin promotor and inserting the Spe I and Eag I restriction sites at the ends of the cDNA sequence. Synapsin fragment with the inserted restriction sites was used for in-frame cloning into (HA-SNAP-$GABA_{B1}R$, HA-CLIP-$GABA_{B1}R$ and HA-$GABA_{B1}R$). Plasmids expressing SNAP-CD86 and SNAP2×-CD86 were generated by replacing the YFP fused to the N-terminus of CD86 with either one or two copies of the SNAP-tag in a previously described construct[47, 234]. A construct coding for bassoon-GFP was kindly provided by Eckart D. Gundelfinger, Leibniz Institute for Neurobiology, Magdeburg, Germany. A plasmid coding for homer-GFP was a gift from Shigeo Okabe Department of Cellular Neurobiology, University of Tokyo, Tokyo, Japan.

3.2.2 Preparation of ultra-clean coverslips

Single-molecule TIRFM experiments require culturing cells on ultra-clean coverslips to minimize the background signal. Twenty-four mm glass coverslips were placed into a coverslip holder. The coverslips were treated with chloroform by placing the coverslip holder into a beaker then adding chloroform (under a fume hood). The beaker was covered with aluminum foil to prevent chloroform evaporation. Subsequently, the coverslips were sonicated in a water bath for 1 h at RT. The coverslips were allowed to dry. A second washing step was performed with 5M NaOH by repeating the previously mentioned steps. The coverslip holder holding the coverslips was placed into a new beaker then washed for three times with distilled water (30 min each). Finally, the coverslips were placed in a glass petri dish filled with absolute ethanol until the experiment day.

3.2.3 Cell culture and transfection

Chinese hamster ovary K1 (CHO-K1) cell line was obtained from American Type Culture Collection ATCC. The cell line was mycoplasma negative as confirmed by the PCR. The Cells were maintained in phenol red-free Dulbecco's Modified Eagle Medium/nutrient mixture F-12 (DMEM/F-12) supplemented with 10% fetal bovine serum and 100 IU/ml penicillin/0.1 mg/ml streptomycin cocktail at an incubator (37°C, 5% (vol/vol) CO_2 and 95% humidity). Phenol-red free media were always used to minimize the autofluorescence. The ultra-clean coverslips were washed with phosphate-buffered saline (PBS) then placed in a six-well plate. 250,000 cells were seeded on the coverslips then allowed to adhere overnight in the incubator. CHO cells (80% confluent) were transfected with 2 µg of the plasmids (SNAP-tagged membrane receptors) using 6 µl Lipofectamine 2000 according to the manufacturer’s protocol. Cells were transiently transfected for 4 - 5 h to reach physiological expression levels, which are optimum for single-molecule imaging.

3.2.4 Live-cell labeling of SNAP-tagged constructs

CHO cells expressing the SNAP-tagged membrane receptors were washed twice with pre-warmed (37°C) PBS. Live-cell labeling was performed by incubating the cells with a saturating concentration (2 µM) of the SNAP-substrates diluted in a complete phenol-red-free medium for 20 min at 37°C, 5% CO_2, and 95% humidity. Labeling of the SNAP-tag is covalent and specific. Cells were washed three times with complete culture medium (5 min each) at 37°C to washout any residues of the free fluorescence dye.

3.2.5 Cell fixation

Cells expressing SNAP-tagged constructs were labeled then washed two times (5 min each) with PBS. Cells were then fixed with 4% Paraformaldehyde (PFA) for 15 min at room temperature (RT). Subsequently, the cells were washed four times (5 min each) to remove any remaining fixative solution. The samples were kept in PBS 4°C until imaging. Coverslips holding the samples were mounted in imaging chamber then supplied with 300 µl PBS as an imaging buffer. Finally, images were acquired using single-molecule total internal reflection microscopy (TIRFM).

3.2.6 Preparation of ultra-clean coverslips for hippocampal neurons

The quality of the coverslips is remarkably important for the attachment and maturation of the neurons. The following protocol was conducted based on a procedure reported by Kaech et al.[235]. 18-mm glass coverslips were placed in a petri dish containing 1 M HCL then shaken overnight. On the next day, the coverslips were sonicated in 5 M NaOH solution for 30 min. The coverslips were rinsed extensively over a period of 3 hours by changing distilled water every 20 min. Coverslips were sonicated in distilled water for 30 min then the solution was replaced by 70% ethanol. Subsequently, the coverslips were sonicated with absolute ethanol for 1 hr. Finally, the coverslips were sterilized in an oven at 170°C for 3 hours.

3.2.7 Hippocampus dissection

Hippocampi were dissected from brains of pups obtained from pregnant mice on the 18th day of the gestational period. Pregnant mice were sacrificed by cervical dislocation, and then pups were dissected out from the uterus. Pup's heads were placed in a petri dish and maintained submerged in cold HBSS solution all the time. Pub's brains were dissected out under the stereoscope. Subsequently, meninges surrounding the cerebellar hemispheres were stripped away and the hippocampi were carefully dissected out.

3.2.8 Culturing of primary hippocampal neurons

Isolated hippocampi were maintained in ice-cold HBSS solution. The cell suspension was trypsinized for 5 min in a water bath at 37°C. Neurons were washed twice with warm HBSS solution to remove any trypsin residues, and maintained in a final volume of 1 ml of Neurobasal medium. Neurons were then triturated mechanically by passing through a 9 inch sterile glass Pasteur pipette 7 times. The neurons were then dissociated further using a Pasteur pipette with a narrowed opening by flame-polishing for additional 7 times. The cell suspension was transferred to a centrifuge tube, and then neurons were centrifuged (1000 RPM) for 1 min at 4°C. The supernatant was discarded then the cell pellet was resuspended in 1 ml Neurobasal

medium. Hippocampal neurons were cultured in Neurobasal medium supplemented with 2% B27, 2 mM GlutaMAX supplement, and penicillin/streptomycin solution in density of 40,000 cells/well over ultra-clean coverslips at 37°C, 5% CO_2, and 95% humidity. B27 supplement contains culture additives and a cocktail of antioxidants to reduce the generation of reactive oxygen species, and hence providing optimal growth and maximal survival of the neurons. On the previous day, 18-mm glass ultra-clean coverslips were placed in a 12 wells plate then coated with 1 mg/ml poly-D-Lysine overnight at 37°C. One-third of the medium was replaced with a fresh medium once a week. Monolayer cultures with less than 90% confluence ratio were selected for transfection. Neurons were transfected at 7-9 days *in vitro* (DIV) using magnetofection transfection reagent according to the manufacturer's instructions. Finally images were acquired at 10 -14 DIV using TIRFM.

Neurobasal medium		
Supplement	Volume	Final conc.
Neurobasal medium	48 ml	-
B 27 (50×)	1 ml	2%
GlutaMAX	0.5 ml	2 mM
Penicillin (10,000 IU/ml) Streptomycin (1 mg/ml)	0.5 ml	1%

Hanks Balanced Salt Solution (HBSS)		
Supplement	Volume	Final conc.
10 × HBSS, minus phenol red	50 ml	-
HEPES	3.5 ml	0.7%
Penicillin (10,000 IU/ml) Streptomycin (1 mg/ml)	5 ml	1%
H_2O (water for injection)	Add to 500 ml	

Table 5: Media preparation for neuronal hippocampal cultures.

3.2.9 Synapse staining with FM dye

Neurons were incubated with 3 µM FM4-64 Dye in HEPES buffer supplemented with 50 mM KCL for 2 min at 37°C, 5% CO^2. The high K^+ solution depolarized the neuron to initiate vesicle recycling and the dye uptake. The neurons were rinsed three times with 1 mM ADVASEP containing washing solution (2% BSA in Neurobasal medium) three times, 1 min each at 37°C. The washing solution was then replaced with a fresh one for 7 min at 37°C. Subsequently, the neurons were labelled with the Alexa Fluor dyes as described in section 3.2.3.

50 mM KCL HEPES buffer		
Supplement	Molecular weight	Weight
50 mM KCL	74.5	1.86 g
50 mM NaCl	58.4	1.46 g
2mM $CaCl_2$	110.98	110.98 mg
1 mM $MgCl_2$	95.2	47.6 mg
20 mM HEPES	238.31	2.38 g
Distilled water	Add to 500 ml, adjust to pH= 7.3 then filter	

Table 6: Solution preparation for synapse staining.

3.2.10 Immunofluorescence staining for hippocampal cultures

Hippocampal cultures (14 DIV) were washed with PBS twice (5 min each). Neurons were then fixed with 4% PFA for 15 min at RT, and washed with PBS twice (5 min each). Subsequently, the neurons were permeabilized with 0.3% Triton X-100 in PBS for 5 min at RT. The neurons were washed with PBS twice (5 min each) and blocked with the blocking solution (5% goat serum in PBS) for 1 h at RT. Samples were then incubated with the appropriate concentrations of primary antibodies in the blocking solution overnight at 4°C. At the end of the incubation, the neurons were washed with the blocking solution twice (5 min each), followed by two washing steps with the blocking solution for 20 min. The samples were incubated with the Alexa Fluor conjugated secondary antibodies diluted at 1:200 in a blocking solution for 2 h at RT in darkness. Filamentous actin (F-actin) was detected by incubating the fixed neurons with Alexa Fluor 532 Phalloidin for 2 h at RT. Finally, fixed neurons were washed with the blocking solution for 15 min twice.

3.2.11 Preparation of cerebellar slices

Euthanized mice were perfused transcardially with 0.2 M Sodium phosphate buffer (PB) containing heparin (10 I.U./ml), followed by infusion with a fixative solution (4% PFA in 0.2 M PB, pH 7.4) for 10 minutes. Brains were isolated and post-fixed with 4% PFA overnight at 4°C. Samples were then transferred to 30% sucrose in PBS for approximately 24 h. The next day, the cerebella were dissected from the rest of the brain then included in Tissue-Tek O.C.T. (Sakura Finetek, Alphen aan den Rijn, The Netherlands). Tissues were snap-frozen in an isopentane solution precooled with liquid nitrogen. Samples were then sliced into thin sections of 1.5 -2 nm using a Leica CM3050S cryostat. 18-mm round coverslips were passivated by silanization to block the glass and prevent non-specific binding. Coverslips were silanized by

soaking in silanization solution (composed of 2% 3-aminopropyltriethoxysilane in methanol) for 4 min, and then the coverslips were washed three times with distilled water then dried overnight. The slices were collected on the silanized coverslips and stored at - 80°C.

3.2.12 Immunofluorescence staining for cerebellar slices

Cerebellar slices were incubated with 0.02 M glycine in PBS to quench aldehyde groups. Samples were blocked and permeabilized by incubation with a blocking solution consisting of 1% bovine serum albumin, 5% normal goat serum and 0.3% Triton X-100 in PBS for 2 h at RT. Subsequently, samples were incubated with appropriate concentrations of the primary antibodies in the blocking solution overnight at 4°C. The primary antibodies were used in the following dilutions: guinea pig anti-mGluR4: 1:100 – 1:200 (stock solution concentration = 0.94 mg/ml), mouse anti-bassoon: 1:200 – 1:400, rabbit anti-bassoon: 1:200 – 1:400, rabbit anti-Ca_V2.1:200, and mouse anti-Munc 18-1: 1:400. In case of double labeling, slices were incubated simultaneously with both primary antibodies. At the end of the incubation, the slices were washed twice (10 min each) with the blocking solution, followed by two washing steps (40 min each) with the blocking solution. Sections were incubated with the Alexa Fluor conjugated secondary antibodies diluted at 1:200 in a blocking solution for 2 h at RT in darkness. The slices were washed twice (10 min each) with the blocking solution, followed by two washing steps (40 min each) with the blocking solution. The samples were kept in PBS at 4°C until imaging.

3.3 Microscope setups and data analysis

3.3.1 Confocal imaging

Confocal images were acquired with Leica true confocal scanner, 5 spectro-photometer (TCS SP5) (Leica Microsystems, Wetzlar, Germany), equipped with (63× oil-immersion, NA 1.4) objective. For excitation of AF 532 and AF647, 514 (100 mW Argon) and 633 nm (10 mW HeNe) laser lines were used. Images were acquired with image resolution of 1024 × 1024 pixels, and a scanning speed of 200 Hz, and then analyzed using Leica LAS-AF Application software. Further image processing was carried out on the public domain NIH Image program ImageJ/FIJI software.

3.3.2 *d*STORM imaging

As described previously[221] for reversible photoswitching, samples were embedded in a photoswitching buffer (freshly prepared) (100 mM β-mercaptoethylamine in PBS at a pH of 7.4 - 7.8). Superresolution imaging was performed on a custom-built Olympus IX-71 inverted

microscope, equipped with an oil-immersion objective (PlanApo 60x, NA 1.49, Olympus, Shinjuku, Tokyo, Japan), and a nosepiece stage (IX2-NPS, Olympus) to prevent focus-drift during imaging. For excitation of AF532 and AF647, 514 nm (500 mW) and 639 nm (1000 mW) solid-state lasers (OPSL, Genesis MX STM-Series, Coherent, Santa Clara, CA, USA) were used. Additionally, a suitable dichroic mirror (R442/514/635, Chroma, Bellows Falls, Vermont, USA) was installed to separate excitation from fluorescent light. The fluorescence emission of AF532 and AF647 dyes was acquired sequentially by the same objective, then projected separately by a dichroic mirror (630 DCXR customized, Chroma) on two EMCCD cameras (iXon Ultra 897, Andor, Belfast, Northern Ireland). The excitation intensities were in the range of 4 - 5 kW/cm² to enable sufficient photoswitching rates of the fluorophores. For each image, 40,000 frames were recorded with a frame rate of 60 Hz. The raw data were analyzed and the superresolution images were reconstructed using the open source software rapi*d*STORM 3.3[236]. The data ware generated as a list of localization coordinates and their intensities from the rapi*d*STORM.

3.3.3 Cluster analysis

Cluster analysis was performed using home-written algorithms in Mathematica 11.2. First, to gain a global assessment of the distribution of proteins, normalized Ripley's K function (Ripley's H function H(r)) was used[237]. A region of 32.9 x 32.9 µm² in the *d*STORM image was examined. Positive values of H(r) indicate significant clustering behavior, whereas negative values indicate dispersion. The r value corresponding to point of maximal aggregation (peak of H(r)) indicated the domain radius. For comparison with experimental data, simulated data were generated according to a Neyman-Scott point distribution. This distribution describes Poisson distributed localization clusters in a region of interest (ROI). The number of localizations within each localization cluster was 20 (mimicking the average number of localizations per mGluR4 localization cluster) with a standard deviation equal to 20. The data were also compared to a simulated data set with a complete spatial randomness.

Localization clusters were identified and grouped from isolated fluorophores using density-based spatial clustering of applications with noise (DBSCAN)[238]. The hierarchical clustering algorithm visits all localizations in the dataset, and assigns a localization into a localization cluster if it detects a core localization with neighboring localization numbers equal to or higher than the minimum number of neighboring points (minPTs) residing within a radius r. The algorithm then visits the next localization, if the conditions are not met (minPTs within radius r) the expansion stops and the boundary of the cluster is defined. The following DBSCAN parameters were selected to identify mGluR4 and bassoon localization clusters: bassoon (r = 60 nm and 20 minPts) and for mGluR4 (r = 16 nm and 4 minPts).

3.3.4 The orientation of the AZ analysis

First, AZs were identified by bassoon clusters filtered according to DBSCAN parameters of (r = 60 nm, 20 minPts), and AZ surface areas ranging from 100,000 to 600,000 nm². Secondly, the orientation of the AZ was identified to distinguish between synapses adopting *en face* or side view orientation. The orientation was identified based on the assessment of AZ circularity. For this analysis, two parameters were calculated: the inertia moment eccentricity (IME) and bounding box elongation (BBE). The IME is proportional to the ratio of length of the main axis to the minor axis along the main inertia moment of the localization distribution. The BBE is identified as one minus the ratio of the edge width of a smallest rectangular hull containing all localizations of the cluster distribution to the length of the BB. For both parameters a value ranging from 0 (perfect circular (*en face*) AZ) to 1 (elongated (side view) AZ) was calculated. The parameter couple of IME (min, 0.9) and BBE (min, 0.5) identified *en face* AZs. These parameters translate to *en face* AZs with a diameter ranging from 350 to 900 nm. For quantification analysis, twenty nm was added to the border limit of bassoon, to ensure that all localizations at the AZ's boarder are included.

3.3.5 Distance-based colocalization analysis

This analysis as described previously is a home-written routine in MATLAB environment to understand the spatial relationship between the localizations of two species [224]. The routine is based on adjustments on a method developed by Ibach (adopted from Mander's equation) [239, 240]. This analysis was conducted on original *d*STORM list of localizations without grouping the localizations into localization clusters (by any algorithm like DBSCAN) in order to avoid generating artefacts, and to maintain the robustness of the analysis by keeping high localization numbers[241]. The localizations in two channels (A and B) were binned to produce superresolved images with 5 x 5 nm pixel size. A binary mask was generated based on localizations in channel A to exclude regions with localization numbers lower than certain cut-off value. Colocalization index values, which measure the correlation between the fluorescence intensity from two channels were estimated in each pixel over increasing distance steps (5, 20, 40, 60, 80 and 100 nm). These distance values refer to the standard deviation width of a Gaussian filter applied to produce the images of channel A and B. Larger distance value produced lower resolution images. The colocalization index I was calculated according to the following equation.

$$I = \frac{(\langle B_{loc}\rangle - \langle B\rangle)\langle A\rangle}{\langle \mathrm{B}\rangle(\langle A_{loc}\rangle - \langle A\rangle)}$$

Defined for $\langle B_{loc}\rangle \geq \langle B\rangle$, where $\langle A_{loc}\rangle$, $\langle B_{loc}\rangle$ are the averages of the interpolated intensities of the two channel at each localization in A. ⟨A⟩, ⟨B⟩ are the mean intensities of channel A and

B, respectively. A simulation for completely randomized localizations was generated, to serve as a negative control. The sign of the index value indicates the direction of the correlation. Positive values indicate positive correlation and vice versa. Values equal to zero indicates the absence of correlation.

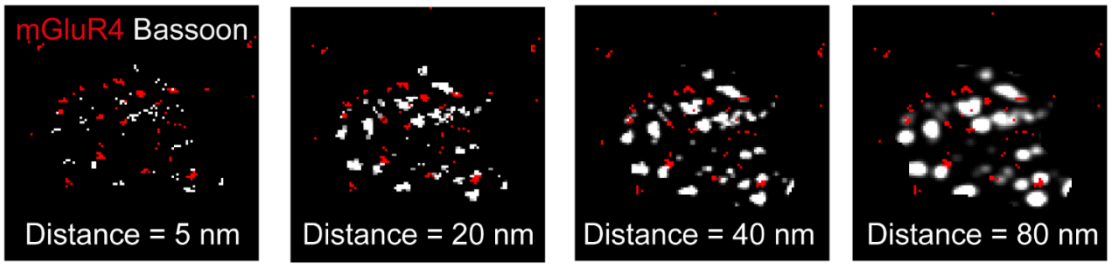

Figure 9: Principle of the distance-based colocalization analysis. Colocalization index values between localizations in channel A and B were calculated over increasing distances. These distance values refer to the standard deviation width of a Gaussian filter applied to produce the images of channel A and B.

3.3.6 Single-molecule total internal reflection microscopy

SNAP-tagged membrane receptors were visualized using a custom motorized Nikon Eclipse Ti total internal reflection fluorescence (TIRF) inverted microscope (Tokyo, Japan), equipped with (an oil immersion 100 x TIRF, NA 1.49) objective. The illumination was performed in a TIRF mode to generate an evanescent wave at the glass-medium interface to visualize receptors located at the plasma membrane. The fluorescence excitation was performed using 405 nm, 488 nm, 561 nm, and 640 nm diode lasers (Coherent, Santa Clara, CA, USA). The emitted light was projected to four separate EMCCD cameras (iXon3 DU897, Andor, Belfast, Northern Ireland). An incubator enclosing the microscope and the objective was kept at 20°C via a cooling water bath control system. The incubator was turned on an hour ahead of imaging to prevent temperature drifts. NIS Elements software (Nikon Instruments) was used to control the microscope. Region of interest was defined as 448 × 448 pixels. For each movie, 400 frames were recorded with a speed of 35 frames/s. Further image analysis was carried out on ImageJ software. Detection and tracking of single particles were conducted in the *u-track* software implemented in MATLAB as described previously[47]. The receptor density was calculated by dividing the total number of particles detected at the first frame of a movie by surface area of the cell. The surface area of the cell was estimated by manually drawing a ROI along the cell border.

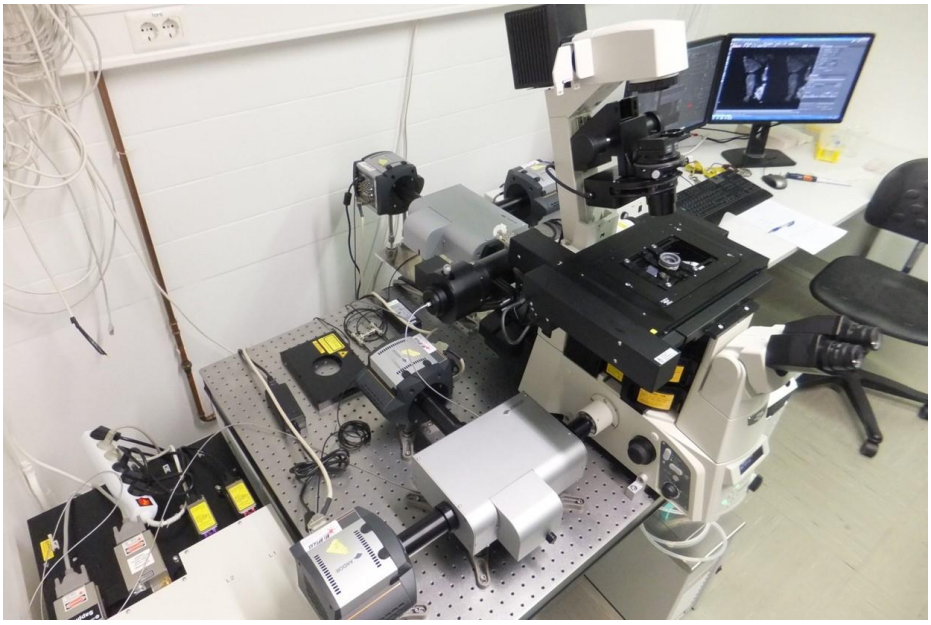

Figure 10: Single-molecule TIRFM setup. A custom motorized Nikon Eclipse Ti total internal reflection fluorescence (TIRF) inverted microscope.

3.3.7 Single-molecule intensity distribution analysis

The number of receptors per complex in single-molecule image sequences was estimated as previously described[47, 227]. Briefly, for each particle the intensities were estimated by averaging intensities from the beginning of the movie to the frame before the start of photobleaching (up to 20 frames). The distribution of the particle intensities was then fitted with a mixed Gaussian model, according to the following equation:

$$\varphi\,(i) = \sum_{n=1}^{n\,max} A_n \frac{1}{n\sigma\sqrt{2\pi}} e^{-\frac{(i-n\mu)^2}{2(n\sigma)^2}}$$

Where φ (i) is the frequency of particles with intensity i, n is the component number, A_n is the area under the curve of each component, and μ and σ are the mean and standard deviation of the intensity of the employed fluorophore, respectively. The intensity distribution of monomeric receptors (Alexa Fluor 647-labeled SNAP-CD86) was used as an initial estimate of μ and σ. However, because there might be minor differences in particle intensities among different image sequences, μ and σ were fine adjusted for each individual image. This is done by the estimation of the particle intensities at the last 60 frames (internal standard). This internal standard represents the intensity of single fluorophores after photobleaching of a large fraction of fluorophores. The relative abundance of each individual component was then calculated from A_n values.

3.3.8 Mean square displacement (MSD) analysis

The mean square displacement (MSD) is a home written routine in matlab to analyze the receptor trajectories generated from tracking single-molecule receptor motion utilizing TIRF microscopy. The diffusion coefficient (*D*) was computed by fitting the MSD with the following equation:

$$MSD\ (t) = 4Dt^{\alpha} + 4{\sigma_1}^2$$

Where t corresponds to time, α is the anomalous diffusion exponent and σ_1 is the standard deviation of the Gaussian localization error which was estimated to be ~ 23 nm. The trajectories generated from particles lasting for at least 120 frames were analyzed. Subsequently, trajectories were classified into four categories based on the two diffusion parameters *D* and α due to the observed motion heterogeneity. Particles with $D \leq 0.01\ \mu m^2 s^{-1}$ were considered to be immobile. Particles with $D \geq 0.01\ \mu m^2 s^{-1}$ and $0.75 \leq \alpha \leq 1.25$ were assigned to the normal diffusion (Brownian motion) category. Particles that had $D \geq 0.01\ \mu m^2 s^{-1}$ and $\alpha < 0.75$ or $\alpha > 1.25$ where assigned to the sub-diffusion (confined motion), and super-diffusion (directed motion) category, respectively. For the two-color TIRF movies, the area of synaptic and extrasynaptic compartments within the neuron was delineated manually using image J software. Finally, the MSD analysis was performed on trajectories in the corresponding compartment.

Statistics

Data are reported as mean ± s.e.m., unless otherwise indicated. Statistical analyses were conducted by Prism 6 software (GraphPad Software, La Jolla, CA, USA). Two-sided paired *t*-test was used to assess differences between two groups. Analysis of Variance (ANOVA) was used to assess differences between three or more groups, followed by Bonferroni's post hoc test. Differences were considered significant when $P < 0.05$.

4 Results

4.1 Nanoscopic organization of mGluR4 at presynaptic active zones

4.1.1 Conventional and *d*STORM imaging of mGluR4 spatial distribution at parallel fiber active zones

The focus of this study was to investigate mGluR4 organization at the active zone (AZ) of parallel fiber-Purkinje cell (PF-PC) synapses; model central synapses at the molecular layer (the outer layer) of the cerebellar cortex in mouse cerebellum. This synapse is one of the most abundant types of synapses in the brain and mGluR4 is highly expressed in these synapses[187, 192, 242, 243]. The PF-PC synapse model was selected also due to its highly organized structure, where the longitudinal PF axis intersects with the PC dendrites at a perpendicular angle **(Fig. 11)**. This orientation maximizes the chance of PC in receiving signals from granule cells. Moreover, these synapses provide the link between the major input pathway and the exclusive output pathway of the cerebellar network[244]. Thin cerebellar cryoslices were prepared. Coronal and sagittal slices (1.5 – 2 nm thickness) were prepared by slicing parallel or perpendicular to the parallel fiber main axis, respectively (**Fig. 11**). However, only coronal slices were used for imaging and further studies because this orientation provides a favorable anatomical view of the PF-PC synapses to study the protein spatial distribution and colocalization assessment. In the coronal orientation of slicing, most synapses are expected to be at *en face* view; the optical axis is perpendicular to the synapse main axis. Whereas for the sagittal slices, most synapses are expected to adopt the side view orientation; the optical axis is parallel to the synapse main axis.

Subsequently, I stained the cerebellar coronal slices prepared from adult wild-type FVB mice for endogenous mGluR4 and bassoon (presynaptic AZ scaffold protein marker) by indirect immunofluorescence. Confocal images showed that mGluR4 is enriched at the presynaptic AZs where bassoon is also highly concentrated (**Fig. 12a**). mGluR4 was recognized with a polyclonal antibody (kindly provided by Prof. Ryuichi Shigemoto, Institute of Science and Technology, Austria). The antibody selectively recognizes the mGluR4a splice variant, and I will refer to it in this study as mGluR4 (as the two splice variants mGluR4a and mGluR4b have different C-termini[245, 246]). The antibody was generated against a synthetic peptide corresponding to the 890-912 amino acid residue of rat mGluR4 C-terminal. Specificity of the antibody was previously verified by immunoblot analysis of membrane fractions from the rat hippocampus and membrane fractions prepared from CHO cells transfected with mGluR4a,

mGluR7a, mGluR7b, and mGluR8[125, 192]. Furthermore, I also tested the specificity of this antibody on cerebellar slices obtained from mGluR4 knockout mouse generated from another project in our group aiming to establish SNAP-mGluR4 knockin mice using CRISPR/Cas9 technology (**Fig. 12b**).

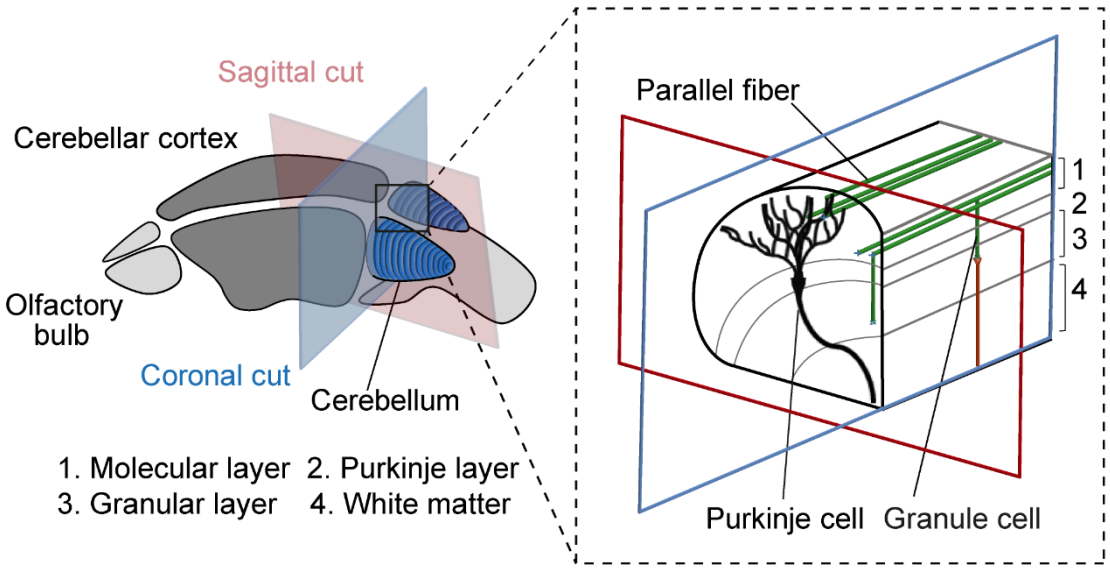

Figure 11: Schematic description of the orientation in cutting cerebellar slices. Left, scheme depicting the brain and the orientation of the coronal and sagittal cutting planes. The coronal cutting plane (blue) is parallel to the parallel fiber main axis. The sagittal cutting plane (red) is perpendicular to the parallel fiber main axis. Right, enlargement of boxed region within the cerebellum. Shown is the ordered arrangement of the parallel fibers (green), which originate from granule cells and form dense synapses with the dendritic spines of Purkinje cells (black).

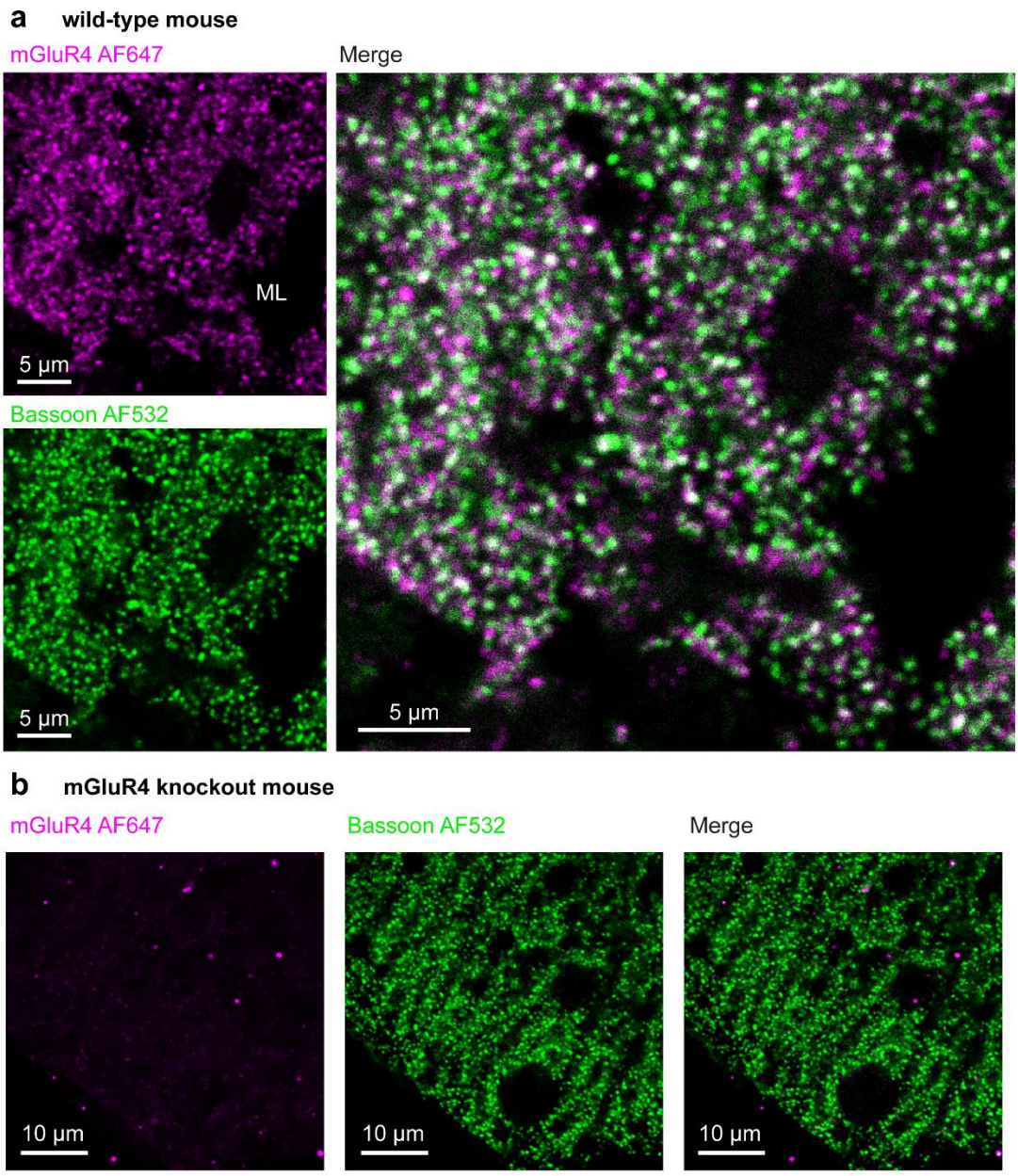

Figure 12: Confocal images of cerebellar slices stained for endogenous mGluR4 and bassoon by double indirect immunofluorescence. Confocal images of mGluR4 (magenta) and bassoon (green). Shown are representative confocal images acquired in regions corresponding to the molecular layer from coronal cerebellar slices. The slices were obtained from **(a)** wild-type and **(b)** mGluR4 knockout mice. Slices were stained for endogenous mGluR4 (magenta) and bassoon (green) simultaneously by guinea pig polyclonal α-mGluR4 and mouse monoclonal α-bassoon, respectively. Primary antibodies were recognized by AF647-conjugated α-guinea pig and AF532-conjugated α-mouse secondary antibodies, respectively. ML: molecular layer, AF: Alexa Fluor dye.

Confocal microscopy does not provide enough resolution to reveal the nanoscopic organization of mGluR4 due to the diffraction limit of light microscopy[204]. Therefore, I utilized two-color *direct* stochastic optical reconstruction microscopy (*d*STORM) to image native mGluR4 organization. The achieved localization precision (σ) was ~ 13 nm in the lateral direction. The presynaptic AZs detected by bassoon staining adopted disc-like shape at *en face* view synapses, while AZs at side view synapses adopted bar-like shapes (**Fig. 13a,b,c**). The vast majority of presynaptic varicosities showed mGluR4 enrichment at the AZs (**Fig. 13**). In contrast, slices stained with just the secondary antibody showed only a negligible signal (**Fig. 13d**).

Within AZs, clustered mGluR4 organization rather than homogenous distribution of individual receptors was observed, where the receptors appeared to be organized in small clusters (localization clusters). In *d*STORM method, one target molecule labeled by Alexa Fluor dye generates several localizations due to binding of more than one secondary antibody to the primary antibody. Additionally, each secondary antibody is conjugated to multiple fluorophores and each fluorophore blinks several times during image acquisition. Therefore, Ripley's H analysis was performed to confirm that the nature of mGluR4 clustered organization is biological and is not simply a result of fluorophore photoswitching characteristics. The analysis confirmed this finding and indeed revealed features of mGluR4 spatial clusters. The Ripley's H function obtained for mGluR4 displayed a bimodal shape (**Fig. 14a**), with a point of maximal aggregation (peak of H(r)) around 101 nm and this value was significantly higher than a simulated Neyman-Scott point distribution (peak of H(r) was 60 nm) and completely randomized localizations. The Neyman-Scott point distribution was simulated to distribute 20 localizations per cluster (mimicking the average number of localizations per mGluR4 localization cluster; explained in more details in the method, **section 3.3.3**) and a sigma of the probability density function of 20 nm. Those clusters were randomly distributed across the plane. The detected shoulder around 240 nm from mGluR4 Ripley's H function could be explained by mGluR4 preferential localization at AZs, as bassoon localizations displayed similar peak (**Fig. 14a**).

In order to estimate mGluR4 degree of enrichment at the AZ, average mGluR4 localizations within *en face* AZs were calculated and compared to the localization density outside AZs. First, AZs were identified based on bassoon localizations using the DBSCAN[238] clustering algorithm followed by automated detection for the selection of AZs displaying *en face* orientation (refer to the method, **section 3.3.4** for details) and the surface area was calculated. The surface area of AZs showed a broad distribution (mean = $21.63 \pm 0.38 \times 10^4$ nm^2; range = 10.02×10^4 – 58.14×10^4 nm^2) (**Fig. 14c**). Secondly, mGluR4 localizations inside and outside

AZs were calculated. Outside AZs area is defined as area within 2000 nm orthogonal distance from the AZ border. While AZs contain on average $2.10 \pm 0.38 \times 10^{-3}$ mGluR4 localizations/nm^2, $0.59 \pm 0.38 \times 10^{-4}$ mGluR4 localizations/nm^2 were detected outside AZs. Based on these localization densities, mGluR4 was about four-fold concentrated inside AZs compared to outside AZs (**Fig. 14d**). Ripley's H analysis, DBSCAN, and the AZ orientation analysis were performed by Dr. Sarah Aufmkolk from the group of Prof. Sauer.

In short, two-color *d*STORM imaging of cerebellar slices revealed that mGluR4 is arranged in small nanoscale clusters (nanodomains) with four-fold higher enrichment within parallel fiber AZs in comparison to outside AZs.

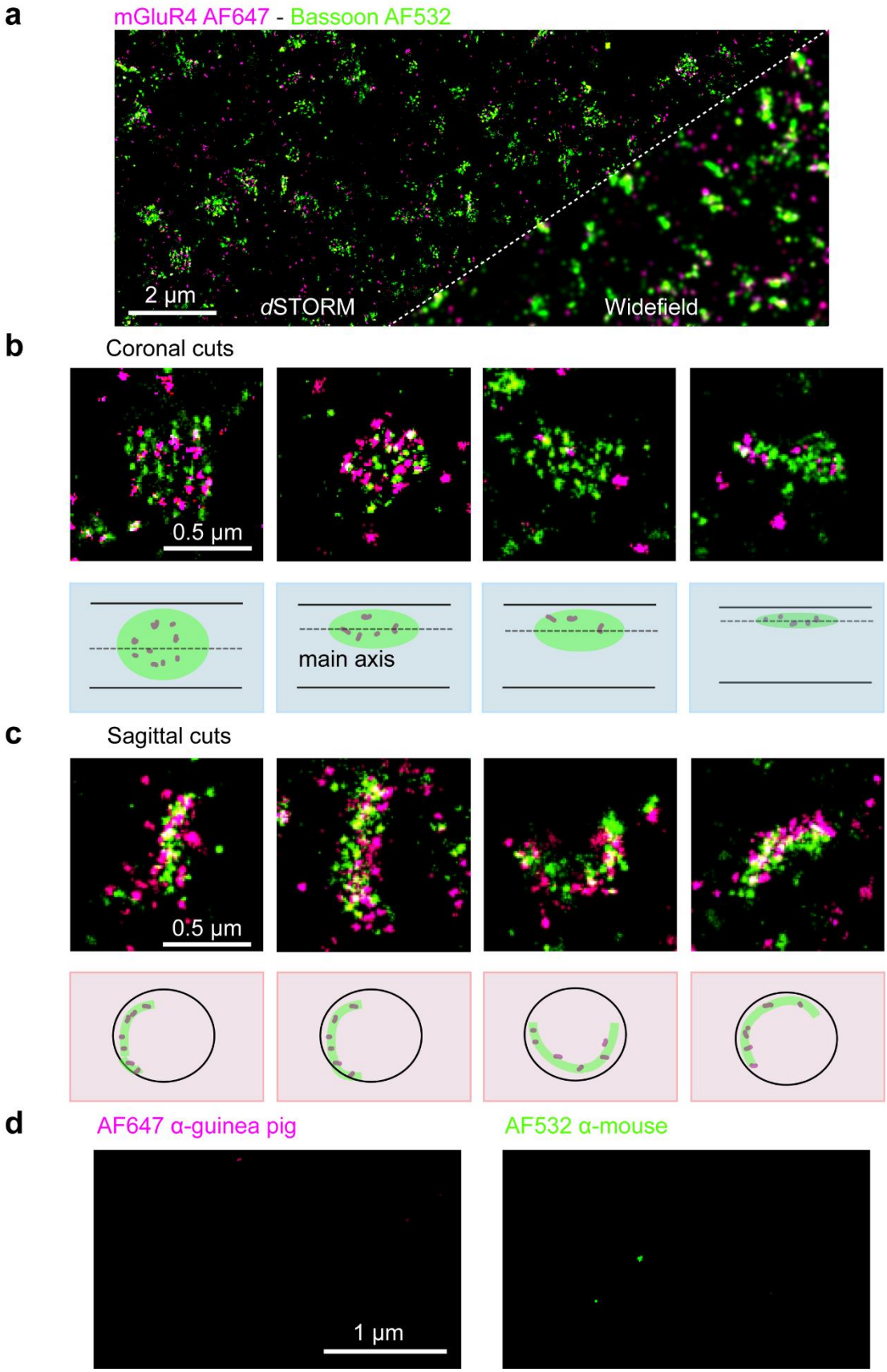
a
mGluR4 AF647 - Bassoon AF532
2 µm
dSTORM
Widefield
b
Coronal cuts
0.5 µm
main axis
c
Sagittal cuts
0.5 µm
d
AF647 α-guinea pig
AF532 α-mouse
1 µm

Figure 13: Superresolution (*d*STORM) imaging reveals the nanoscale organization of mGluR4 at parallel fiber AZs. (a) Two-color *d*STORM imaging of mGluR4 (magenta) and bassoon (green). Shown is a representative image of a coronal slice acquired in a region corresponding to the molecular layer of the cerebellum. An artificial widefield image is given for comparison. Enlarged views of representative AZs imaged in either **(b)** coronal or **(c)** sagittal slices. *En face* AZs presented disk-like shapes with different degrees of flattening, while side view synapses presented bar-like shapes. **(d)** Negative control for mGluR4 immunofluorescence staining. Representative *d*STORM images of cerebellar slices stained with AF 647-conjugated α-guinea pig secondary antibody (left) or AF 532-conjugated α-mouse secondary antibody (right) simultaneously to serve as a negative control. Images in b and c are representative of 2 and 4 independent experiments, respectively.

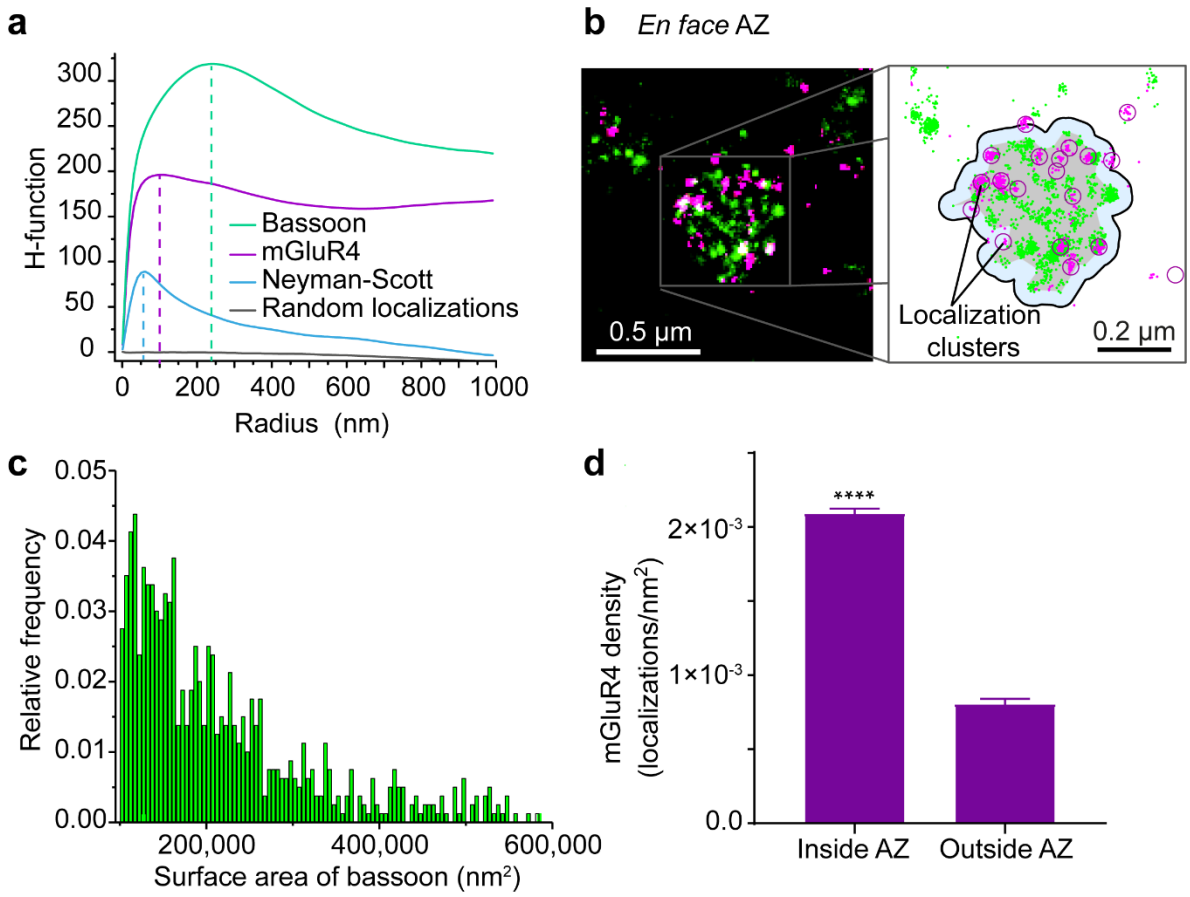

Figure 14: Clustering and quantification of mGluR4 at the presynaptic AZs. (a) Ripley's H function analysis investigating the clustering of mGluR4 (magenta). Data were compared with a Neyman-Scott distribution (blue) (n = 20, σ= 20 nm) to simulate randomly distributed localization clusters as well as with entirely random localizations (black). Ripley's H function analysis of bassoon was also performed (green). **(b)** Principle of the mGluR4 quantification analysis. Gray shaded area indicates e*n face* AZs which were identified based on the bassoon localizations (green clusters) using the DBSCAN analysis followed by the AZ orientation analysis. Twenty nm was added to the border limit of bassoon (blue shaded area). mGluR4 nanoclusters (magenta circles) were subsequently identified based on the mGluR4 localizations (magenta dots) using DBSCAN. **(c)** Histogram of the surface area of analyzed *en face* AZs. **(d)** Comparison of mGluR4 localizations density detected inside and outside AZs. Outside AZs area is defined as area within 2000 nm orthogonal distance from the AZ border. (n=799 AZs), ****P<0.0001 by two-sided paired *t*-test.

4.1.2 Oligomeric state of mGluR4 complexes in CHO cells

Next, I aimed to characterize the oligomeric state of mGluR4 (monomers, dimers or higher order oligomers). To tackle this question, I applied single-molecule total internal reflection fluorescence microscopy (TIRFM) for the identification of GPCR supramolecular organization. The applied approach combines single-molecule imaging and labeling via the SNAP/CLIP-tags technology[47, 227, 228].

First, in order to validate the method with positive controls, SNAP-CD86 and SNAP2×-CD86 membrane receptors were used to represent virtual monomers and dimers, respectively. CD86 receptor was engineered to insert either one SNAP-tag (SNAP-CD86) or two SNAP-tags (SNAP2×-CD86) at the extracellular N-termini (**Fig. 15a,d**). Then, CHO cells were transiently transfected to express SNAP-CD86 or SNAP2×-CD86 at low physiological levels (0.29 ± 0.07) and (0.40 ± 0.1) (s.d.) particles/μm^2, respectively. Subsequently, receptors were covalently labeled with a saturating concentration (2 µM) of a fluorescent SNAP substrate (SNAP-Surface Alexa Fluor 647). Cells were then fixed with 4% PFA and images were acquired by fast TIRF microscopy. Individual fluorescent particles were observed (**Fig. 15b,e**). Finally, the distribution of the automatically detected and tracked particle intensities was fitted to a mixed Gaussian model in order to estimate the relative abundance of the underlying components (monomers, dimers, higher order oligomers). As expected, the analysis of SNAP-CD86 particle distribution intensity revealed a single predominant peak (94 ± 0.05 %). This peak overlapped with the peak corresponding to the intensity of an internal standard representing single fluorophores. This internal standard was obtained by performing a mixed Gaussian fit on the intensity distribution of particles at the end of the movies (last 60 frames) (**Fig. 15c**). On the other hand, the mixed Gaussian fitting analysis of SNAP2×-CD86 showed broader intensity distributions and the predominant peak (79 ± 0.03%) was shifted to the right, consistent with the dimeric nature of this construct. A minor peak (21 ± 0.03%) was observed due to the presence of higher order oligomers (15 ± 0.02% trimers and 5% tetramers, pentamers and hexamers) (**Fig. 15f**).

Next, I performed similar experiments to study the oligomeric state of mGluR4. CHO cells were transfected with a plasmid encoding SNAP-mGluR4, resulting in SNAP-mGluR4 expression at low/physiological densities (0.48 ± 0.09 particles/μm^2). SNAP-mGluR4 was labeled with 1:1 stoichiometry with AF647 then imaged with TIRFM (**Fig. 16a,b**). Quantitative analysis revealed that a large fraction of SNAP-mGluR4 population is homodimeric (71 ± 0.03%) and 29% of the population is in the form of higher ordered oligomers (19 ± 0.04% trimers, 4 ± 0.02% tetramers and 4 ± 0.01% pentamers) (**Fig. 16c,d**).

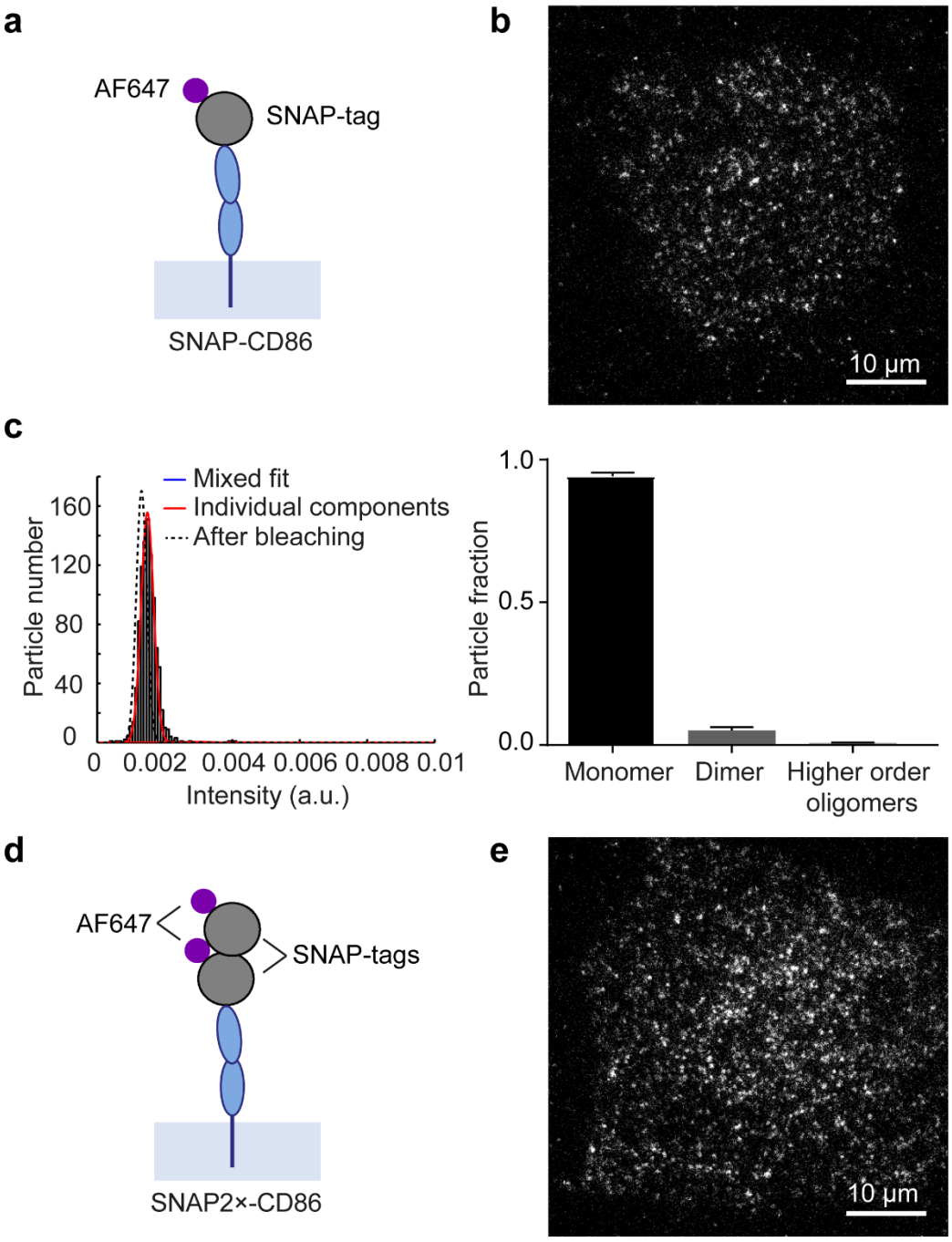
a
AF647
SNAP-tag
SNAP-CD86
b
10 μm
c
Mixed fit
Individual components
After bleaching
Particle number
160
120
80
40
0
0 0.002 0.004 0.006 0.008 0.01
Intensity (a.u.)
Particle fraction
1.0
0.5
0.0
Monomer
Dimer
Higher order oligomers
d
AF647
SNAP-tags
SNAP2×-CD86
e
10 μm
f
mixed fit
individual components
after bleaching
Particle number
120
80
40
0
0 0.002 0.004 0.006 0.008 0.01
Intensity (a.u.)
Particle fraction
1.0
0.8
0.6
0.4
0.2
0.0
Monomer
Dimer
Higher order oligomers

Figure 15: Validation of the single-molecule TIRFM method. Schematic view of CD86 constructs carrying either **(a)** one or **(d)** two SNAP-tag copies at their N-terminal domains to assess the expected monomeric and dimeric intensity distributions. Representative TIRF images of fixed CHO cells expressing **(b)** SNAP-CD86 or **(e)** SNAP2×-CD86. Dots represent individual receptor particles, which were identified and tracked with an automated single-particle detection algorithm. Representative intensity distributions (left) of **(c)** SNAP-CD86 and **(f)** SNAP2×-CD86. The intensity distribution of the fluorescence spots was fitted with a mixed Gaussian model, followed by quantification of the monomeric, dimeric and oligomeric subpopulation (right). The intensity of an internal standard of single fluorophores at the end of each movie was fitted with the mixed Gaussian model (dotted black line) as a reference for intensity distribution of a monomer. n=14 cells (10,290 particles) and n=13 cells (12,415 particles) for a-c and d-f, respectively, from three independent experiments.

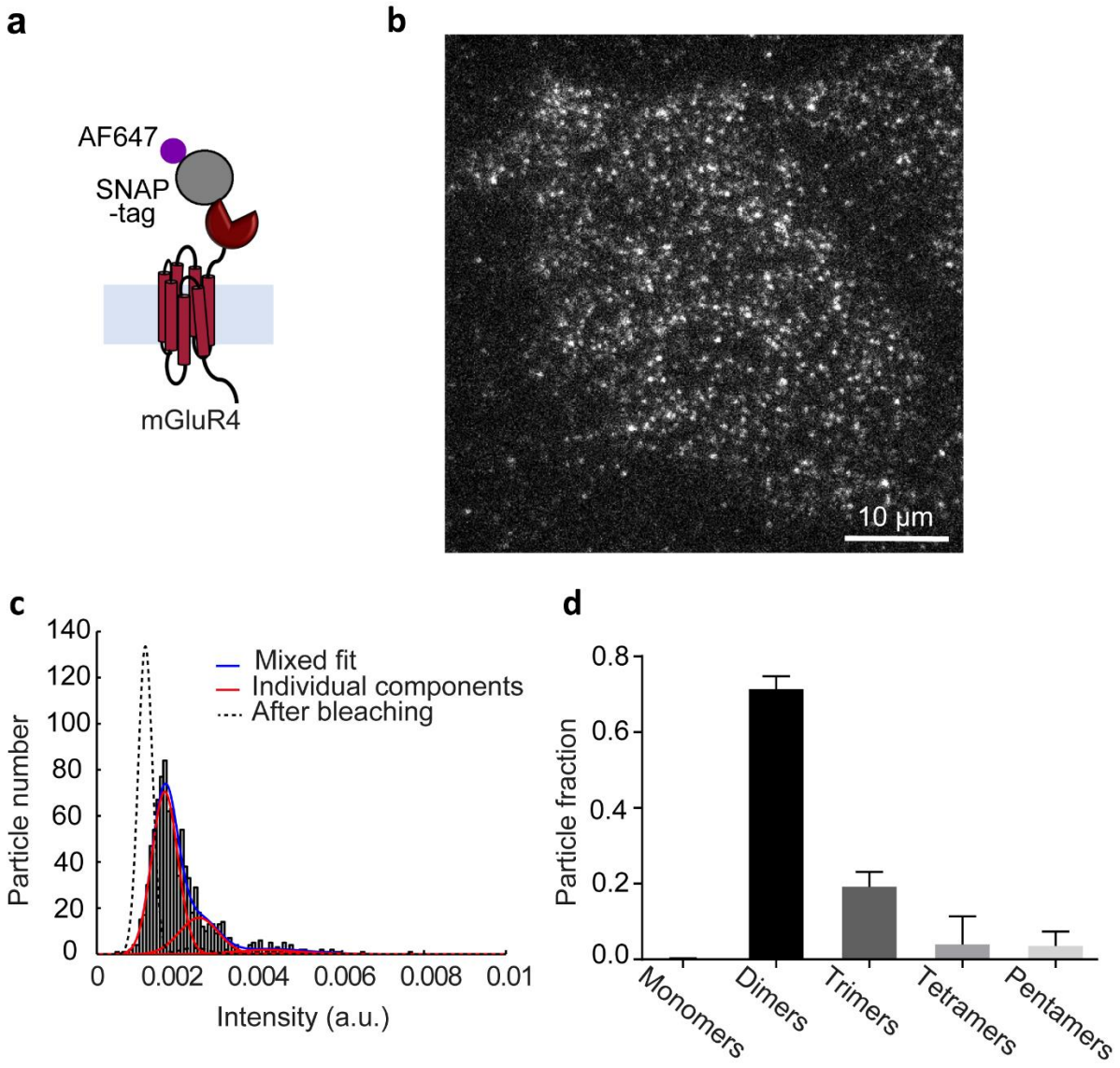

Figure 16: Analysis of mGluR4 oligomeric state by single-molecule TIRFM. (a) Schematic view of the mGluR4 construct carrying an N-terminal SNAP-tag. **(b)** Representative TIRF image of a fixed CHO cell expressing the SNAP-mGluR4 construct. Dots represent individual receptor particles, which were identified with an automated single-particle detection algorithm **(c)** Representative distribution of the intensity of mGluR4 particles. Data were fitted with a mixed Gaussian model. The intensity of an internal standard of single fluorophores at the end of each movie was fitted with the mixed Gaussian fitting (dotted black line) as a reference for intensity distribution of a monomer. **(d)** Relative abundance of monomers, dimers and higher-order oligomers detected by the analysis. n= 11 cells (15,658 particles) from three independent experiments.

4.1.3 Number and stoichiometry of mGluR4 nanoclusters within active zones

A substantial bottleneck for understanding underlying GPCR mechanisms of actions include the visualization of GPCR stoichiometry on the surface of AZs. Therefore, the next aim was to extract quantitative information regarding the number of receptors within single mGluR4 nanocluster and the number of mGluR4 receptors expressed per active zone. Thus, a series of experiments were conducted to: first, estimate number of mGluR4 primary antibodies binding to one receptor and secondly, to estimate the average number of localizations from a single mGluR4 localization cluster.

To attain information regarding the number of primary antibodies bound to one receptor (number of epitopes/receptor), a single-molecule based strategy was developed. CHO cells were transfected with wild-type mGluR4 to express physiological concentration of the receptor (0.55 ± 0.07 (s.d.) particles/μm^2). The cells were fixed with 4% PFA then stained for two different conditions. For the first condition, cells were stained with a saturating concentration of the primary antibody (1:100, stock solution concentration = 0.94 µg/µl) to ensure that all accessible epitopes of mGluR4 complex are saturated with the primary antibody (saturating condition). In a second condition, the cells were stained with very low concentration of the primary antibody ($1:10^6$) to ensure that only one epitope per mGluR4 complex is occupied (low labeling condition). The concentration of the secondary antibody was fixed for both conditions (1:200), which was a saturating concentration. Images were then acquired by TIRFM. Mixed Gaussian fitting was performed on the distribution intensities of individual fluorescent spots. The resultant intensity distributions were complex showing three of more subpopulations as a result of potential presence of multiple epitopes, mGluR4 supramolecular structure, binding of multiple secondary antibodies to one primary antibody, in addition to the contribution of multiple fluorophores conjugated to the secondary antibody (**Fig. 17**). For the low labeling condition, the intensity of the first subpopulation corresponds to the smallest mGluR4 complex detected by one primary antibody per complex and the minimum possible number of secondary antibodies and conjugated fluorophores. Whereas, for the saturating condition, first peak corresponds to completely saturated epitopes within mgluR4 complex, detected by the minimum possible number of secondary antibodies and conjugated fluorophores. The ratio of first peak intensity of saturating condition to the one at very low labeling condition corresponds to the number of epitopes per mGluR4 dimer, which was 1.8 ± 0.22. This value indicates that only one primary antibody binds per single mGluR4 taking into account the dimeric nature of mGluR4 as revealed in the previous section (the ratio 1.8 divided by 2). The finding that the binding stoichiometry for the primary antibody is 1:1 is consistent with the nature of the primary

antibody, which was generated by immunizing guinea pigs with a small synthetic peptide (23 amino acids).

In parallel, *d*STORM imaging of slices stained with increasing primary antibody concentrations was carried out to construct the titration curve. DBSCAN analysis calculated the number of mGluR4 localizations arising from staining with each primary antibody dilution. The average values were then fitted to a logistic function to estimate the number of localizations per nanocluster in a saturating and limiting dilution conditions (**Fig. 18**). 1:100 primary antibody dilution was found to saturate mGluR4 nanoclusters, subsequently the number of mGluR4 localizations arising from this dilution was used to quantify mGluR4 within the nanoclusters, and at the AZs. Briefly, the ratio of the highest number of mGluR4 localizations corresponding to the saturating primary antibody concentration (20.87 ± 1.00) to the lowest localization number arising from limiting dilution (single receptor per mGluR4 is recognized by the primary antibody) (14.90 ± 0.85) provided an approximation of mGluR4 number residing with individual nanocluster. The ratio which was 1.40 ± 0.11, indicates that each mGluR4 nanocluster contains 1 - 2 receptors on average. Moreover, the distribution obtained at the saturating concentration was broader than the one obtained under limiting dilution conditions. The distribution of localizations corresponding to saturated nanocluster indicates that each mGluR4 nanocluster contains minimum 1 to a maximum of 5 receptors (**Fig. 18b**).

In order to estimate the number of mGluR4 nanoclusters within each AZ, the number of mGluR4 localizations per *en face* active zone was calculated. The number of mGluR4 localizations varied considerably between synapses indicating a high heterogeneity. The mean value was 522 ± 13 localizations/AZ. On average 29 mGluR4 nanoclusters were estimated per AZ, each containing one or two mGluR4s, with few nanoclusters possibly containing three or more receptors (**Fig. 19**).

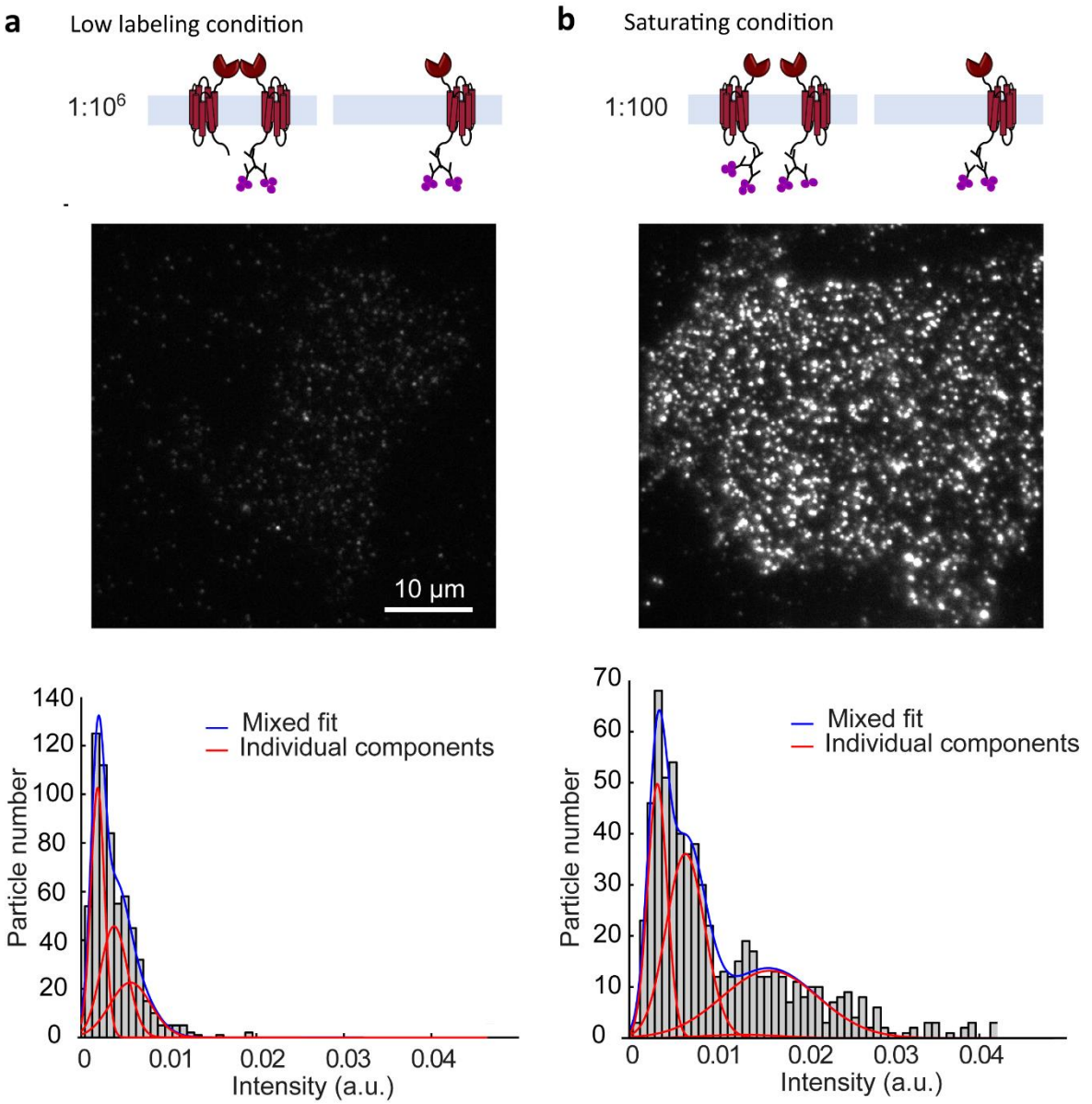

Figure 17: Estimation of mGluR4 number of epitopes by single-molecule TIRFM based approach. CHO cells transiently transfected to express wild-type mGluR4 at low densities were fixed and then incubated with either **(a)** a low labeling dilution (1:10^6) or **(b)** a saturating concentration (1:100) of the primary antibody against mGluR4. The receptors were labeled with an Alexa Fluor 647-conjugated secondary antibody. Imaged were acquired and particles were detected and tracked and their intensity distributions were fitted with a mixed Gaussian fitting. Shown are representative TIRF images and distribution of the intensity of mGluR4 particles of 20 cells (17,257 particles) for (a) and 22 cells (13,553 particles) for (b), from three independent experiments.

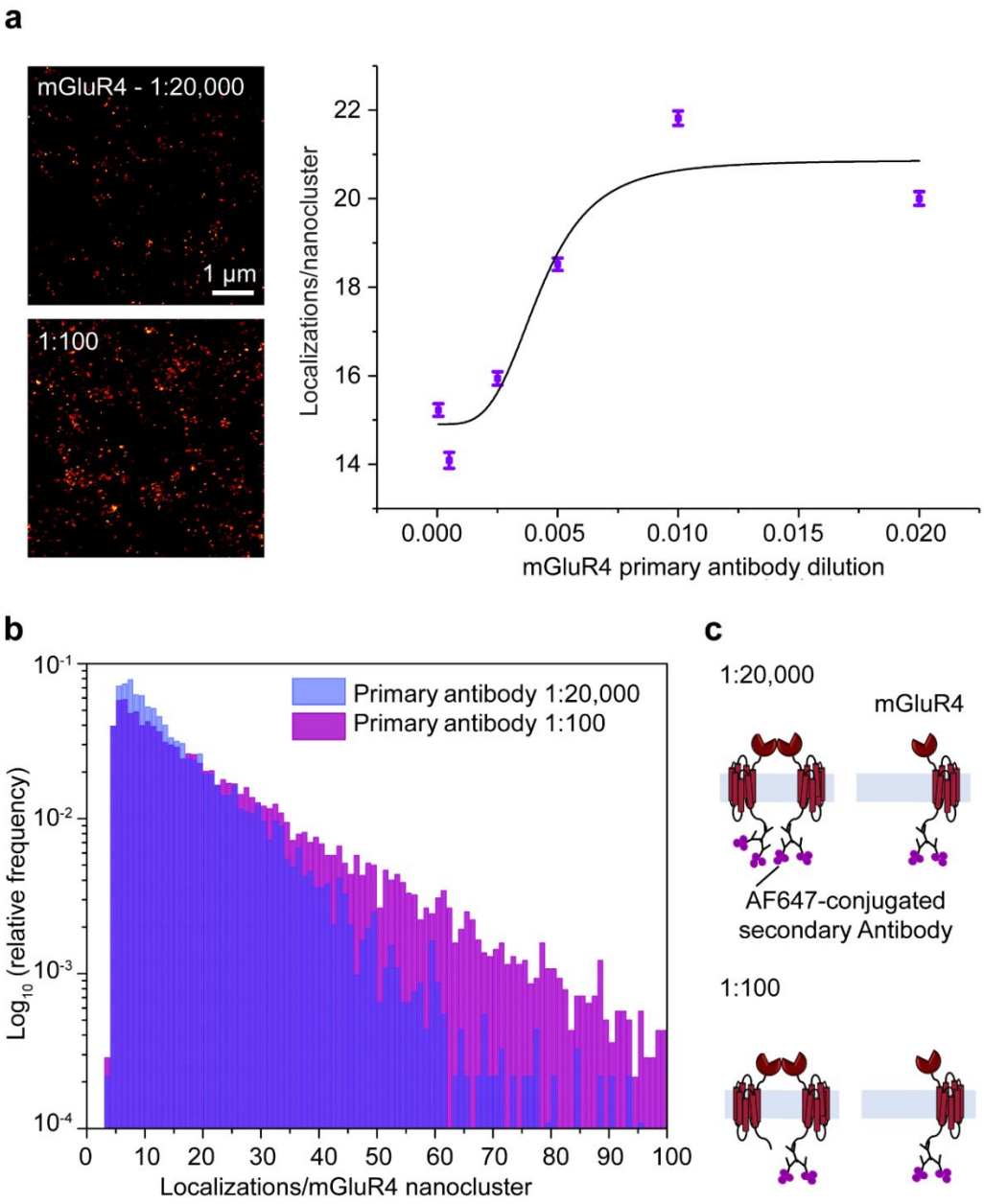

Figure 18: Stoichiometry of mGluR4 complexes at AZs. (a) Titration curve of the primary antibody against mGluR4. Left, representative *d*STORM images of cerebellar slices stained with either a limiting dilution (1:20,000) or a saturating concentration (1:100 dilution) of the α-mGluR4a antibody. Right, titration curve constructed by plotting mGluR4 localizations/nanocluster over six different primary antibody dilutions (1:50, 1:100, 1:200, 1:400, 1:2000, 1:20,000). Data was fitted with a logistic function. **(b)** Distributions of the number of localizations per nanocluster measured with either limiting dilution or saturating concentration of the primary antibody, n = 9,205 and 13,974 nanoclusters, respectively. (**c**) Schematic view of the results, showing the effect of varying concentrations of the primary antibody on the number of secondary antibodies, therefore changing the number of localizations, detected for a nanocluster.

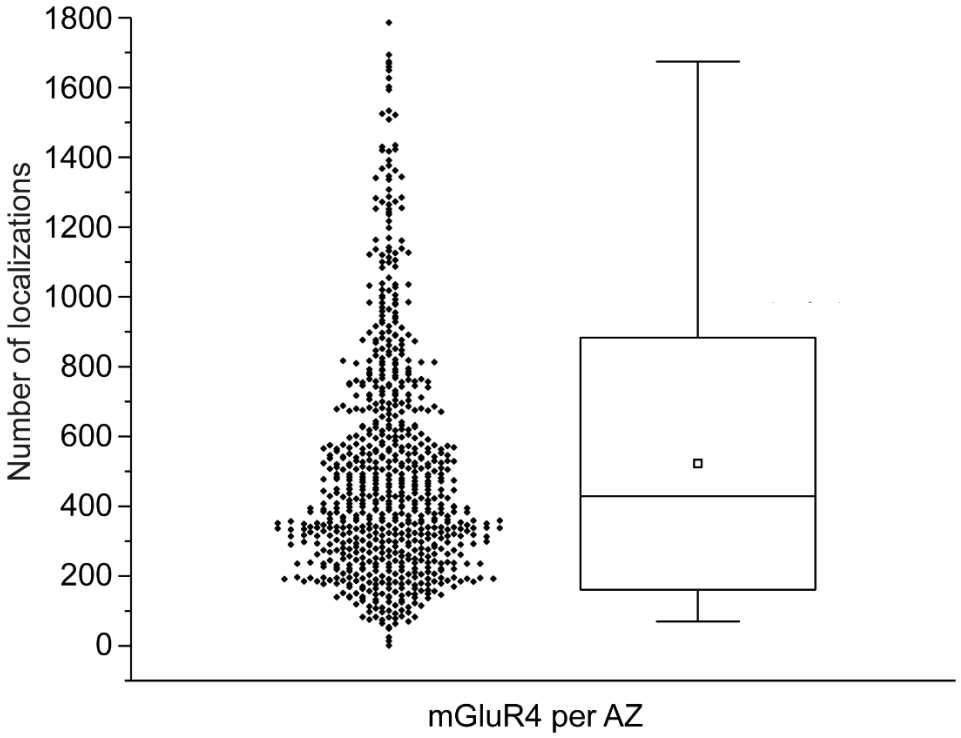

Figure 19: Quantification of mGluR4 nanoclusters in the parallel fiber AZ. Box chart showing the number of mGluR4 localizations per parallel fiber AZ, mean= 522.1123 (square) and median= 429 (line), n = 699 AZs.

4.1.4 Substructural arrangement of mGluR4 relative to $Ca_V2.1$ channels

Moving towards a different level of mGluR4 nanocluster organization, I also studied mGluR4 spatial organization with respect to $Ca_V2.1$ channels, which are the most abundant type of VDCC in the cerebellum and mediates strong PF activation[247, 248]. Cerebellar slices were stained for native mGluR4 and endogenous $Ca_V2.1$ and images were acquired by confocal microscopy. Subsequently, images were acquired using *d*STORM to reveal nanoscopic substructural details. The $Ca_V2.1$ antibody was generated against the $\alpha\text{-}_{1A}$ subunit of the *P/Q-type* Ca^{2+} channel (amino acid residues 856 to 888). Confocal images showed intense $Ca_V2.1$ staining throughout the molecular layer (ML) as previously reported (**Fig. 20a**)[92, 249]. *d*STORM images revealed apparent colocalization between mGluR4 and $Ca_V2.1$ channels. In order to evaluate the degree of colocalization between mGluR4 and $Ca_V2.1$, a distance-based localization analysis was used. The distance-based colocalization analysis was developed by the Prof. Calebiro's group for the assessment of the correlation between GPCRs and various scaffolding and cytoskeleton proteins[224, 225]. The analysis demonstrated to be robust as it is directly applied to analyze the list of coordinates and is independent on the parameters selected to create the intensity based superresolved image. Additionally, we are analyzing

individual proteins rather than averages. One antibody (IgG) has a size of 7-10 nm[250, 251], meaning that a marker made of one primary and one secondary antibody has a size of ~15-20 nm. Thus, distances starting from 30 nm are most relevant to us when we want to evaluate the proximity of two targets. As a positive control, cerebellar slices were stained for bassoon using two different antibody species both targeting bassoon epitopes. Colocalization index values ranged between 0.2 and 0.6 at 20 nm and 100 nm, respectively (**Fig. 20**). These values serve as a reference for us to evaluate the degree of correlation between various targets.

Distance-based colocalization analysis revealed a positive correlation between mGluR4 and bassoon at 40-100 nm scale based on the positive colocalization index values (**Fig**. **21**). As expected, the correlation values were higher at longer distances. The positive correlation was not due to random chance as statistical significance was obtained when comparing the actual localization distribution to a situation where mGluR4 localizations were scrambled and distributed randomly (bassoon localizations were not altered). Higher degree of positive correlation was observed between mGluR4 and $Ca_V2.1$. Statistically significant correlation was detected at shorter distance (20 nm), which is below the localization uncertainty introduced by the antibodies and the localization error (**Fig**. **21**), although $Ca_V2.1$ is less concentrated at AZs in comparison to bassoon as observed in *d*STORM images. Kulik et al. also reported high $Ca_V2.1$ expression at the PF varicosities and dendritic spines of PCs, and weak $Ca_V2.1$ expression at the dendritic shafts of PCs[249]. Distance-based colocalization analysis revealed that at least a fraction of mGluR4 is located in close proximity to $Ca_V2.1$. This result suggest that, mGluR4 might interact directly or indirectly with $Ca_V2.1$.

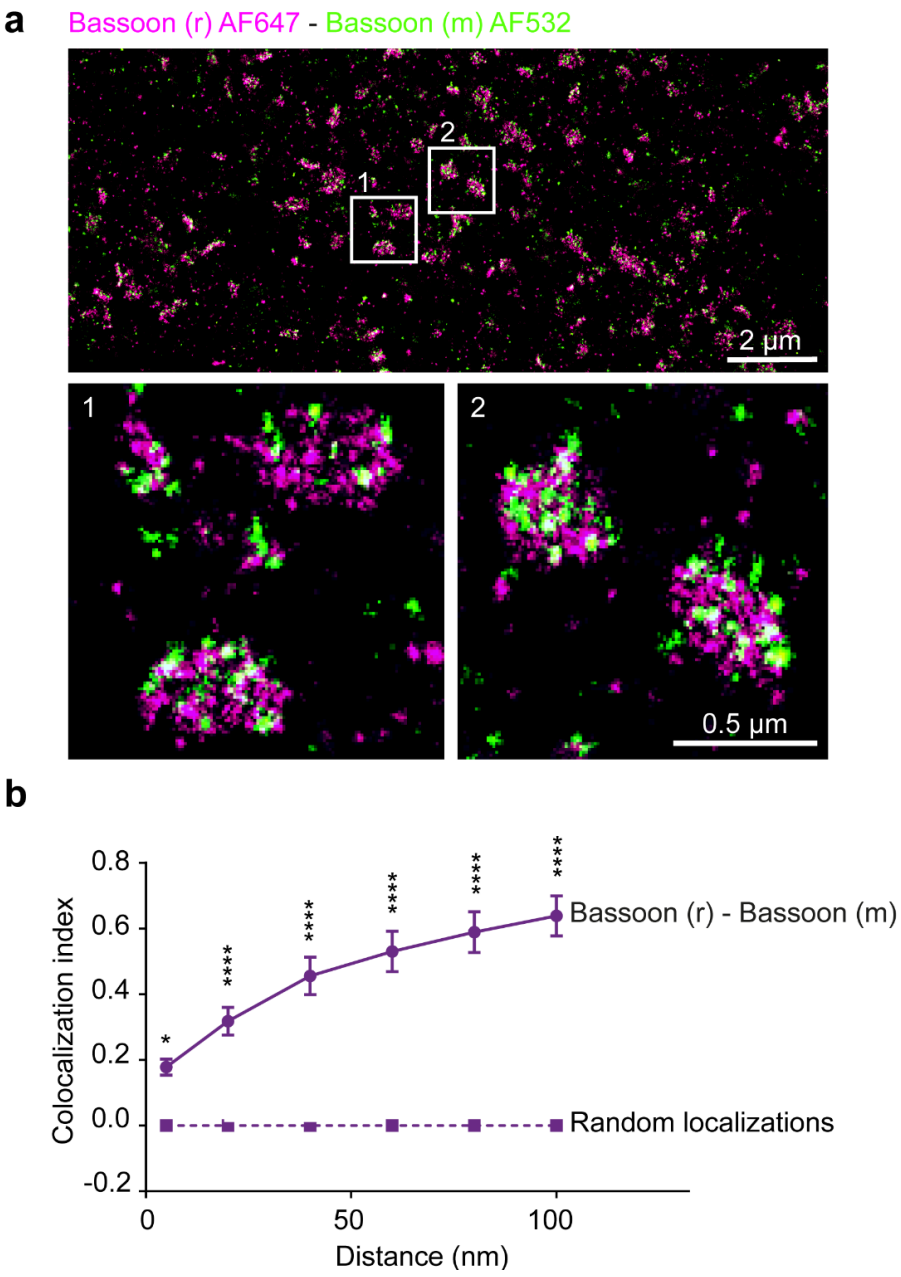

Figure 20: Validation of the distance-based colocalization analysis. (a) A representative two-color *d*STORM image of a cerebellar slice revealing bassoon clusters co-immunostained using two different antibodies raised either in rabbit (r) (magenta) or in mouse (m) (green). Images were acquired in a region corresponding to the molecular layer of the cerebellum. Lower panel, 1-2 enlarged images of two boxed regions. **(b)** Distance based colocalization analysis. Shown is the quantification of colocalization index values over increasing distances (Gaussian filter width). Colocalization index values (continuous line) were compared to values resulting from correlation between randomly scrambled bassoon (r) localizations and bassoon (m) localizations (dashed line). n = 3 regions of 16 × 16 µm^2 from one preparation. Differences were statistically significant by two-way ANOVA. *P < 0.05 and ****P < 0.0001 versus random localizations by Bonferroni's post hoc test.

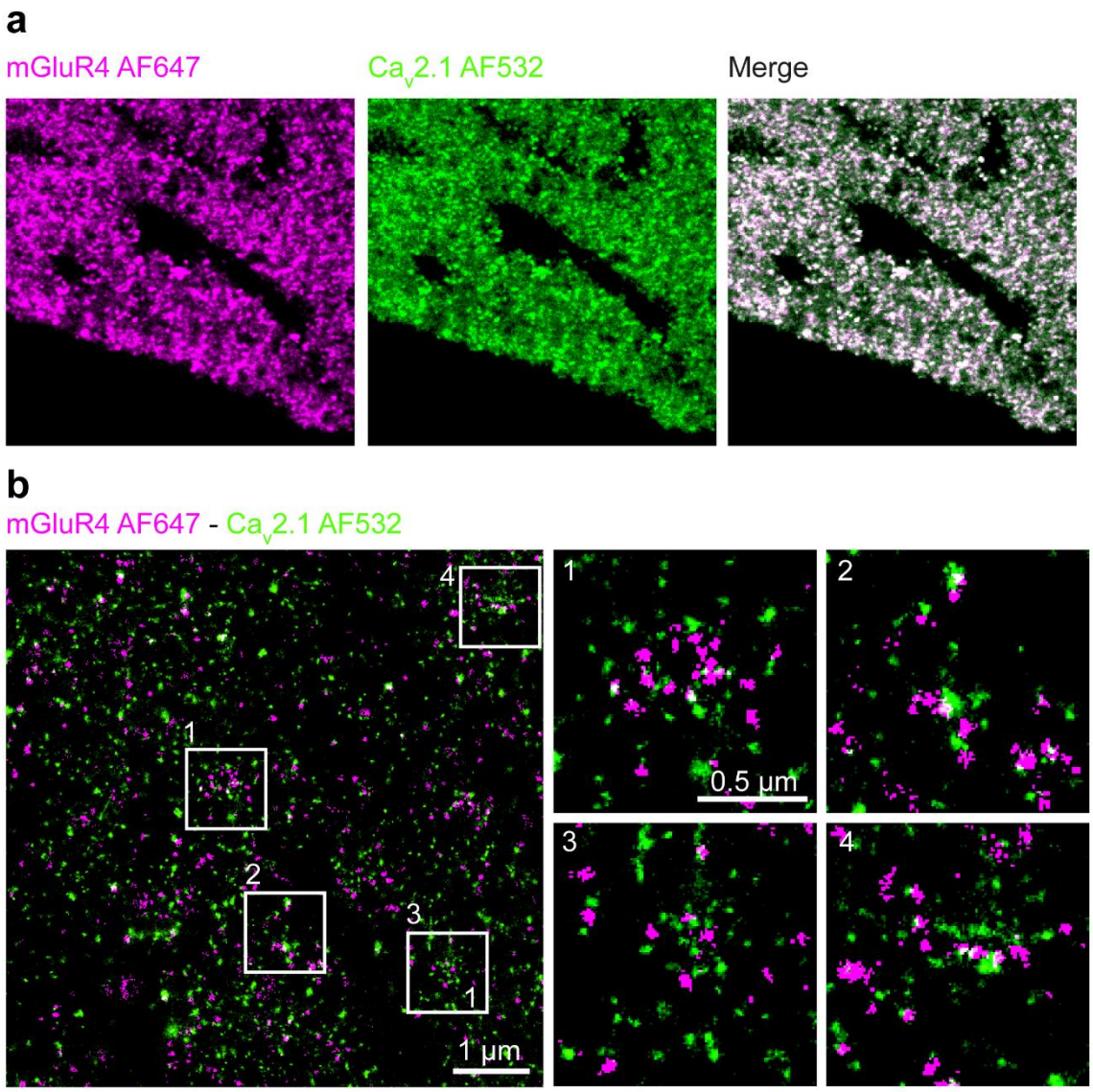
a
mGluR4 AF647
Ca$_V$2.1 AF532
Merge
b
mGluR4 AF647 - Ca$_V$2.1 AF532
1
2
3
4
1 µm
0.5 µm
c
Colocalization index
0.3
0.2
0.1
0.0
0
20
40
60
80
100
120
Distance (nm)
mGluR4 - Ca$_V$2.1
mGluR4 - Bassoon
Random localizations

Figure 21: Arrangement of mGluR4 relative to bassoon and $Ca_V2.1$ channels by distance-based colocalization analysis. (a) Representative confocal images of a slice stained for native mGluR4 (magenta) and $Ca_V2.1$ channels (green). The images were acquired in a region corresponding to the molecular layer of the cerebellum. **(b)** Representative two-color *d*STORM imaging of mGluR4 (magenta) and $Ca_V2.1$ channels (green). Left, shown is superresolved image revealing the organization of mGluR4 relative to $Ca_V2.1$. Right, 1-4 enlarged views of the boxed regions. **(c)** Distance based colocalization analysis. Shown is the quantification of colocalization index values over increasing distances. Colocalization index values (continuous line) were compared to values resulting from the correlation of randomly scrambled mGluR4 localizations across the image to bassoon or $Ca_V2.1$ localizations (dashed line). n = 7, 10 regions of 16 × 16 μm^2 from two independent preparations co-immunostained for (mGluR4 and bassoon) and (mGluR4 and $Ca_V2.1$ channels), respectively. Differences were statistically significant by two-way ANOVA followed by Bonferroni's post hoc test. ***P* < 0.01, ****P* < 0.001, and *****P* < 0.0001 versus random localizations. #*P* < 0.05, ##*P* < 0.01, and ###*P* < 0.001 for colocalization index values of (mGluR4 relative to $Ca_V2.1$ channels) versus colocalization index values of (mGluR4 relative to bassoon).

4.1.5 Substructural arrangement of mGluR4 relative to Munc 18-1

Next, due to the preferential location of mGluR4 at the AZ, this GPCR is likely to modulate synaptic transmission via directly affecting the exocytotic machinery. To tackle this theory, the spatial organization of mGluR4 was studied in relation to Munc 18-1 (which is a component of the vesicle fusion machinery) using the same approach described above. Cerebellar slices were co-immunostained for native mGluR4 and Munc 18-1. Confocal images revealed intense Munc 18-1 labeling in the molecular layer and the Purkinje cell layer, and weak labeling in the granular layer (**Fig. 22a**). Next, *d*STORM images revealed Munc 18-1 nanoclustering at the AZ indicated by mGluR4 clusters. Munc 18-1 was also located outside of the AZ along the presynaptic membrane, consistent with its role in multiple types of exocytosis (**Fig. 22b**)[111]. Remarkably, the distance-based colocalization analysis revealed an even closer and stronger association between mGluR4 and Munc18-1 than with either bassoon or $Ca_V2.1$ channels (**Fig. 22c**). The colocalization index values for mGluR4 relative to Munc 18-1 were (0.083 ± 0.026 and 0.123 ± 0.037) vs. (0.038 ± 0.005 and 0.057 ± 0.007) for mGluR4 relative to $Ca_V2.1$ at a distance of 20 and 40 nm, respectively.

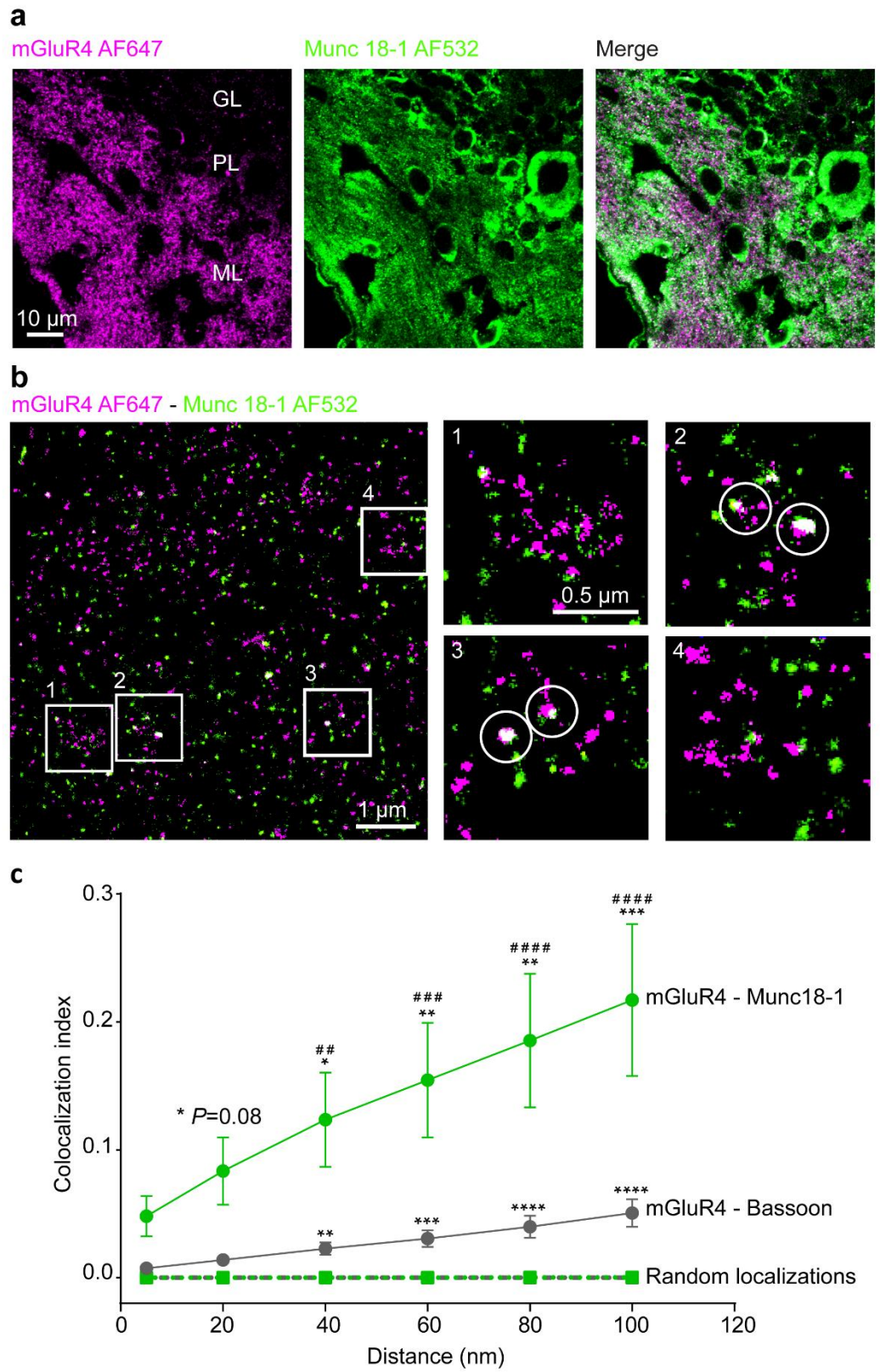
a
mGluR4 AF647
Munc 18-1 AF532
Merge
GL
PL
ML
10 µm
b
mGluR4 AF647 - Munc 18-1 AF532
1
2
3
4
1 µm
0.5 µm
c
Colocalization index
0.3
0.2
0.1
0.0
0
20
40
60
80
100
120
Distance (nm)
* P=0.08
mGluR4 - Munc18-1
mGluR4 - Bassoon
Random localizations

Figure 22: Arrangement of mGluR4 relative to bassoon and Munc 18-1 by distance-based colocalization analysis. (a) Representative confocal images of a coronal cerebellar slice stained for native mGluR4 (magenta) and Munc 18-1 (green). Images were acquired in a region corresponding to the cerebellar cortex of the cerebellum. **(b)** Representative two-color *d*STORM imaging of mGluR4 (magenta) and Munc 18-1 (green). Left, shown is superresolved image revealing the organization of mGluR4 relative to Munc 18-1. Right, 1-4 enlarged views of the boxed regions. **(c)** Distance based colocalization analysis. n = 7, 3 regions of 16 × 16 μm^2 from two independent preparations co-immunostained for (mGluR4 and bassoon) and one preparation co-immunostained for (mGluR4 and Munc 18-1), respectively. Differences were statistically significant by two-way ANOVA followed by Bonferroni's post hoc test. $^{**}P < 0.01$, $^{***}P < 0.001$, and $^{****}P < 0.0001$ versus random localizations. $^{\#\#}P < 0.01$, $^{\#\#\#}P < 0.001$, and $^{\#\#\#\#}P < 0.0001$ for colocalization index values of (mGluR4 relative to Munc 18-1) versus colocalization index values of (mGluR4 relative to bassoon) data points. ML: molecular layer, PL: Purkinje cell layer, and the GL: granule cell layer.

4.2 $GABA_BR$ dynamics in living hippocampal neurons

4.2.1 Single-molecule analysis of $GABA_BR$ dynamics in CHO cells and living hippocampal neurons by single-molecule TIRFM

In order to understand the lateral diffusion patterns of $GABA_BR$ at the cell surface of living hippocampal neurons in real-time with high spatial and temporal resolution I used single-molecule TIRFM. The SNAP-tag was fused to the extracellular N-terminus of the $GABA_{B1a}$ subunit (SNAP-$GABA_{B1a}R$) taking advantage of the fact that $GABA_BR$ is an obligatory heterodimer composed of $GABA_{B1}$ and $GABA_{B2}$ subunits. The SNAP-tag was fused to the $GABA_{B1a}R$ and not to the $GABA_{B2}R$ because $GABA_{B2}R$ can traffic to the plasma membrane alone, whereas $GABA_{B1a}R$ cannot reach the plasma membrane unless the functional heterodimer is formed. I will refer to $GABA_{B1a}R$ isoform as $GABA_{B1}R$. A previous report by our group showed that the SNAP-tagged receptor behaved like the wild-type receptor in the functional assays[47]. Hippocampal neurons were cotransfected with plasmids expressing SNAP-$GABA_{B1}$ and wild-type $GABA_{B2}$ subunits at 8 days in vitro (DIV). At 10-14 DIV, receptors were covalently labeled with a saturating concentration of AF549 (2 µM) and subsequently imaged by one-color TIRFM. The labeling stoichiometry was one fluorophore per heterodimer. Particles were automatically detected and tracked with algorithms based on *utrack* software implemented in Matlab[252]. $GABA_BRs$ were found to diffuse rapidly at the surface of hippocampal neurons and explore large areas of the axons and dendrites (**Fig. 23**). Interestingly, at least two dynamic patterns were observed. The trajectories of a fraction of the tracked receptors were apparently restricted within confined compartments (hot spots). On the other hand, a second fraction of the tracked receptors was found to explore a larger area of the plasma membrane. Receptors displaying the confined motion behavior at certain compartments (hot spots) are most probably anchored to synaptic compartments. To identify these compartments, I cotransfected the neurons with a presynaptic marker (bassoon) and a postsynaptic marker (homer) then analyzed the receptor trajectories by applying the mean square displacement (MSD) analysis as explained in the following section (4.2.2).

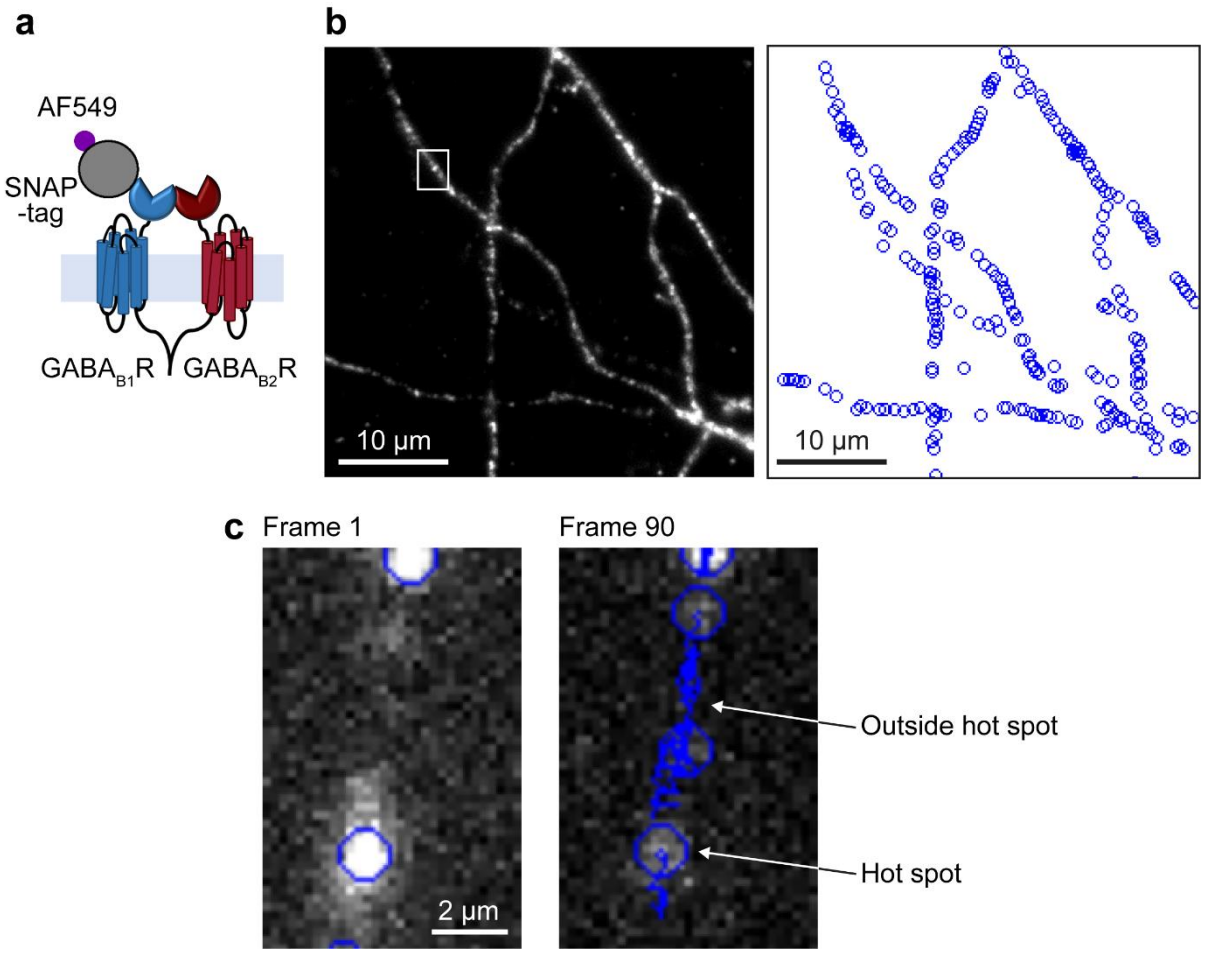

Figure 23: lateral diffusion of GABA$_B$Rs at the plasma membrane of living hippocampal neurons visualized by single-molecule TIRFM. (a) Schematic drawing of the heterodimer SNAP-GABA$_B$R construct. The SNAP-tag was inserted at the N-terminal domain of GABA$_{B1}$ subunit. **(b)** Left, representative TIRF image showing hippocampal neurons cotransfected with SNAP-GABA$_{B1}$ and GABA$_{B2}$ subunits and labeled with a saturating concentration of the cell-impermeable SNAP substrate (AF549) at 10-14 DIV. Dots represent individual receptor particles. Right, automated detection and tracking of GABA$_B$R particles. The blue circles indicate particle positions. **(c)** Magnification of the boxed region from b showing representative two frames and overlaid GABA$_B$Rs blue trajectories from the TIRF image stack. Shown are the first frame (left) and frame 90 (right) of 400 frames movie (30 ms temporal resolution). The blue circles and trajectories indicate particle positions and motion.

Next, I aimed to analyze $GABA_BR$ spatiotemporal dynamics and compare the difference in the behavior of receptors expressed in neurons and in simple cell model. Therefore, $GABA_BR$ was transfected in neurons (48 h transfection) and in CHO cells (4 hours transfection) to reach physiological expression levels. The MSD analysis was performed to calculate the diffusion coefficients of the detected $GABA_BR$ trajectories from both systems as explained in the method section. Receptors expressed in both CHO cells and neurons displayed four diffusion classes (immobile, sub-diffusion (confined motion), normal diffusion (Brownian motion), and super-diffusion (directed motion)). Interestingly, a significant smaller subpopulation of the receptors expressed in CHO cells showed the confined diffusion behavior (sub-diffusion) than the subpopulation belonging to the same class (sub-diffusion) but expressed in neurons. Additionally, a significant larger subpopulation of receptors expressed in CHO cells and displaying the Brownian motion behavior (normal diffusion) were detected in comparison to the subpopulation of receptors assigned to the same class (normal diffusion) but expressed in neurons (**Table 6 and Fig. 24**). These results suggest that, the observed slower and more confined $GABA_BR$ diffusion in neurons might be a result of receptor anchoring to scaffold or cytoskeleton proteins expressed exclusively in neurons.

Cell type	Super-diffusion	Normal diffusion	Sub-diffusion	Immobile
CHO cells	0.08 ± 0.01	0.44 ± 0.02(****)	0.28 ± 0.01(****)	0.23 ± 0.04
Hippocampal neurons	0.06 ± 0.01	0.22 ± 0.02	0.46 ± 0.03	0.28 ± 0.04

Table 7: Relative frequency distribution of the surface $GABA_B$ receptor trajectories expressed in CHO cells and hippocampal neurons based on the MSD analysis. Differences were statistically significant by two-way ANOVA. ****$P < 0.0001$ by Bonferroni's post hoc test.

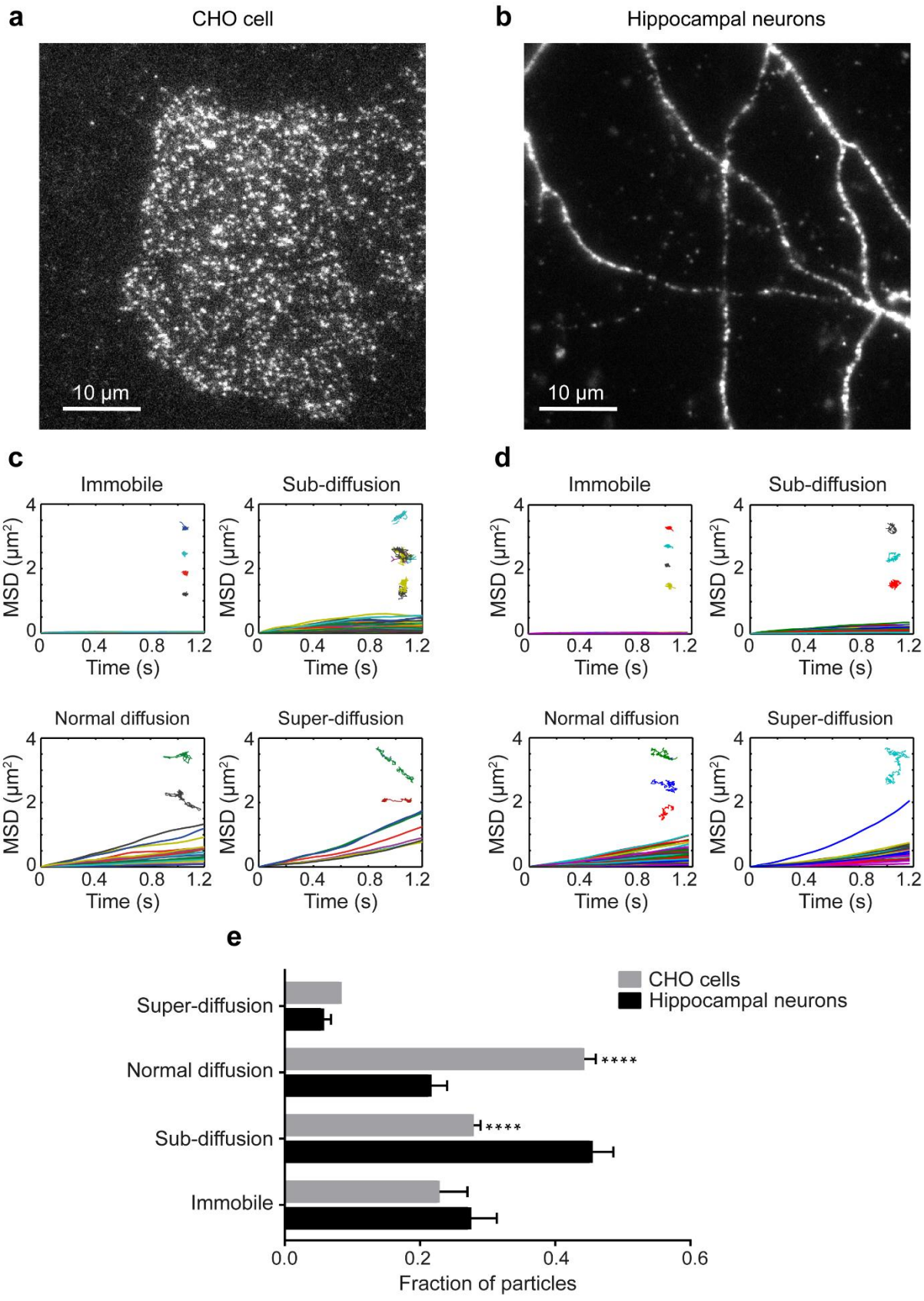
a
CHO cell
10 μm
b
Hippocampal neurons
10 μm
c
Immobile
Sub-diffusion
Normal diffusion
Super-diffusion
MSD (μm²)
Time (s)
d
Immobile
Sub-diffusion
Normal diffusion
Super-diffusion
MSD (μm²)
Time (s)
e
CHO cells
Hippocampal neurons
Super-diffusion
Normal diffusion
Sub-diffusion
Immobile
****
****
Fraction of particles

Figure 24: MSD analysis of surface $GABA_BR$ trajectories detected by single-molecule TIRFM in CHO and hippocampal neurons. Representative TIRF images of live **(a)** CHO cell and **(b)** hippocampal neurons expressing the SNAP-$GABA_B$Rs at physiological levels. $GABA_B$Rs are white dots. Representative MSD plots over time of $GABA_B$R trajectories in **(c)** CHO cells and **(d)** hippocampal neurons classified into four classes (immobile, sub-diffusion, normal diffusion and super-diffusion) based on the diffusion coefficients. **(e)** Relative frequency distributions of the four classes of $GABA_B$R trajectories expressed in CHO cells (gray) and neurons (black). Shown are representative images and results of 15 cells (5,165 particles) and 11 neurons (685 particles) from five and three independent experiments, respectively. Differences were statistically significant by two-way ANOVA. ****$P < 0.0001$ by Bonferroni's post hoc test.

4.2.2 $GABA_BR$ lateral dynamics in synaptic and extrasynaptic compartments in hippocampal neurons

Next, I aimed to analyze the lateral mobility of the pre- and postsynaptic $GABA_B$Rs depending on the receptor location inside or outside of the synaptic compartments using the MSD analysis. The MSD analysis reflects the area explored by $GABA_B$Rs. Presynaptic boutons were identified by either cotransfection of bassoon fused to the green fluorescent protein (bassoon-GFP) or labeling with the vesicle marker FM 4-64 dye. Neurons cotransfected with SNAP-$GABA_{B1}$R and bassoon-GFP were selected for further analysis. On the other hand, postsynaptic domains were identified by cotransfection homer-GFP. Most transfected neurons showed dual expression of both SNAP-$GABA_B$Rs and the synaptic markers. $GABA_B$Rs could be detected as early as 5 DIV after culturing. However, 14 DIV was selected for imaging because bassoon and homer were difficult to identify prior to 14 days of culturing. SNAP-$GABA_B$Rs were covalently labeled prior to imaging with a saturating concentration of AF549. At the presynaptic side of synapses (as marked by bassoon), $GABA_B$R fluorescent signals were observed along the axons and at the axon terminals (**Fig. 25a**). Postsynaptically (as marked by homer), $GABA_B$Rs were expressed at the dendritic spines and dendritic shafts. The majority of the receptor population was located at the extrasynaptic compartments (**Fig. 26a**). These findings are confirmed by a previous investigation performed using EM[177].

The mean square displacement (MSD) over time was measured to compare between the behavior of $GABA_B$Rs within and outside synaptic compartments. The trajectories of the pre- and postsynaptic $GABA_B$Rs displayed four diffusion classes (immobile, sub-diffusion, normal diffusion and super-diffusion). Regarding presynaptic $GABA_B$Rs, the receptors were observed to halt briefly on synapses. However, mobile and immobile receptors were detected at synaptic

compartments. Interestingly, only 0.09 ± 0.01 of the receptor subpopulation located at the synaptic compartments displayed super-diffusion (directional motion) behavior. In contrast, 0.61 ± 0.09 of the $GABA_BR$ subpopulation located at extrasynaptic compartments displayed super-diffusion behavior. Additionally, only 0.15 ± 0.07 of the receptor subpopulation located at the extrasynaptic sites and up to 0.35 ± 0.10 of the receptors located at the synaptic compartments were immobile (**table 7 and Fig. 25b**). These results suggest the existence of regulatory mechanisms in synaptic compartments that leads to $GABA_BR$ retention. Immobile receptors are defined as receptors with diffusion coefficient $D \leq 0.01\ \mu m^2 s^{-1}$ and particles belonging to the super-diffusion behavior are those characterized by $D \geq 0.01\ \mu m^2 s^{-1}$ and $\alpha > 1.25$. Concerning postsynaptic $GABA_BRs$, strikingly, 0.40 ± 0.11 of $GABA_BR$ subpopulation located at the synaptic compartments were immobile and stationary. In contrast, only 0.11 ± 0.07 of the subpopulation at extrasynaptic compartments within the dendritic shaft were immobile (**table 7 and Fig. 26b**). These results suggest that $GABA_BRs$ interact with certain factors at the synaptic compartments that result in interference with $GABA_BR$ dynamics.

There are known differences between the pre- and postsynaptic $GABA_BRs$ in terms of the complex composition and pharmacological mechanisms[253, 254]. Therefore, I also compared between presynaptic and postsynaptic receptors in terms of the diffusion patterns. According to the current results**,** pre- and postsynaptic $GABA_BRs$ behave similarly (**table 7, Fig. 25, and fig. 26**). The diffusion characteristics of receptors located at synaptic and extrasynaptic compartments were comparable in terms of receptor fractions belonging to the four diffusion classes.

Receptor location	Super-diffusion	Normal diffusion	Sub-diffusion	Immobile
Presynaptic; synaptic compartments	0.09 ± 0.01(*)	0.26 ± 0.05	0.40 ± 0.05	0.35 ± 0.10
Presynaptic; extrasynaptic compartments	0.61 ± 0.09	0.15 ± 0.03	0.34 ± 0.11	0.15 ± 0.07
Postsynaptic; synaptic compartments	0.05 ± 0.01	0.21 ± 0.02	0.45 ± 0.09	0.40 ± 0.11(*)
Postsynaptic; extrasynaptic compartments	0.13 ± 0.01	0.34 ± 0.08	0.57 ± 0.10	0.11 ± 0.07

Table 8: Relative frequency distribution of the pre- and postsynaptic $GABA_BR$ trajectories based on MSD analysis. Differences were statistically significant by two-way ANOVA. *$P < 0.05$ by Bonferroni's post hoc test.

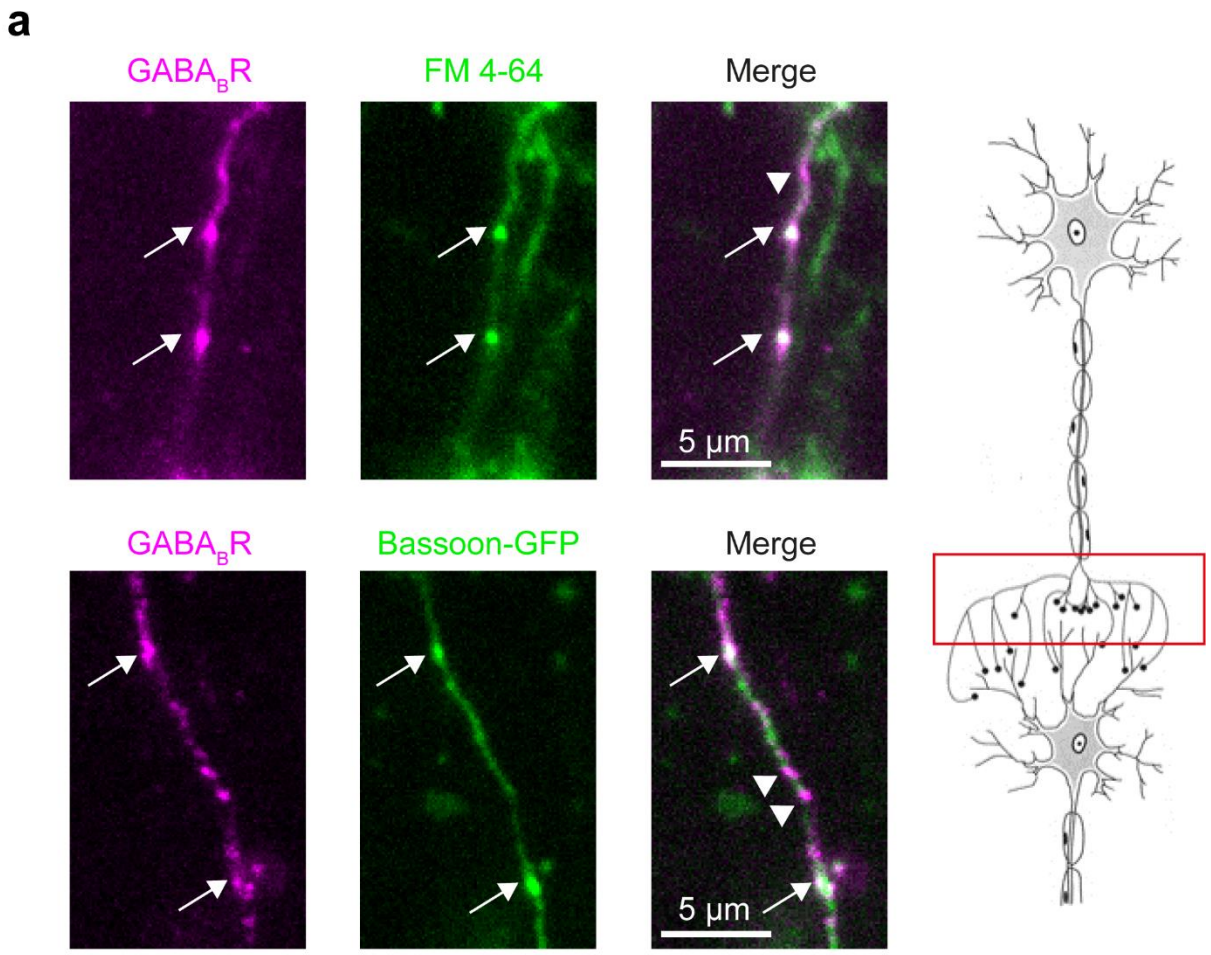
a
GABA$_B$R
FM 4-64
Merge
5 µm
GABA$_B$R
Bassoon-GFP
Merge
5 µm
b
Synaptic
Extrasynaptic
Super-diffusion
*
Normal diffusion
Sub-diffusion
Immobile
0.0
0.2
0.4
0.6
0.8
Fraction of particles

Figure 25: Distribution and multiple lateral diffusion patterns of presynaptic $GABA_BRs$ located at the synaptic and extrasynaptic compartments in living hippocampal neurons. (a) Representative TIRF images showing hippocampal neurons expressing the SNAP-$GABA_BR$ (magenta). Presynaptic boutons in green were marked by either FM 4-64 (upper panel) or bassoon-GFP (lower panel). Arrows indicate $GABA_BRs$ confined within the synaptic compartments. Arrow heads indicate $GABA_BRs$ diffusing at extrasynaptic compartments. **(b)** Relative frequency distributions of the four classes of presynaptic $GABA_BR$ trajectories at synaptic (green) and extrasynaptic (magenta) compartments. Shown are representative images and results of 7 neurons (122 and 659 analyzed particles in synaptic and extrasynaptic compartments, respectively) from two independent experiments. Differences were statistically significant by two-way ANOVA. $*P < 0.05$ by Bonferroni's post hoc test.

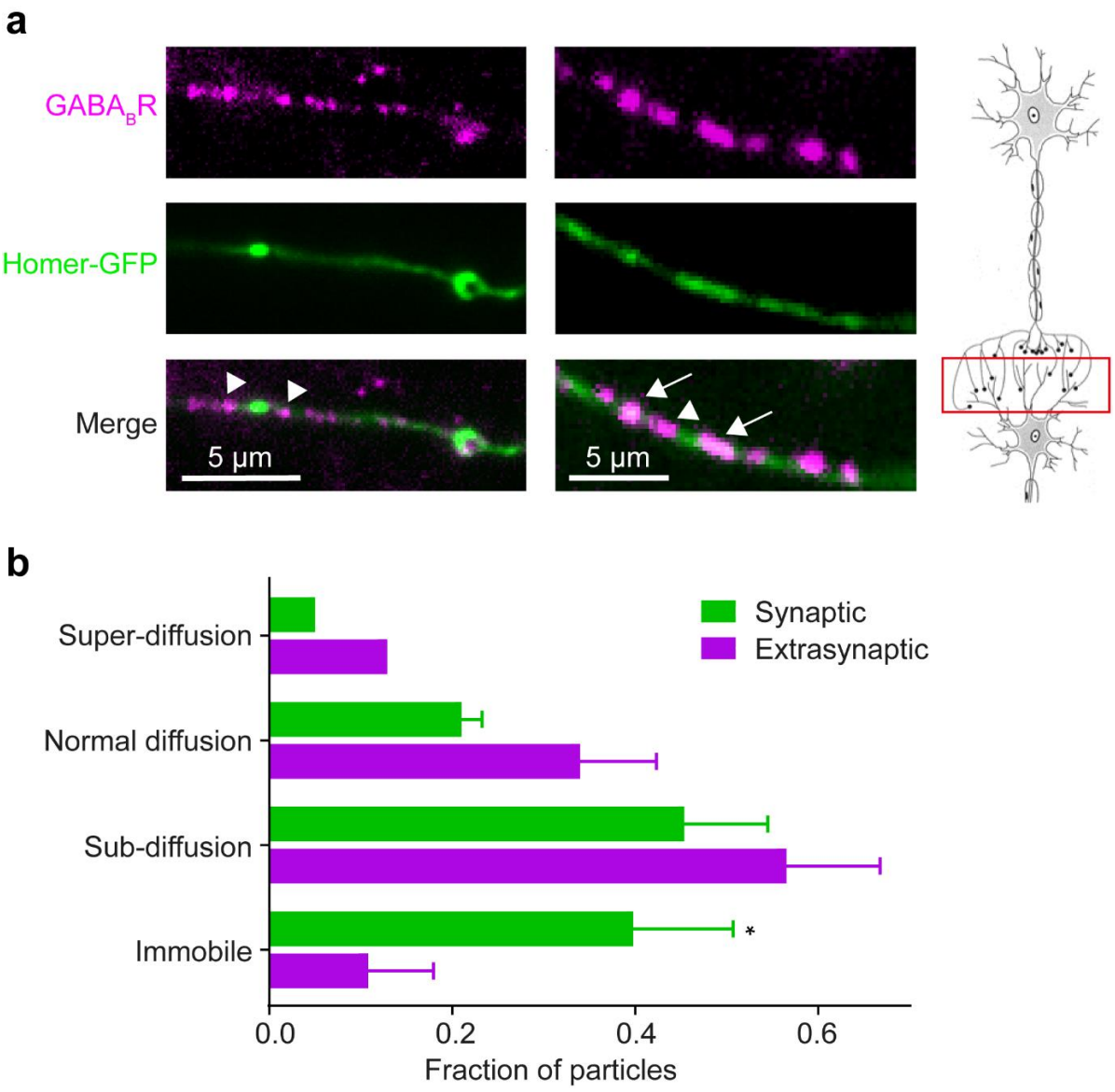

Figure 26: Distribution and multiple lateral diffusion patterns of postsynaptic GABA$_B$Rs located at the synaptic and extrasynaptic compartments in living hippocampal neurons. (a) Representative TIRF images showing hippocampal neurons expressing the SNAP-GABA$_B$R (magenta). Postsynaptic dendritic spines were marked by homer-GFP (green). Arrows indicate GABA$_B$Rs confined within the synaptic compartments. Arrow heads indicate GABA$_B$Rs diffusing at extrasynaptic compartments. **(b)** Relative frequency distributions of the four classes of postsynaptic GABA$_B$R trajectories at synaptic (green) and extrasynaptic (magenta) compartments. Shown are representative images and results of 6 neurons (58 and 98 analyzed particles in synaptic and extrasynaptic compartments, respectively) from two independent experiments. Differences were statistically significant by two-way ANOVA. *P < 0.05 by Bonferroni's post hoc test.

4.2.3 Colocalization of $GABA_BR$ and actin cytoskeleton in hippocampal neurons

Several mechanisms were proposed to regulate the spatial organization of GPCRs at the plasma membrane. The cortical actin cytoskeleton was suggested to interact with GPCRs to regulate their expression and distribution at the cell surface. To investigate whether the actin cytoskeleton plays a role in anchoring diffusing $GABA_BRs$, I assessed the colocalization between endogenous $GABA_BRs$ and the actin filaments (F-actin). Hippocampal neurons were stained for $GABA_{B1}R$ and F-actin by indirect IF then fixed. $GABA_BRs$ were detected with a specific antibody raised against the 873-977 amino acid residue at the intracellular C-terminal of the $GABA_{B1}R$. F-actin was detected with the fluorescence Alexa Fluor 532 Phalloidin. $GABA_BRs$ were expressed in the neurons in punctate pattern. Moreover, confocal images showed apparent $GABA_BRs$ expression along the F-actin (**Fig 27**). This result suggests that, $GABA_BRs$ might interact directly or indirectly with the actin cytoskeleton. Confocal images unfortunately did not provide enough resolution to reveal the molecular organization of $GABA_BRs$ with F-actin. The application of *d*STORM to study $GABA_BR$ molecular organization in detail would be necessary in the future to draw firm conclusions.

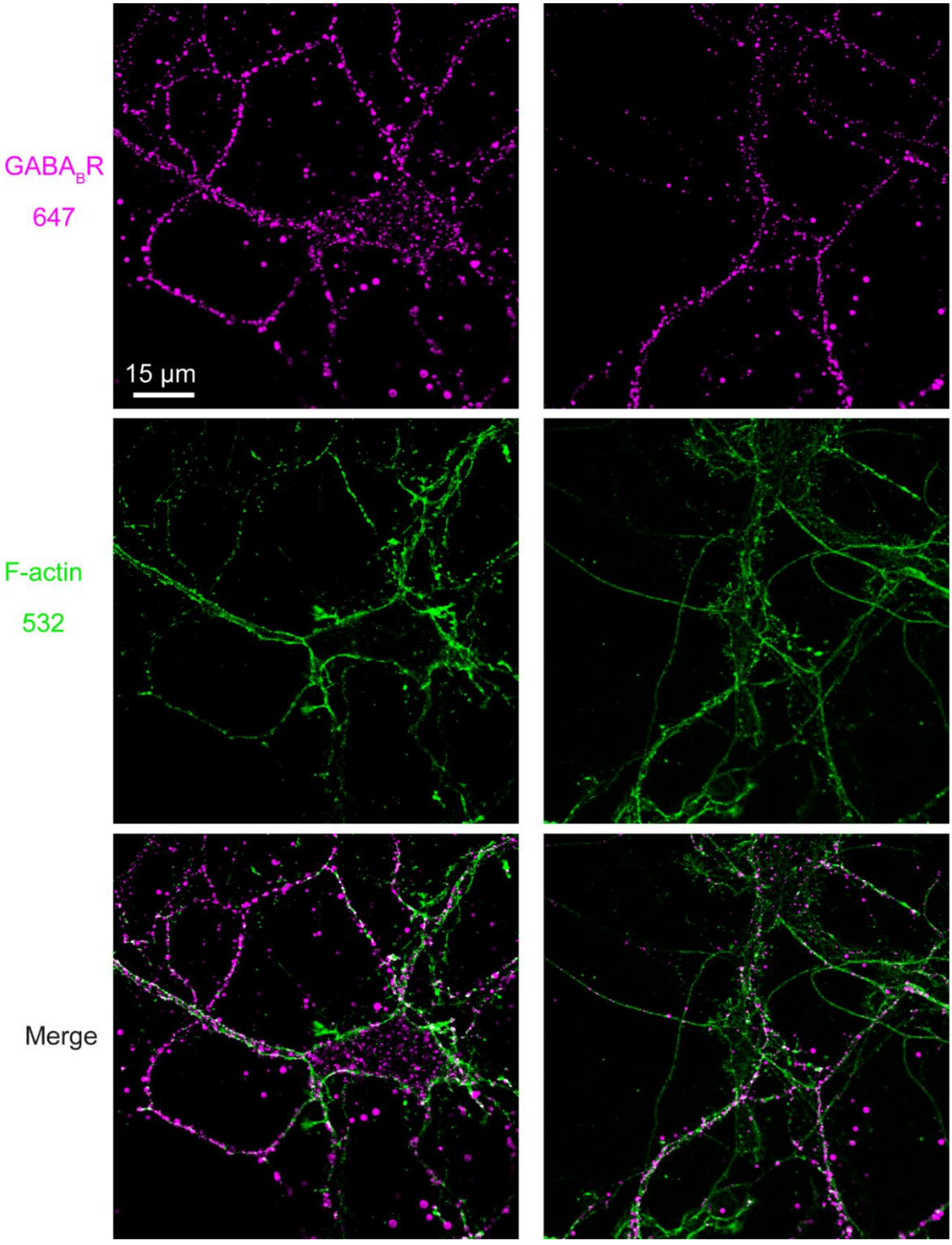

Figure 27: Confocal images of expression and synaptic localization of endogenous GABA$_B$R and F-actin in fixed hippocampal neurons. Representative confocal images of PFA-fixed hippocampal neurons at 14 DIV stained simultaneously for endogenous GABA$_B$R (magenta) and F-actin (green).

5 Discussion

5.1 Nanoscopic organization of mGluR4 at presynaptic active zones

This study provides a detailed characterization of the nanoscopic organization of mGluR4 at the AZs of model parallel fiber synapses in the cerebellum. mGluR4 nanodomains were visualized with nanoscale precision using two-color *d*STORM. Results obtained from *d*STORM were combined with data from single-molecule TIRFM, to achieve quantitative analysis.

The data obtained by *d*STORM under high labeling and controlled conditions provide strong evidence for the organization of mGluR4 in small nanodomains each containing 1-2 mGluR4s, with few containing three or more receptors. This result is in line with a previous report that revealed clustering of mGluR4 at parallel fiber terminals using immunogold EM[255]. However, specific labeling with antibody-conjugated gold particles is generally inefficient and there is a trade-off between the achievable tissue preservation and spatial resolution[256]. Thus, *d*STORM has more advantages where it combines the efficient labeling and good structural preservation of immunofluorescence microscopy with the high spatial resolution of EM. My *d*STORM analysis has also revealed that mGluR4 is enriched four-fold at the parallel fiber AZs compared to perisynaptic sites and sites further away from the synapse. In a previous report, β-adrenergic receptors were found to be organized in the form of signalosomes within cardiac myocytes[257]. Additionally, the composition and number of these signalosome complexes were found to determine the rate of myocyte contraction[257]. Similarly, the revealed organization of mGluR4 nanodomains at the AZs of PFs is consistent with the receptor's function in modulating short-term plasticity, and for mediating the neuronal survival and normal motor performance[258, 259, 260]. Such distribution may provide a mechanism for the rapid receptor activation by glutamate and hence the rapid regulation of synaptic transmission by circumventing the burden of receptor diffusion. When multiple receptors are arranged in the form of a nanodomain, the receptor action is neither slowed down by the diffusion nor dependent on bulk concentrations within a certain cell volume.

Various methods were applied to study GPCR oligomerization. Biochemical methods such as immunoblots and co-immunoprecipitation assays were widely used. However, these methods require stable protein-protein interactions to analyze the interactions of molecules. FRET/BRET studies have been instrumental in demonstrating GPCR oligomeric states due to their high resolution. However, these ensemble biophysical techniques report the average

behavior of millions of molecules. Additionally, these methods cannot distinguish if the signal arises from the cell surface or from the cell interior. Single-molecule microscopy has additional advantages for the investigation of GPCR oligomerization. The investigated receptors expressed in physiological concentrations are examined in living cells under controlled conditions. Thus, I exploited single-molecule TIRFM to characterize the oligomeric states of mGluR4. This method is reliable, accurate, and precise for the stoichiometry measurements of receptor complexes as detected by the two controls (SNAP-CD86 and SNAP2×-CD86). These positive controls were detected correctly as monomers and dimers, respectively. Analyses of the intensity distribution of mGluR4 fluorescent spots revealed that the majority of mGluR4 is expressed in the form of homodimers. A fraction of receptors (29%) was organized in the form of trimers. This finding is in agreement with a previous *in vitro* finding showing that a truncated mGluR4 containing part of the extracellular N-terminal domain (i.e. the first 548 amino acids) migrates as a dimer and trimer using gel electrophoresis[261]. Additional studies performed on other mGluR subtypes have also reported mGluR homodimerization[50, 51, 65]. However, results from single-molecule analysis are more reliable and rigorous.

Quantitative superresolution imaging by *d*STORM was introduced recently for the quantification of endogenous AZ elements following standard IF labelling[217]. Here, the same approach was used to quantify a prototypical GPCR in the AZs for the first time. Each parallel fiber terminal has on average 1.05 - 1.12 AZs[92, 262, 263]. We detected a large variability in the number of mGluR4 nanodomains per AZ (on average each AZ contains 29 mGluR4 nanodomains). The AZ area showed a broad distribution, ranging from 10.02×10^4 to 58.14×10^4 nm^2 (mean = $21.63 \pm 0.38\times10^4$ nm^2). Thus, the large variation in the number of mGluR4 nanodomains per AZ might be partially attributed to the high variability of the AZ size. I found that some of the mGluR4 nanodomains contain one receptor per nanocluster despite the widely accepted class C homo-/heterodimerization. This finding might be explained by the presence of a fraction of monomers. A second more likely explanation is that mGluR4 formed a heterodimeric complex with other mGluR subtypes that were not labeled. Previous observations by trFRET suggest that mGluR4 can form a heterodimeric complex with mGluR2, however, mGluR2 is located mainly at perisynaptic sites[55, 125]. mGluR7 is expressed at the AZs of pyramidal neurons in the hippocampus[29, 264, 265]. In the cerebellum, mGluR7 is expressed in PCs but not in granule cells[193]. However, mGluR7 mRNA is expressed in the granule cells of developing rats (P14 and P21)[266]. Additionally, mGluR7 mRNA and protein were detected in cultured cerebellar granule cells[267]. Thus, mGluR7 might be expressed at a very low density and/or at certain developmental stages in the PF-PC synapses of rodents. Studies investigating mGluR8 subcellular localization are very few. Therefore, mGluR4 might form heterodimeric complexes with mGluR7 and/or mGluR8. This theory could be tested by

staining cerebellar slices simultaneously for endogenous mGluR4 and mGluR7/8 to assess the stoichiometry of the receptor complex.

The high-resolution capabilities of *d*STORM combined with a distance-based colocalization analysis allowed me to assess mGluR4 proximity to its effectors at a nanoscale resolution. One major finding of my study was the close proximity of mGluR4 to $Ca_V2.1$ channels at distances that we would expect for physically interacting proteins labeled with pairs of primary and secondary antibodies. However, the exact stoichiometries of these elements could not be identified. No direct association between mGluR4 and VDCC has been reported so far; however, a previous study has revealed that the postsynaptic mGluR1 interacts directly with $Ca_V2.1$ via the C-terminal of the receptor and channel[135]. These data are consistent with the presence of mGluR4s and $Ca_V2.1$ channels in either small, functional nanodomains or macromolecular signaling complexes. Such unique organization may allow specific calcium signaling and/or facilitate rapid regulation of channel activity. Pre-formed complexes allows more efficient signaling compared to proteins that are dissociated from each other and function via random collisions.

The most striking finding of this study is the close proximity between mGluR4 and Munc 18-1 detected by *d*STORM. This finding is consistent with a previous proteomic study performed on cerebellar slices reporting that native mGluR4 forms complexes with Munc 18-1[140]. This result suggests that the mGluR4 depressive effect on glutamate release is not solely mediated by depressing VDCC, but also by regulating Munc 18-1. mGluR4 may interact with Munc 18-1 to prevent Munc 18-1 interaction with syntaxin-1. The prevention of Munc 18-1 interaction with syntaxin-1 hinders vesicle fusion and depresses glutamate release[268]. Therefore, mGluR4 might have a G protein-independent effect by directly sequestering SV exocytosis machinery. The organization of mGluR4 into nanodomains with bassoon, $Ca_V2.1$, and/or with Munc 18-1 reflects heterogeneity of the nanodomains composition and potential mGluR4 diverse functions.

5.2 $GABA_BR$ dynamics in living hippocampal neurons

Due to the knowledge gap in understanding how polarized neurons regulate GPCR dynamics, I studied $GABA_BR$ spatiotemporal diffusion as a model GPCR at the plasma membrane of neurons utilizing single-molecule TIRFM. The lateral diffusion patterns at the synaptic and extrasynaptic compartments were characterized by MSD analysis. MSD analysis in neurons represents a powerful approach to reveal confinement of receptor within certain compartments.

GPCR diffusion has mainly been investigated in heterologous systems such as CHO cells due to their smooth and flat surface. Results obtained from these studies are insufficient in drawing conclusions regarding the patterns of GPCR diffusion. Neurons have narrow processes and do not lay flat on a coverslip but rather form multilayers culture. Therefore, attempts using single-molecule microscopy to study GPCRs in neurons are more challenging. Here, single-molecule TIRFM was used to analyze SNAP-tagged $GABA_BR$ diffusion in CHO cells and hippocampal neurons. Some previous studies used antibodies to recognize extracellular epitopes of inotropic receptors. However, fusion of a SNAP-tag to the receptor in question would be more dynamic and flexible.

This study revealed that $GABA_BRs$ laterally diffuse in hippocampal neuronal networks. A significantly large population of presynaptic $GABA_BRs$ located at extrasynaptic compartments display a directional motion (super-diffusion) behavior compared to receptors located at synaptic compartment. Additionally, majority of the pre- and postsynaptic receptors located at synaptic compartments were found to be stationary or confined within limited regions, suggesting the existence of regulatory mechanisms within synaptic compartments. The stationary/confined motion of the $GABA_BRs$ at the synaptic sites might improve the efficiency of the inhibition of the neurotransmitter release and postsynaptically inhibitory signals given the low number of receptors expressed per synapse and the low $GABA_BR$ affinity for GABA.

One possible theory to explain the restricted motion of $GABA_BR$ at synaptic compartments is the physical trapping of receptors due to the morphology of the thin spin neck. The second possibility is that the diffusion of the receptor is determined by the size and nature of $GABA_BR$ arranged in different protein complexes. Based on a recent proteomic analysis, native receptors were reported to arrange with diverse nano-architecture [269]. This study suggested that $GABA_BR$ complexes are formed of core and periphery layers. The core layer is always fixed and is composed of $GABA_{B1}R$, $GABA_{B2}R$, heterotrimeric G protein, and KCTD tetramers. The peripheral layer includes diverse elements, such as effector channels (VDCC, GIRK), leading to receptor molecular diversity. The third and most probable possibility is that the receptors are less motile at synaptic compartments due to the different matrix organization that stabilizes the receptors. For example, anchoring of the receptors through interactions with synaptic scaffolding or cytoskeleton proteins may restrict receptor motility. Experiments done in our group by colleagues (Dr. Marie-Lise Jobin and Dr. Titiwat Sungkaworn) on a similar project showed that, the first intracellular loop of $GABA_{B1}R$ is responsible for the organization of $GABA_BRs$ in the form of ordered arrays in CHO cells. Furthermore, after screening for potential proteins that bridge the interaction between $GABA_BR$ and actin, filamin A was identified as a strong candidate. The analysis of the role of filamin A in bridging $GABA_BR$

interaction to the cytoskeleton is important in the future. In a previous investigation using FRAP, the authors suggested that a region between residues 862 and 886 in the C-terminal domain of the $GABA_{B2}$ subunit is important for the regulation of the $GABA_{B2}R$ restricted mobility[270]. However, the authors did not address whether the C-terminal of $GABA_{B2}R$ is also important for the regulation of the movement of functional $GABA_BRs$ taking into account that the $GABA_{B2}$ subunit is functionally silent is absence of $GABA_{B1}$ subunit[40, 42].

As quantified by the MSD analysis, some of the receptors located in extrasynaptic compartments showed a confined motion behavior. This observation could be explained either by unstaining of the synapses or that the receptors might be part of a higher order oligomeric state (dimers or tetramers of heterodimers)[47]. An additional theory is that the receptors are undergoing their natural default clathrin-mediated endocytosis. This theory could be tested in the future by labeling the clathrin-coated pits and monitoring $GABA_BR$ diffusion.

Finally, I investigated whether F-actin plays a role in the regulation of $GABA_BR$ mobility and organization at the plasma membrane of neurons. Confocal images showed that $GABA_BRs$ are organized along F-actin filaments. However, confocal images did not provide enough resolution and hence an in-depth characterization was not possible. Therefore, *d*STORM experiments must be performed in the future to conclude whether F-actin plays a role in the regulation of $GABA_BR$ mobility. A previous study done in our group using CHO cells visualized by single-molecule TIRFM demonstrated that $GABA_BRs$ have limited mobility and are arranged in rows via interactions with actin fibers[47]. Additionally, SNAP-tagged somatostatin receptor subtype 2 (SSTR2) expressed in CHO cells localize preferentially along actin fibers[225]. Contrary to multiple previous reports confirming that GPCR spatial organization is regulated by the actin cytoskeleton, a single report suggested that actin and tubulin do not play a direct role in regulating $GABA_{B2}R$ mobility at the surface of the plasma membrane[270]. The authors showed that treatment of the cells with latrunculin and colchicine to disrupt the cytoskeleton and β-tubulin, respectively, do not affect $GABA_{B2}R$ mobility. The authors however did not investigate the effect of cytoskeleton and tubulin destruction on the function $GABA_B$ heterodimer.

$GABA_BRs$ tightly regulate some forms of long-term potentiation and long-term depression mediated by NMDARs[152]. Therefore, the observed diffusion patterns revealed and characterized by this study might play a role in the regulation of synaptic strength and hence plasticity.

6 Conclusions

6.1 *d*STROM reveals nanoscale organization of metabotropic glutamate receptors at presynaptic active zones

GPCR nanodomain organization, composition, and stoichiometry are suggested to regulate the function of receptors. Presynaptic metabotropic glutamate receptors subtype 4 (mGluR4) plays key roles in the regulation of glutamate release. However, the molecular mechanisms of mGluR4 actions are not fully identified. Here, I investigated the subcellular distribution of endogenous mGluR4 in the highly organized presynaptic active zone of the parallel fiber in the mouse cerebellum. Two-color *direct* stochastic optical reconstruction microscopy (*d*STORM) was used to examine mGluR4 nanoscopic distribution using a specific primary α-mGluR4 and Alexa Fluor-conjugated secondary antibody with a spatial resolution of ~ 13 nm. *d*STORM images revealed a four-fold mGluR4 enrichment at active zones. Single-molecule microscopy showed that mGluR4 is mainly expressed in the form of homodimers at physiological expression levels. The obtained data indicated that mGluR4 are organized in nanodomains of one or two receptors on average. Additionally, distance-based colocalization analysis revealed that mGluR4 is expressed in close proximity to its main effectors ($Ca_V2.1$ and Munc 18-1). Altogether, this unique spatial organization can play an important role for the efficiency and rapid signaling required for synaptic transmission. It would be of great interest to correlate mGluR4 nanoscopic distribution with its function in the future to understand how GPCRs fine-tune fundamental physiological functions.

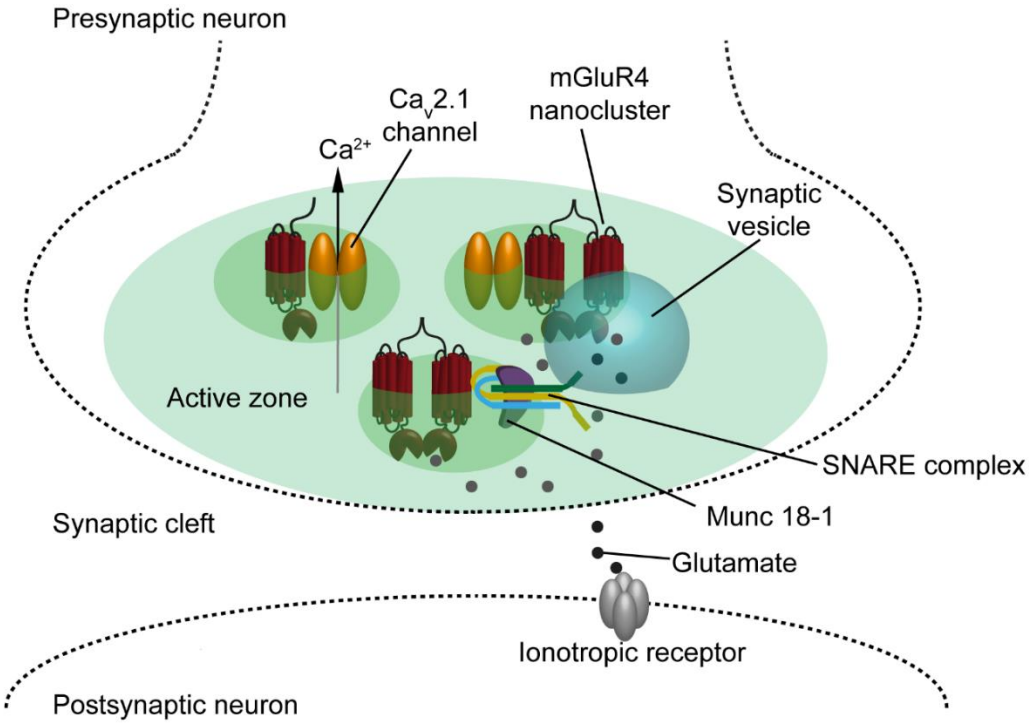

Figure 28: Schematic summary depicting endogenous mGluR4 nanoscale organization within the active zones. mGluR4 is located in close proximity to $Ca_V2.1$ channels and Munc 18-1 at the presynaptic AZs. This unique spatial organization provides a basis for understanding mGluR4 underlying mechanisms in the modulation of synaptic transmission.

6.2 Single-molecule TIRFM reveals characteristic dynamic patterns of GPCR depending on receptor location in neurons

The dynamics of γ-aminobutyric acid subtype B receptors ($GABA_BRs$) in living neurons at the level of individual proteins, and the molecular mechanisms regulating their surface expression are currently poorly understood. In the present study, single-molecule total internal reflection fluorescence microscopy combined with SNAP-tag technology was performed to characterize $GABA_BR$ diffusion dynamics in hippocampal neurons with a high spatial (10-20 nm) and temporal (20 ms) resolution. The MSD analysis revealed that the majority of $GABA_BRs$ located at extrasynaptic sites move rapidly and freely. Approximately 80% of the synaptic receptors are immobile or display restricted diffusion behavior within confined regions. The limited diffusion of the pre- and postsynaptic $GABA_BRs$ at synaptic compartments are hypothesized to play a contributing role in synaptic transmission efficacy.

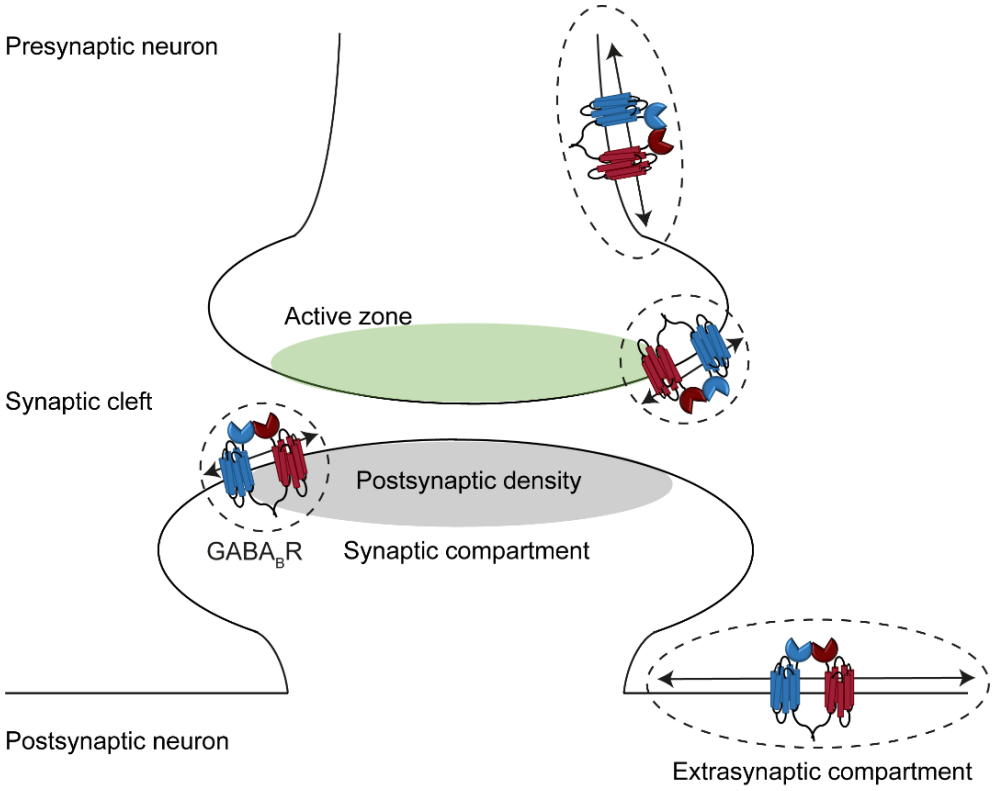

Figure 29: Schematic summary depicting the diffusion patterns of $GABA_BR$ in synaptic and extrasynaptic compartments. $GABA_BRs$ diffuse slowly within confined regions in synaptic compartments. Receptors located in extrasynaptic compartments diffuse faster than the synaptic receptors and explore larger regions.

7 Outlook

My approach utilizing *d*STORM to quantify mGluR4 nanoclusters has an advantage of assessing native receptors using conventional primary and secondary antibodies. In this way, we avoid bizarre protein folding or atypical post-translational modifications introduced by the protein engineering and subsequent transfection. However, direct assessment of mGluR4 stoichiometry could be achieved by labeling the receptor with SNAP/CLIP-tagging system (where we have a 1:1 stoichiometry). To achieve this, I am participating in a current project running in the laboratory in order to establish SNAP-mGluR4 knockin mice, using CRISPR/Cas9 technology. Cerebellar slices from these mice could be used in a fallow-up study to determine the absolute stoichiometry of mGluR4 at the AZ. This would preclude possibility of errors due to undercounting caused by incomplete antibody binding or due to displacement of the fluorophore-conjugated antibodies far from the receptors.

This study focused on studying mGluR4 proximity to $Ca_V2.1$ because it is the main VDCC type regulating the neurotransmitter release from central nerve terminals. Thus, more open questions remain regarding the proximity of mGluR4 to other VDCC isoforms expressed at the active zone contributing to the Ca^{2+} influx such as $Ca_V2.2$ as it shares high sequence identity with $Ca_V2.1$. It would be also interesting to investigate the spatial relationship aspects of mGluR4 to other SNARE complex components such as SNAP-25, Syntaxin-1, and Synaptotagmine which were found to co-immunoprecipitate with anti-mGluR4 antibodies in a study conducted on cerebellar extracts[140]. In order to answer the question of whether mGluR4 close proximity to $Ca_V2.1$ and Munc 18-1 revealed by this study is due to direct protein-protein interaction or indirect interaction, it would be of interest to conduct a pull-down assay using purified proteins. It is also tempting to FRET/BRET studies to resolve the proximity of the proteins in living cells at a distance of 10 nm. However, with FRET/BRET strategy, we cannot distinguish between direct and indirect interactions[271, 272].

Finally, conducting experiments to investigate the physiological implication of mGluR4 nanocluster organization and the importance of packing density on synaptic transmission by optogenetics is also crucial to reveal functional consequences and to proof that local signals are provoking confined physiological functions.

In my thesis I characterized $GABA_BR$ dynamics in living neurons during basal state in details. As a following step, it would be interesting to stimulate the receptors with GABA/baclofen; $GABA_BR$ agonists, to analyze how the diffusion rate of synaptic and extrasynaptic $GABA_BRs$ would be affected. The number of glutamate and GABA receptors available for binding with their corresponding neurotransmitters in neurons were found to be regulated not only by endocytosis and exocytosis but also by the receptor rapid lateral movements at the plasma membrane. The lateral AMPA and NMDA receptors movements inside and outside synapses may be associated with long term potentiation and long term depression which are important for learning and forming memories[152, 158, 273, 274]. Therefore, it would be interesting to analyze the movies to investigate the reality of $GABA_BR$ lateral diffusion inside and outside synapses to regulate the receptor numbers at synaptic compartments. This diffusion behavior might play a role in the regulation of synaptic strength.

In hippocampal neurons around 80% of $GABA_BRs$ were anchored within synapses and, I observed clustered $GABA_BR$ organization within synaptic sites. Therefore, a next step would be to analysis the intensity distribution of the $GABA_BR$ fluorescent signals to reveal the oligomeric state of receptors within synaptic compartments. It would be also interesting to analyze the stoichiometry of receptors at extrasynaptic sites and finally compare between the two populations to evaluate if there is any consequence on signaling. Same sets of experiments regarding $GABA_BR$ dynamic patterns could be applied at organotypic cultures or acute brain slices to analyses the receptor motion at 3 D context that resembles the *in vivo* brain architecture. Nonetheless, it is expected that the same dynamic signature would be found based previous studies done on dopamine receptors[173, 275]. D1 receptor was labeled with quantum dots. The receptors were found to diffuse along the neurons of cultured hippocampal cells in a pattern consistent with that observed at the acute brain slices[173, 275].

Confocal images showed potential colocalization between $GABA_BR$ and F-actin, suggesting potential actin cytoskeleton role in the regulation of the $GABA_BR$ organization at the plasma membrane. Confocal images unfortunately did not provide enough resolution to reveal molecular organization of $GABA_BRs$ with F-actin. The rational following step, is to utilize *d*STORM to validate this hypothesis. It would be also important to study if the actin cytoskeleton globally regulates the number of receptors expressed at the cell surface or finely regulates the receptor stoichiometry and stability. Furthermore, it would be important to study which proteins link $GABA_BRs$ to regulate its spatial distribution and subsequently the synaptic function. Analysis of the role of filamin A scaffold proteins in bridging $GABA_BR$ to the cytoskeleton is important. One possible approach is to cotransfect a mutated $GABA_BR$ that doesn't bind to filamin A (already present in the laboratory) in neurons, then to analyze the

diffusion coefficient and the MSD changes in comparision to the wild-type receptors. Aa alternative approach is to inhibit filamin A expression by siRNA then visualize the $GABA_BR$ mobility by single-molecule TIRF.

8 Annex

9.1 Primer sequences

Primer name	Primer Sequence
Sub-cloning SpeI-SYN fw	AAAAAAACTAGTGCCCTGCGTATGAGTGCAAG
Sub-cloning SYN-EagI rev	AAAAAACGGCCGGACACGACTCCTCCGCTGC

Table 9: Description and sequences of primers used for subcloning in this study.

9.2 Sub-cloning of synapsin promoter-driven $GABA_BR$ constructs

In order to optimize $GABA_BR$ expression in neurons, I sub-cloned the existing $GABA_BR$ plasmids driven by the cytomegalovirus (CMV) promoter to generate new plasmids coding for $GABA_BRs$ under the control of the neuron-specific synapsin (SYN) promoter. The synapsin promoter was inserted to enhance the efficiency and specificity of the transfection of neurons[276, 277]. The plasmids coding for synapsin-driven $GABA_{B1a}R$ tagged at its extracellular N-terminus with an HA-tag and a SNAP-tag, or with an HA-tag and a CLIP-tag (pSYN-HA-SNAP-$GABA_{B1a}R$, pSYN-HA-CLIP-$GABA_{B1a}R$) were generated. CHO cells were cotransfected for 48 h with pSYN-HA-SNAP-$GABA_{B1}R$ or with pSYN-HA-CLIP-$GABA_{B1}R$. CLIP- or SNAP-tagged $GABA_{B2}$ subunit was cotransfected, respectively. Cells were labeled with a complete culture medium containing saturating concentration of the SNAP-surface AF549 (2 µM) and CLIP-surface AF647 (2 µM). Images were acquired by TIRFM. $GABA_BR$ constructs were expressed in the CHO cells and were correctly located at the plasma membrane (**Fig. 29**). However, all the experiments demonstrated in this thesis were conducted using $GABA_{B1}R$ plasmids under the control of CMV promoter. CMV promoter-driven plasmids showed higher expression in neurons in comparison to synapsin-driven ones. This might be attributed to the CMV stronger transcriptional activity in comparison to synapsin[276, 277].

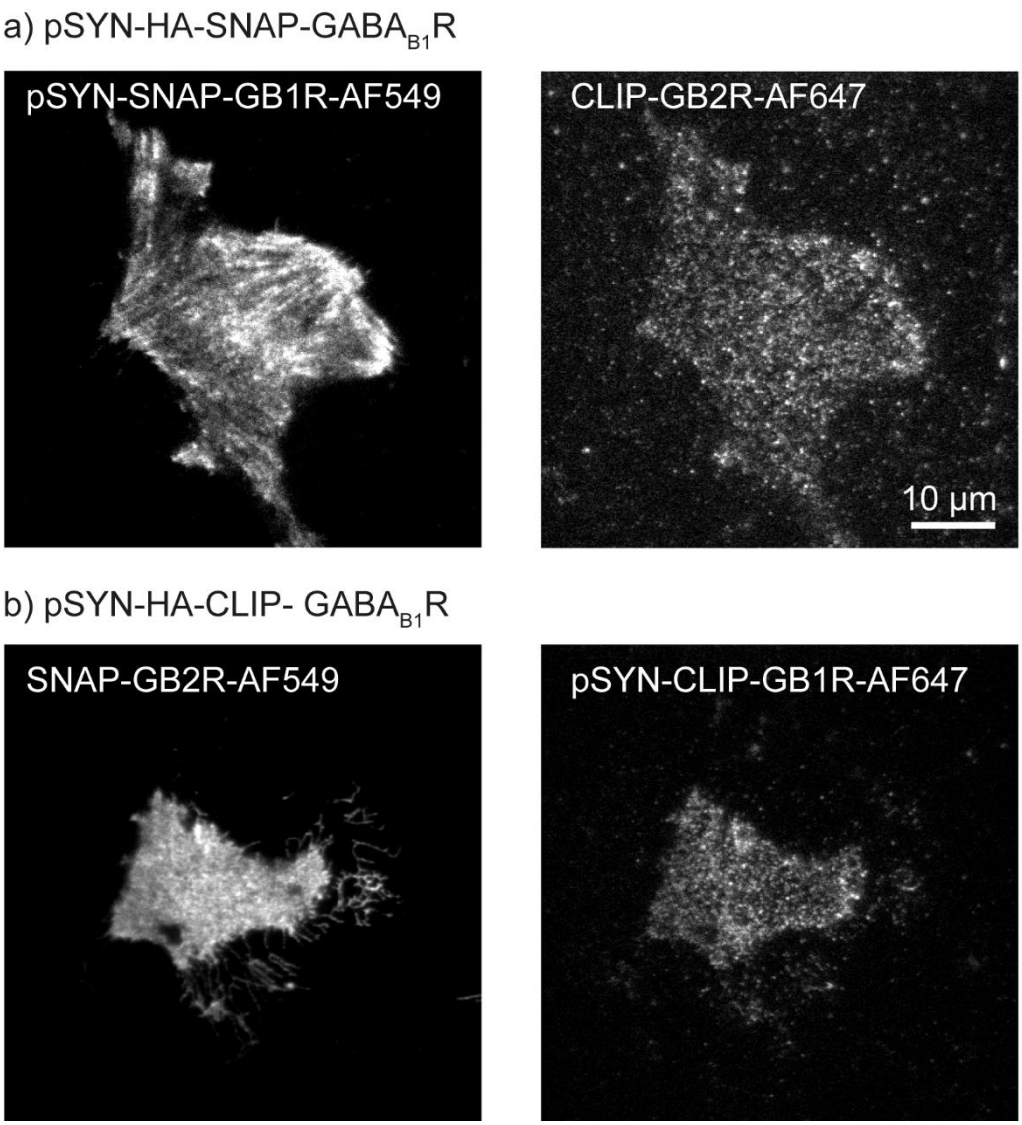

Figure 29: Expression and location of GABA$_B$Rs visualized by single-molecule TIRFM. Shown are representative TIRF images of CHO cells cotransfected for 48 h with DNA plasmids coding for **(a)** HA-SNAP-GABA$_{B1}$R and CLIP-GABA$_{B2}$R and **(b)** HA-CLIP-GABA$_{B1}$R and SNAP-GABA$_{B2}$R. GABA$_{B1}$R Cells were labeled with saturating concentration of the cell-impermeable SNAP and CLIP substrates. Subsequently, images were acquired by TIRFM. Dots are individual GABA$_B$ subunits.

9 References

1. Pierce KL, Premont RT, Lefkowitz RJ. Seven-transmembrane receptors. *Nat Rev Mol Cell Biol* **3**, 639-650 (2002).

2. Lefkowitz RJ. A brief history of G-protein coupled receptors (Nobel Lecture). *Angew Chem Int Ed Engl* **52**, 6366-6378 (2013).

3. Rask-Andersen M, Almen MS, Schioth HB. Trends in the exploitation of novel drug targets. *Nat Rev Drug Discov* **10**, 579-590 (2011).

4. Dolwing JE, Ratliff F. Nobel prize: 3 named for medicine, physiology award (George Wald, Ragnar Granit and Haldan Keffer Hartline). *Science* **158**, 468-473 (1967).

5. Sutherland EW. Studies on the mechanism of hormone action. *Science* **177**, 401-408 (1972).

6. Raju TN. The Nobel chronicles. 1994: Alfred G Gilman (b 1941) and Martin Rodbell (1925-98). *Lancet* **355**, 2259 (2000).

7. Axel R. Scents and sensibility: a molecular logic of olfactory perception (Nobel lecture). *Angew Chem Int Ed Engl* **44**, 6110-6127 (2005).

8. Buck LB. Unraveling the sense of smell (Nobel lecture). *Angew Chem Int Ed Engl* **44**, 6128-6140 (2005).

9. Attwood TK, Findlay JBC. Fingerprinting G-Protein-Coupled Receptors. *Protein Eng* **7**, 195-203 (1994).

10. Kolakowski LF, Jr. GCRDb: a G-protein-coupled receptor database. *Receptors Channels* **2**, 1-7 (1994).

11. Ghanouni P*, et al.* Functionally different agonists induce distinct conformations in the G protein coupling domain of the beta(2) adrenergic receptor. *Journal of Biological Chemistry* **276**, 24433-24436 (2001).

12. Farrens DL, Altenbach C, Yang K, Hubbell WL, Khorana HG. Requirement of rigid-body motion of transmembrane helices for light activation of rhodopsin. *Science* **274**, 768-770 (1996).

13. Sheikh SP, Zvyaga TA, Lichtarge O, Sakmar TP, Bourne HR. Rhodopsin activation blocked by metal-ion-binding sites linking transmembrane helices C and F. *Nature* **383**, 347-350 (1996).

14. Heuss C, Gerber U. G-protein-independent signaling by G-protein-coupled receptors. *Trends in Neurosciences* **23**, 469-475 (2000).

15. Hall RA, Premont RT, Lefkowitz RJ. Heptahelical receptor signaling: beyond the G protein paradigm. *J Cell Biol* **145**, 927-932 (1999).

16. Ribas C*, et al.* The G protein-coupled receptor kinase (GRK) interactome: role of GRKs in GPCR regulation and signaling. *Biochim Biophys Acta* **1768**, 913-922 (2007).

17. Cahill TJ, 3rd*, et al.* Distinct conformations of GPCR-beta-arrestin complexes mediate desensitization, signaling, and endocytosis. *Proc Natl Acad Sci U S A* **114**, 2562-2567 (2017).

18. Bjarnadottir TK, Fredriksson R, Schioth HB. The gene repertoire and the common evolutionary history of glutamate, pheromone (V2R), taste(1) and other related G protein-coupled receptors. *Gene* **362**, 70-84 (2005).

19. Pin JP, Galvez T, Prezeau L. Evolution, structure, and activation mechanism of family 3/C G-protein-coupled receptors. *Pharmacol Therapeut* **98**, 325-354 (2003).

20. Fredriksson R, Lagerstrom MC, Lundin LG, Schioth HB. The G-protein-coupled receptors in the human genome form five main families. Phylogenetic analysis, paralogon groups, and fingerprints. *Mol Pharmacol* **63**, 1256-1272 (2003).

21. Cao J*, et al.* Evolution of the class C GPCR Venus flytrap modules involved positive selected functional divergence. *BMC Evol Biol* **9**, 67 (2009).

22. Dissous C, Morel M, Vanderstraete M. Venus kinase receptors: prospects in signaling and biological functions of these invertebrate kinases. *Front Endocrinol (Lausanne)* **5**, 72 (2014).

23. Francesconi A, Duvoisin RM. Divalent cations modulate the activity of metabotropic glutamate receptors. *J Neurosci Res* **75**, 472-479 (2004).

24. Bourne HR. How receptors talk to trimeric G proteins. *Current Opinion in Cell Biology* **9**, 134-142 (1997).

25. Wess J. G-protein-coupled receptors: molecular mechanisms involved in receptor activation and selectivity of G-protein recognition. *FASEB J* **11**, 346-354 (1997).

26. Enz R. Structure of metabotropic glutamate receptor C-terminal domains in contact with interacting proteins. *Front Mol Neurosci* **5**, 52 (2012).

27. Niswender CM, Conn PJ. Metabotropic glutamate receptors: physiology, pharmacology, and disease. *Annu Rev Pharmacol Toxicol* **50**, 295-322 (2010).

28. Conn PJ, Pin JP. Pharmacology and functions of metabotropic glutamate receptors. *Annu Rev Pharmacol Toxicol* **37**, 205-237 (1997).

29. Ferraguti F, Shigemoto R. Metabotropic glutamate receptors. *Cell Tissue Res* **326**, 483-504 (2006).

30. Hermans E, Challiss RA. Structural, signalling and regulatory properties of the group I metabotropic glutamate receptors: prototypic family C G-protein-coupled receptors. *Biochem J* **359**, 465-484 (2001).

31. Aramori I, Nakanishi S. Signal transduction and pharmacological characteristics of a metabotropic glutamate receptor, mGluR1, in transfected CHO cells. *Neuron* **8**, 757-765 (1992).

32. Joly C, Gomeza J, Brabet I, Curry K, Bockaert J, Pin JP. Molecular, functional, and pharmacological characterization of the metabotropic glutamate receptor type 5 splice variants: comparison with mGluR1. *J Neurosci* **15**, 3970-3981 (1995).

33. Page G*, et al.* Group I metabotropic glutamate receptors activate the p70S6 kinase via both mammalian target of rapamycin (mTOR) and extracellular signal-regulated kinase (ERK 1/2) signaling pathways in rat striatal and hippocampal synaptoneurosomes. *Neurochem Int* **49**, 413-421 (2006).

34. Choi S, Lovinger DM. Metabotropic glutamate receptor modulation of voltage-gated Ca2+ channels involves multiple receptor subtypes in cortical neurons. *J Neurosci* **16**, 36-45 (1996).

35. Knoflach F, Kemp JA. Metabotropic glutamate group II receptors activate a G protein-coupled inwardly rectifying K+ current in neurones of the rat cerebellum. *J Physiol* **509 (Pt 2)**, 347-354 (1998).

36. Masu M*, et al.* Specific deficit of the ON response in visual transmission by targeted disruption of the mGluR6 gene. *Cell* **80**, 757-765 (1995).

37. Gassmann M, Bettler B. Regulation of neuronal GABA(B) receptor functions by subunit composition. *Nat Rev Neurosci* **13**, 380-394 (2012).

38. Chalifoux JR, Carter AG. GABAB receptor modulation of synaptic function. *Curr Opin Neurobiol* **21**, 339-344 (2011).

39. Duthey B*, et al.* A single subunit (GB2) is required for G-protein activation by the heterodimeric GABA(B) receptor. *Journal of Biological Chemistry* **277**, 3236-3241 (2002).

40. Calver AR*, et al.* The C-terminal domains of the GABA(B) receptor subunits mediate intracellular trafficking but are not required for receptor signaling. *Journal of Neuroscience* **21**, 1203-1210 (2001).

41. Pagano A*, et al.* C-terminal interaction is essential for surface trafficking but not for heteromeric assembly of GABA(B) receptors. *Journal of Neuroscience* **21**, 1189-1202 (2001).

42. Margeta-Mitrovic M, Jan YN, Jan LY. A trafficking checkpoint controls GABA(B) receptor heterodimerization. *Neuron* **27**, 97-106 (2000).

43. Ishikawa T, Kaneko M, Shin HS, Takahashi T. Presynaptic N-type and P/Q-type Ca2+ channels mediating synaptic transmission at the calyx of Held of mice. *J Physiol* **568**, 199-209 (2005).

44. Laviv T*, et al.* Compartmentalization of the GABA(B) Receptor Signaling Complex Is Required for Presynaptic Inhibition at Hippocampal Synapses. *Journal of Neuroscience* **31**, 12523-12532 (2011).

45. Gahwiler BH, Brown DA. GABAB-receptor-activated K+ current in voltage-clamped CA3 pyramidal cells in hippocampal cultures. *Proc Natl Acad Sci U S A* **82**, 1558-1562 (1985).

46. Terrillon S, Bouvier M. Roles of G-protein-coupled receptor dimerization. *EMBO Rep* **5**, 30-34 (2004).

47. Calebiro D*, et al.* Single-molecule analysis of fluorescently labeled G-protein-coupled receptors reveals complexes with distinct dynamics and organization. *Proc Natl Acad Sci U S A* **110**, 743-748 (2013).

48. Kasai RS, Kusumi A. Single-molecule imaging revealed dynamic GPCR dimerization. *Curr Opin Cell Biol* **27**, 78-86 (2014).

49. Kniazeff J, Prezeau L, Rondard P, Pin JP, Goudet C. Dimers and beyond: The functional puzzles of class C GPCRs. *Pharmacol Ther* **130**, 9-25 (2011).

50. Pin JP*, et al.* G-protein-coupled receptor oligomers: two or more for what ? Lessons from mGlu and GABA(B) receptors. *J Physiol-London* **587**, 5337-5344 (2009).

51. Levitz J, Habrian C, Bharill S, Fu Z, Vafabakhsh R, Isacoff EY. Mechanism of Assembly and Cooperativity of Homomeric and Heteromeric Metabotropic Glutamate Receptors. *Neuron* **92**, 143-159 (2016).

52. Muto T, Tsuchiya D, Morikawa K, Jingami H. Structures of the extracellular regions of the group II/III metabotropic glutamate receptors. *Proc Natl Acad Sci U S A* **104**, 3759-3764 (2007).

53. Kunishima N*, et al.* Structural basis of glutamate recognition by a dimeric metabotropic glutamate receptor. *Nature* **407**, 971-977 (2000).

54. Romano C, Yang WL, O'Malley KL. Metabotropic glutamate receptor 5 is a disulfide-linked dimer. *J Biol Chem* **271**, 28612-28616 (1996).

55. Doumazane E, Scholler P, Zwier JM, Trinquet E, Rondard P, Pin JP. A new approach to analyze cell surface protein complexes reveals specific heterodimeric metabotropic glutamate receptors. *FASEB J* **25**, 66-77 (2011).

56. Woods AS, Ferre S. Amazing stability of the arginine-phosphate electrostatic interaction. *J Proteome Res* **4**, 1397-1402 (2005).

57. El Moustaine D*, et al.* Distinct roles of metabotropic glutamate receptor dimerization in agonist activation and G-protein coupling. *Proc Natl Acad Sci U S A* **109**, 16342-16347 (2012).

58. Goudet C*, et al.* Heptahelical domain of metabotropic glutamate receptor 5 behaves like rhodopsin-like receptors. *Proc Natl Acad Sci U S A* **101**, 378-383 (2004).

59. White JH*, et al.* Heterodimerization is required for the formation of a functional GABA(B) receptor. *Nature* **396**, 679-682 (1998).

60. Huang J, Chen S, Zhang JJ, Huang XY. Crystal structure of oligomeric beta1-adrenergic G protein-coupled receptors in ligand-free basal state. *Nat Struct Mol Biol* **20**, 419-425 (2013).

61. Wu BL*, et al.* Structures of the CXCR4 Chemokine GPCR with Small-Molecule and Cyclic Peptide Antagonists. *Science* **330**, 1066-1071 (2010).

62. Wu HX*, et al.* Structure of the human kappa-opioid receptor in complex with JDTic. *Nature* **485**, 327-U369 (2012).

63. Manglik A*, et al.* Crystal structure of the mu-opioid receptor bound to a morphinan antagonist. *Nature* **485**, 321-U170 (2012).

64. Dijkman PM*, et al.* Dynamic tuneable G protein-coupled receptor monomer-dimer populations. *Nat Commun* **9**, 1710 (2018).

65. Maurel D*, et al.* Cell-surface protein-protein interaction analysis with time-resolved FRET and snap-tag technologies: application to GPCR oligomerization. *Nat Methods* **5**, 561-567 (2008).

66. Comps-Agrar L, Kniazeff J, Brock C, Trinquet E, Pin JP. Stability of GABAB receptor oligomers revealed by dual TR-FRET and drug-induced cell surface targeting. *FASEB J* **26**, 3430-3439 (2012).

67. Moller TC*, et al.* Oligomerization of a G protein-coupled receptor in neurons controlled by its structural dynamics. *Sci Rep* **8**, 10414 (2018).

68. The oligomeric state sets GABAB receptor signalling efficacy.

69. Lum JS*, et al.* Neurodevelopmental Expression Profile of Dimeric and Monomeric Group 1 mGluRs: Relevance to Schizophrenia Pathogenesis and Treatment. *Sci Rep* **6**, 34391 (2016).

70. Kandel ER, Schwartz JH, Jessell TM, Siegelbaum SA, Hudspeth AJ. *Principles of Neural Science*. McGraw-Hill Publishing (2012).

71. Katz B. *The Release of Neural Transmitter Substances*. Springfield II (1969).

72. Katz B. Neural transmitter release: from quantal secretion to exocytosis and beyond. The Fenn Lecture. *J Neurocytol* **25**, 677-686 (1996).

73. Heuser JE, Reese TS. Structural changes after transmitter release at the frog neuromuscular junction. *J Cell Biol* **88**, 564-580 (1981).

74. Schneggenburger R, Neher E. Intracellular calcium dependence of transmitter release rates at a fast central synapse. *Nature* **406**, 889-893 (2000).

75. Stanley EF. The calcium channel and the organization of the presynaptic transmitter release face. *Trends Neurosci* **20**, 404-409 (1997).

76. Rothman JE. A Protein Assembly-Disassembly Pathway in-Vitro That May Correspond to Sequential Steps of Synaptic Vesicle Docking, Activation and Fusion. *Journal of Neurochemistry* **62**, S65-S65 (1994).

77. Gao Y*, et al.* Single reconstituted neuronal SNARE complexes zipper in three distinct stages. *Science* **337**, 1340-1343 (2012).

78. Sutton RB, Fasshauer D, Jahn R, Brunger AT. Crystal structure of a SNARE complex involved in synaptic exocytosis at 2.4 angstrom resolution. *Nature* **395**, 347-353 (1998).

79. Yang B, Steegmaier M, Gonzalez LC, Jr., Scheller RH. nSec1 binds a closed conformation of syntaxin1A. *J Cell Biol* **148**, 247-252 (2000).

80. de Wit H. Molecular mechanism of secretory vesicle docking. *Biochem Soc Trans* **38**, 192-198 (2010).

81. Verhage M, Sorensen JB. Vesicle docking in regulated exocytosis. *Traffic* **9**, 1414-1424 (2008).

82. Burgoyne RD, Morgan A. Chaperoning the SNAREs: a role in preventing neurodegeneration? *Nat Cell Biol* **13**, 8-9 (2011).

83. Kochubey O, Schneggenburger R. Synaptotagmin increases the dynamic range of synapses by driving Ca(2)+-evoked release and by clamping a near-linear remaining Ca(2)+ sensor. *Neuron* **69**, 736-748 (2011).

84. Vermaas JV, Tajkhorshid E. Differential Membrane Binding Mechanics of Synaptotagmin Isoforms Observed in Atomic Detail. *Biochemistry* **56**, 281-293 (2017).

85. Okabe S. Molecular anatomy of the postsynaptic density. *Mol Cell Neurosci* **34**, 503-518 (2007).

86. Sheng M, Hoogenraad CC. The postsynaptic architecture of excitatory synapses: a more quantitative view. *Annu Rev Biochem* **76**, 823-847 (2007).

87. Sudhof TC. The presynaptic active zone. *Neuron* **75**, 11-25 (2012).

88. Gray EG. Electron microscopy of presynaptic organelles of the spinal cord. *J Anat* **97**, 101-106 (1963).

89. Zhai RG, Bellen HJ. The architecture of the active zone in the presynaptic nerve terminal. *Physiology (Bethesda)* **19**, 262-270 (2004).

90. Squire L, Berg d, Bloom F, Lac SD, Ghosh A, Spitzer N. *Fundamental Neuroscience*, Third edn. Elsevier (2008).

91. Siksou L*, et al.* Three-dimensional architecture of presynaptic terminal cytomatrix. *J Neurosci* **27**, 6868-6877 (2007).

92. Indriati DW, Kamasawa N, Matsui K, Meredith AL, Watanabe M, Shigemoto R. Quantitative localization of Cav2.1 (P/Q-type) voltage-dependent calcium channels in Purkinje cells: somatodendritic gradient and distinct somatic coclustering with calcium-activated potassium channels. *J Neurosci* **33**, 3668-3678 (2013).

93. Harris KM, Stevens JK. Dendritic spines of rat cerebellar Purkinje cells: serial electron microscopy with reference to their biophysical characteristics. *J Neurosci* **8**, 4455-4469 (1988).

94. Harlow ML, Ress D, Stoschek A, Marshall RM, McMahan UJ. The architecture of active zone material at the frog's neuromuscular junction. *Nature* **409**, 479-484 (2001).

95. Atwood HL, Govind CK, Wu CF. Differential Ultrastructure of Synaptic Terminals on Ventral Longitudinal Abdominal Muscles in Drosophila Larvae. *Journal of Neurobiology* **24**, 1008-1024 (1993).

96. Kittel RJ*, et al.* Bruchpilot promotes active zone assembly, Ca2+ channel clustering, and vesicle release. *Science* **312**, 1051-1054 (2006).

97. Matthews G, Fuchs P. The diverse roles of ribbon synapses in sensory neurotransmission. *Nature Reviews Neuroscience* **11**, 812-822 (2010).

98. Dresbach T, Qualmann B, Kessels MM, Garner CC, Gundelfinger ED. The presynaptic cytomatrix of brain synapses. *Cell Mol Life Sci* **58**, 94-116 (2001).

99. Nakata T*, et al.* Fusion of a novel gene, ELKS, to RET due to translocation t(10;12)(q11;p13) in a papillary thyroid carcinoma. *Genes Chromosomes Cancer* **25**, 97-103 (1999).

100. Iezzi M, Regazzi R, Wollheim CB. The Rab3-interacting molecule RIM is expressed in pancreatic beta-cells and is implicated in insulin exocytosis. *Febs Letters* **474**, 66-70 (2000).

101. Betz A*, et al.* Functional interaction of the active zone proteins Munc13-1 and RIM1 in synaptic vesicle priming. *Neuron* **30**, 183-196 (2001).

102. Graf ER*, et al.* RIM promotes calcium channel accumulation at active zones of the Drosophila neuromuscular junction. *J Neurosci* **32**, 16586-16596 (2012).

103. Kaeser PS*, et al.* RIM proteins tether Ca2+ channels to presynaptic active zones via a direct PDZ-domain interaction. *Cell* **144**, 282-295 (2011).

104. Fernandez-Busnadiego R*, et al.* Cryo-electron tomography reveals a critical role of RIM1 alpha in synaptic vesicle tethering. *Journal of Cell Biology* **201**, 725-740 (2013).

105. Castillo PE, Schoch S, Schmitz F, Sudhof TC, Malenka RC. RIM1 alpha is required for presynaptic long-term potentiation. *Nature* **415**, 327-330 (2002).

106. Schoch S*, et al.* RIM1 alpha forms a protein scaffold for regulating neurotransmitter release at the active zone. *Nature* **415**, 321-326 (2002).

107. Gerber SH*, et al.* Conformational switch of syntaxin-1 controls synaptic vesicle fusion. *Science* **321**, 1507-1510 (2008).

108. Garcia-Junco-Clemente P, Linares-Clemente P, Fernandez-Chacon R. Active zones for presynaptic plasticity in the brain. *Mol Psychiatry* **10**, 185-200; image 131 (2005).

109. Mukherjee K*, et al.* Piccolo and bassoon maintain synaptic vesicle clustering without directly participating in vesicle exocytosis. *Proc Natl Acad Sci U S A* **107**, 6504-6509 (2010).

110. Altrock WD*, et al.* Functional inactivation of a fraction of excitatory synapses in mice deficient for the active zone protein bassoon. *Neuron* **37**, 787-800 (2003).

111. Sudhof TC, Rothman JE. Membrane Fusion: Grappling with SNARE and SM Proteins. *Science* **323**, 474-477 (2009).

112. Betke KM, Wells CA, Hamm HE. GPCR mediated regulation of synaptic transmission. *Prog Neurobiol* **96**, 304-321 (2012).

113. Forscher P, Oxford GS, Schulz D. Noradrenaline Modulates Calcium Channels in Avian Dorsal-Root Ganglion-Cells through Tight Receptor Channel Coupling. *J Physiol-London* **379**, 131-144 (1986).

114. Tedford HW, Zamponi GW. Direct G protein modulation of Cav2 calcium channels. *Pharmacol Rev* **58**, 837-862 (2006).

115. Kajikawa Y, Saitoh N, Takahashi T. GTP-binding protein beta gamma subunits mediate presynaptic calcium current inhibition by GABA(B) receptor. *Proc Natl Acad Sci U S A* **98**, 8054-8058 (2001).

116. Gundlfinger A, Bischofberger J, Johenning FW, Torvinen M, Schmitz D, Breustedt J. Adenosine modulates transmission at the hippocampal mossy fibre synapse via direct inhibition of presynaptic calcium channels. *J Physiol* **582**, 263-277 (2007).

117. Catterall WA. Structure and regulation of voltage-gated Ca2+ channels. *Annu Rev Cell Dev Biol* **16**, 521-555 (2000).

118. Bean BP. Neurotransmitter inhibition of neuronal calcium currents by changes in channel voltage dependence. *Nature* **340**, 153-156 (1989).

119. Dolphin AC. G protein modulation of voltage-gated calcium channels. *Pharmacol Rev* **55**, 607-627 (2003).

120. Fernandez-Alacid L*, et al.* Subcellular compartment-specific molecular diversity of pre- and post-synaptic GABA-activated GIRK channels in Purkinje cells. *J Neurochem* **110**, 1363-1376 (2009).

121. Kulik A*, et al.* Compartment-dependent colocalization of Kir3.2-containing K+ channels and GABAB receptors in hippocampal pyramidal cells. *J Neurosci* **26**, 4289-4297 (2006).

122. Ikeda K, Yoshii M, Sora I, Kobayashi T. Opioid receptor coupling to GIRK channels. In vitro studies using a Xenopus oocyte expression system and in vivo studies on weaver mutant mice. *Methods Mol Med* **84**, 53-64 (2003).

123. Huang CL, Slesinger PA, Casey PJ, Jan YN, Jan LY. Evidence That Direct Binding of G(Beta-Gamma) to the Girk1 G-Protein-Gated Inwardly Rectifying K+ Channel Is Important for Channel Activation. *Neuron* **15**, 1133-1143 (1995).

124. Yoon EJ, Gerachshenko T, Spiegelberg BD, Alford S, Hamm HE. Gbetagamma interferes with Ca2+-dependent binding of synaptotagmin to the soluble N-ethylmaleimide-sensitive factor attachment protein receptor (SNARE) complex. *Mol Pharmacol* **72**, 1210-1219 (2007).

125. Shigemoto R*, et al.* Differential presynaptic localization of metabotropic glutamate receptor subtypes in the rat hippocampus. *J Neurosci* **17**, 7503-7522 (1997).

126. Gilman AG. G proteins and dual control of adenylate cyclase. *Cell* **36**, 577-579 (1984).

127. Surmeier DJ, Bargas J, Hemmings HC, Nairn AC, Greengard P. Modulation of Calcium Currents by a D-1 Dopaminergic Protein-Kinase Phosphatase Cascade in Rat Neostriatal Neurons. *Neuron* **14**, 385-397 (1995).

128. Gamper N, Reznikov V, Yamada Y, Yang J, Shapiro MS. Phosphatidylinositol [correction] 4,5-bisphosphate signals underlie receptor-specific Gq/11-mediated modulation of N-type Ca2+ channels. *J Neurosci* **24**, 10980-10992 (2004).

129. Delmas P, Coste B, Gamper N, Shapiro MS. Phosphoinositide lipid second messengers: new paradigms for calcium channel modulation. *Neuron* **47**, 179-182 (2005).

130. Kammermeier PJ, Ruiz-Velasco V, Ikeda SR. A voltage-independent calcium current inhibitory pathway activated by muscarinic agonists in rat sympathetic neurons requires both G alpha(q/11) and G beta gamma. *Journal of Neuroscience* **20**, 5623-5629 (2000).

131. Brown DA, Sihra TS. Presynaptic signaling by heterotrimeric G-proteins. *Handb Exp Pharmacol*, 207-260 (2008).

132. Wang SJ, Coutinho V, Sihra TS. Presynaptic cross-talk of beta-adrenoreceptor and 5-hydroxytryptamine receptor signalling in the modulation of glutamate release from cerebrocortical nerve terminals. *Br J Pharmacol* **137**, 1371-1379 (2002).

133. Davare MA*, et al.* A beta2 adrenergic receptor signaling complex assembled with the Ca2+ channel Cav1.2. *Science* **293**, 98-101 (2001).

134. Lujan R*, et al.* Differential association of GABA(B) receptors with their effector ion channels in Purkinje cells. *Brain Struct Funct* **223**, 1565-1587 (2018).

135. Kitano J*, et al.* Direct interaction and functional coupling between metabotropic glutamate receptor subtype 1 and voltage-sensitive Ca(v)2.1 Ca2+ channel. *Journal of Biological Chemistry* **278**, 25101-25108 (2003).

136. Augustine GJ, Santamaria F, Tanaka K. Local calcium signaling in neurons. *Neuron* **40**, 331-346 (2003).

137. Kisilevsky AE, Zamponi GW. D2 dopamine receptors interact directly with N-type calcium channels and regulate channel surface expression levels. *Channels (Austin)* **2**, 269-277 (2008).

138. Kisilevsky AE*, et al.* D1 receptors physically interact with N-type calcium channels to regulate channel distribution and dendritic calcium entry. *Neuron* **58**, 557-570 (2008).

139. Evans RM*, et al.* Heterodimerization of ORL1 and opioid receptors and its consequences for N-type calcium channel regulation. *J Biol Chem* **285**, 1032-1040 (2010).

140. Ramos C*, et al.* Native presynaptic metabotropic glutamate receptor 4 (mGluR4) interacts with exocytosis proteins in rat cerebellum. *J Biol Chem* **287**, 20176-20186 (2012).

141. Lefkowitz RJ. G protein-coupled receptors III. New roles for receptor kinases and beta-arrestins in receptor signaling and desensitization. *Journal of Biological Chemistry* **273**, 18677-18680 (1998).

142. Ahn S, Maudsley S, Luttrell LM, Lefkowitz RJ, Daaka Y. Src-mediated tyrosine phosphorylation of dynamin is required for beta(2)-adrenergic receptor internalization and mitogen-activated protein kinase signaling. *Journal of Biological Chemistry* **274**, 1185-1188 (1999).

143. Luttrell LM*, et al.* Beta-arrestin-dependent formation of beta2 adrenergic receptor-Src protein kinase complexes. *Science* **283**, 655-661 (1999).

144. Luttrell LM, Daaka Y, Lefkowitz RJ. Regulation of tyrosine kinase cascades by G-protein-coupled receptors. *Curr Opin Cell Biol* **11**, 177-183 (1999).

145. Shenoy SK*, et al.* beta-arrestin-dependent, G protein-independent ERK1/2 activation by the beta2 adrenergic receptor. *J Biol Chem* **281**, 1261-1273 (2006).

146. Tu JC*, et al.* Homer binds a novel proline-rich motif and links group 1 metabotropic glutamate receptors with IP3 receptors. *Neuron* **21**, 717-726 (1998).

147. Mao L, Yang L, Tang Q, Samdani S, Zhang G, Wang JQ. The scaffold protein Homer1b/c links metabotropic glutamate receptor 5 to extracellular signal-regulated protein kinase cascades in neurons. *J Neurosci* **25**, 2741-2752 (2005).

148. Boudin H*, et al.* Presynaptic clustering of mGluR7a requires the PICK1 PDZ domain binding site. *Neuron* **28**, 485-497 (2000).

149. Perroy J*, et al.* PICK1 is required for the control of synaptic transmission by the metabotropic glutamate receptor 7. *Embo Journal* **21**, 2990-2999 (2002).

150. Fraser IDC*, et al.* Assembly of an A kinase-anchoring protein-beta(2)-adrenergic receptor complex facilitates receptor phosphorylation and signaling. *Curr Biol* **10**, 409-412 (2000).

151. Bliss TV, Collingridge GL. A synaptic model of memory: long-term potentiation in the hippocampus. *Nature* **361**, 31-39 (1993).

152. Collingridge GL, Isaac JT, Wang YT. Receptor trafficking and synaptic plasticity. *Nat Rev Neurosci* **5**, 952-962 (2004).

153. Davies CH, Starkey SJ, Pozza MF, Collingridge GL. GABA autoreceptors regulate the induction of LTP. *Nature* **349**, 609-611 (1991).

154. Bortolotto ZA, Bashir ZI, Davies CH, Collingridge GL. A molecular switch activated by metabotropic glutamate receptors regulates induction of long-term potentiation. *Nature* **368**, 740-743 (1994).

155. Bolshakov VY, Siegelbaum SA. Postsynaptic induction and presynaptic expression of hippocampal long-term depression. *Science* **264**, 1148-1152 (1994).

156. Triller A, Choquet D. Surface trafficking of receptors between synaptic and extrasynaptic membranes: and yet they do move! *Trends in Neurosciences* **28**, 133-139 (2005).

157. Benke TA, Luthi A, Isaac JT, Collingridge GL. Modulation of AMPA receptor unitary conductance by synaptic activity. *Nature* **393**, 793-797 (1998).

158. Tardin C, Cognet L, Bats C, Lounis B, Choquet D. Direct imaging of lateral movements of AMPA receptors inside synapses. *EMBO J* **22**, 4656-4665 (2003).

159. Tovar KR, Westbrook GL. Mobile NMDA receptors at hippocampal synapses. *Neuron* **34**, 255-264 (2002).

160. Levine MS, Cepeda C, Andre VM. Location, Location, Location: Contrasting Roles of Synaptic and Extrasynaptic NMDA Receptors in Huntington's Disease. *Neuron* **65**, 145-147 (2010).

161. Papadia S, Hardingham GE. The dichotomy of NMDA receptor signaling. *Neuroscientist* **13**, 572-579 (2007).

162. Kennedy MB. The postsynaptic density at glutamatergic synapses. *European Journal of Neuroscience* **10**, 207-207 (1998).

163. Fischer F*, et al.* Reduced synaptic clustering of GABA and glycine receptors in the retina of the gephyrin null mutant mouse. *Journal of Comparative Neurology* **427**, 634-648 (2000).

164. Kneussel M, Betz H. Clustering of inhibitory neurotransmitter receptors at developing postsynaptic sites: the membrane activation model. *Trends in Neurosciences* **23**, 429-435 (2000).

165. Kneussel M, Betz H. Receptors, gephyrin and gephyrin-associated proteins: novel insights into the assembly of inhibitory postsynaptic membrane specializations. *J Physiol-London* **525**, 1-9 (2000).

166. Sealock R, Wray BE, Froehner SC. Ultrastructural localization of the Mr 43,000 protein and the acetylcholine receptor in Torpedo postsynaptic membranes using monoclonal antibodies. *J Cell Biol* **98**, 2239-2244 (1984).

167. Sanes JR, Lichtman JW. Development of the vertebrate neuromuscular junction. *Annu Rev Neurosci* **22**, 389-442 (1999).

168. Steigerwald F, Schulz TW, Schenker LT, Kennedy MB, Seeburg PH, Kohr G. C-Terminal truncation of NR2A subunits impairs synaptic but not extrasynaptic localization of NMDA receptors. *J Neurosci* **20**, 4573-4581 (2000).

169. Mori H*, et al.* Role of the carboxy-terminal region of the GluR epsilon2 subunit in synaptic localization of the NMDA receptor channel. *Neuron* **21**, 571-580 (1998).

170. Serge A, Fourgeaud L, Hemar A, Choquet D. Receptor activation and homer differentially control the lateral mobility of metabotropic glutamate receptor 5 in the neuronal membrane. *Journal of Neuroscience* **22**, 3910-3920 (2002).

171. Ango F*, et al.* Dendritic and axonal targeting of type 5 metabotropic glutamate receptor is regulated by homer1 proteins and neuronal excitation. *J Neurosci* **20**, 8710-8716 (2000).

172. Roche KW, Tu JC, Petralia RS, Xiao B, Wenthold RJ, Worley PF. Homer 1b regulates the trafficking of group I metabotropic glutamate receptors. *Journal of Biological Chemistry* **274**, 25953-25957 (1999).

173. Ladepeche L, Yang LT, Bouchet D, Groc L. Regulation of Dopamine D1 Receptor Dynamics within the Postsynaptic Density of Hippocampal Glutamate Synapses. *Plos One* **8**, (2013).

174. Lelouvier B*, et al.* Dynamics of somatostatin type 2A receptor cargoes in living hippocampal neurons. *J Neurosci* **28**, 4336-4349 (2008).

175. Stefani A, Pisani A, Mercuri NB, Bernardi G, Calabresi P. Activation of metabotropic glutamate receptors inhibits calcium currents and GABA-mediated synaptic potentials in striatal neurons. *J Neurosci* **14**, 6734-6743 (1994).

176. Poncer JC, Shinozaki H, Miles R. Dual modulation of synaptic inhibition by distinct metabotropic glutamate receptors in the rat hippocampus. *J Physiol* **485 (Pt 1)**, 121-134 (1995).

177. Kulik A*, et al.* Subcellular localization of metabotropic GABA(B) receptor subunits GABA(B1a/b) and GABA(B2) in the rat hippocampus. *J Neurosci* **23**, 11026-11035 (2003).

178. Shigemoto R, Nakanishi S, Mizuno N. Distribution of the mRNA for a metabotropic glutamate receptor (mGluR1) in the central nervous system: an in situ hybridization study in adult and developing rat. *J Comp Neurol* **322**, 121-135 (1992).

179. Romano C, Sesma MA, McDonald CT, O'Malley K, Van den Pol AN, Olney JW. Distribution of metabotropic glutamate receptor mGluR5 immunoreactivity in rat brain. *J Comp Neurol* **355**, 455-469 (1995).

180. Baude A, Nusser Z, Roberts JDB, Mulvihill E, Mcilhinney RAJ, Somogyi P. The Metabotropic Glutamate-Receptor (Mglur1-Alpha) Is Concentrated at Perisynaptic Membrane of Neuronal Subpopulations as Detected by Immunogold Reaction. *Neuron* **11**, 771-787 (1993).

181. Nusser Z, Mulvihill E, Streit P, Somogyi P. Subsynaptic segregation of metabotropic and ionotropic glutamate receptors as revealed by immunogold localization. *Neuroscience* **61**, 421-427 (1994).

182. Aronica E, van Vliet EA, Mayboroda OA, Troost D, da Silva FH, Gorter JA. Upregulation of metabotropic glutamate receptor subtype mGluR3 and mGluR5 in reactive astrocytes in a rat model of mesial temporal lobe epilepsy. *Eur J Neurosci* **12**, 2333-2344 (2000).

183. Ferraguti F, Corti C, Valerio E, Mion S, Xuereb J. Activated astrocytes in areas of kainate-induced neuronal injury upregulate the expression of the metabotropic glutamate receptors 2/3 and 5. *Exp Brain Res* **137**, 1-11 (2001).

184. Tamaru Y, Nomura S, Mizuno N, Shigemoto R. Distribution of metabotropic glutamate receptor mGluR3 in the mouse CNS: differential location relative to pre- and postsynaptic sites. *Neuroscience* **106**, 481-503 (2001).

185. Ohishi H, Shigemoto R, Nakanishi S, Mizuno N. Distribution of the Messenger-Rna for a Metabotropic Glutamate Receptor, Mglur2, in the Central-Nervous-System of the Rat. *Neuroscience* **53**, 1009-1018 (1993).

186. Fotuhi M, Standaert DG, Testa CM, Penney JB, Jr., Young AB. Differential expression of metabotropic glutamate receptors in the hippocampus and entorhinal cortex of the rat. *Brain Res Mol Brain Res* **21**, 283-292 (1994).

187. Makoff A, Lelchuk R, Oxer M, Harrington K, Emson P. Molecular characterization and localization of human metabotropic glutamate receptor type 4. *Mol Brain Res* **37**, 239-248 (1996).

188. Bradley SR, Rees HD, Yi H, Levey AI, Conn PJ. Distribution and developmental regulation of metabotropic glutamate receptor 7a in rat brain. *Journal of Neurochemistry* **71**, 636-645 (1998).

189. Corti C*, et al.* Cloning and characterization of alternative mRNA forms for the rat metabotropic glutamate receptors mGluR7 and mGluR8. *Eur J Neurosci* **10**, 3629-3641 (1998).

190. Nakajima Y*, et al.* Molecular characterization of a novel retinal metabotropic glutamate receptor mGluR6 with a high agonist selectivity for L-2-amino-4-phosphonobutyrate. *J Biol Chem* **268**, 11868-11873 (1993).

191. Nomura A, Shigemoto R, Nakamura Y, Okamoto N, Mizuno N, Nakanishi S. Developmentally regulated postsynaptic localization of a metabotropic glutamate receptor in rat rod bipolar cells. *Cell* **77**, 361-369 (1994).

192. Kinoshita A, Ohishi H, Nomura S, Shigemoto R, Nakanishi S, Mizuno N. Presynaptic localization of a metabotropic glutamate receptor, mGluR4a, in the cerebellar cortex: a light and electron microscope study in the rat. *Neurosci Lett* **207**, 199-202 (1996).

193. Phillips T*, et al.* Immunohistochemical localisation of mGluR7 protein in the rodent and human cerebellar cortex using subtype specific antibodies. *Mol Brain Res* **57**, 132-141 (1998).

194. Bowery NG, Hudson AL, Price GW. GABAA and GABAB receptor site distribution in the rat central nervous system. *Neuroscience* **20**, 365-383 (1987).

195. Chu DC, Albin RL, Young AB, Penney JB. Distribution and kinetics of GABAB binding sites in rat central nervous system: a quantitative autoradiographic study. *Neuroscience* **34**, 341-357 (1990).

196. Charles KJ, Deuchars J, Davies CH, Pangalos MN. GABA B receptor subunit expression in glia. *Mol Cell Neurosci* **24**, 214-223 (2003).

197. Engers DW, Lindsley CW. Allosteric modulation of Class C GPCRs: a novel approach for the treatment of CNS disorders. *Drug Discov Today Technol* **10**, e269-276 (2013).

198. Schoepp DD, Wright RA, Levine LR, Gaydos B, Potter WZ. LY354740, an mGlu2/3 receptor agonist as a novel approach to treat anxiety/stress. *Stress* **6**, 189-197 (2003).

199. Goudet C*, et al.* A novel selective metabotropic glutamate receptor 4 agonist reveals new possibilities for developing subtype selective ligands with therapeutic potential. *FASEB J* **26**, 1682-1693 (2012).

200. Patel S*, et al.* The effects of GABA(B) agonists and gabapentin on mechanical hyperalgesia in models of neuropathic and inflammatory pain in the rat. *Pain* **90**, 217-226 (2001).

201. Addolorato G, Caputo F, Capristo E, Colombo G, Gessa GL, Gasbarrini G. Ability of baclofen in reducing alcohol craving and intake: II--Preliminary clinical evidence. *Alcohol Clin Exp Res* **24**, 67-71 (2000).

202. Froestl W*, et al.* SGS742: the first GABA(B) receptor antagonist in clinical trials. *Biochem Pharmacol* **68**, 1479-1487 (2004).

203. Snead OC, 3rd. Evidence for GABAB-mediated mechanisms in experimental generalized absence seizures. *Eur J Pharmacol* **213**, 343-349 (1992).

204. Abbe E. Beiträge zur Theorie des Mikroskops und der mikroskopischenWahrnehmung. *ArchivfürMikroskop* **9**, 413– 418 (1873).

205. Rayleigh L. On the theory of optical images, with special reference to microscopy. *Philos Mag* **42**, 167-195 (1896).

206. Klar TA, Hell SW. Subdiffraction resolution in far-field fluorescence microscopy. *Opt Lett* **24**, 954-956 (1999).

207. Hell SW. Far-field optical nanoscopy. *Science* **316**, 1153-1158 (2007).

208. Heintzmann R, Cremer CG. Laterally modulated excitation microscopy: improvement of resolution by using a diffraction grating. In: *BiOS Europe '98* (ed^(eds). SPIE (1999).

209. Gustafsson MG. Surpassing the lateral resolution limit by a factor of two using structured illumination microscopy. *J Microsc* **198**, 82-87 (2000).

210. Betzig E*, et al.* Imaging intracellular fluorescent proteins at nanometer resolution. *Science* **313**, 1642-1645 (2006).

211. Hess ST, Girirajan TP, Mason MD. Ultra-high resolution imaging by fluorescence photoactivation localization microscopy. *Biophys J* **91**, 4258-4272 (2006).

212. Rust MJ, Bates M, Zhuang X. Sub-diffraction-limit imaging by stochastic optical reconstruction microscopy (STORM). *Nat Methods* **3**, 793-795 (2006).

213. Heilemann M*, et al.* Subdiffraction-resolution fluorescence imaging with conventional fluorescent probes. *Angew Chem Int Ed Engl* **47**, 6172-6176 (2008).

214. , (!!! INVALID CITATION !!! 171, 172, 173, 174, 175, 176).

215. Sauer M. Localization microscopy coming of age: from concepts to biological impact. *Journal of Cell Science* **126**, 3505-3513 (2013).

216. Klein T, Loschberger A, Proppert S, Wolter S, van de Linde SV, Sauer M. Live-cell dSTORM with SNAP-tag fusion proteins. *Nature Methods* **8**, 7-9 (2011).

217. Ehmann N*, et al.* Quantitative super-resolution imaging of Bruchpilot distinguishes active zone states. *Nature Communications* **5**, (2014).

218. van de Linde S, Sauer M, Heilemann M. Subdiffraction-resolution fluorescence imaging of proteins in the mitochondrial inner membrane with photoswitchable fluorophores. *J Struct Biol* **164**, 250-254 (2008).

219. van de Linde S, Krstic I, Prisner T, Doose S, Heilemann M, Sauer M. Photoinduced formation of reversible dye radicals and their impact on super-resolution imaging. *Photochem Photobiol Sci* **10**, 499-506 (2011).

220. van de Linde S, Sauer M. How to switch a fluorophore: from undesired blinking to controlled photoswitching. *Chem Soc Rev* **43**, 1076-1087 (2014).

221. van de Linde S*, et al.* Direct stochastic optical reconstruction microscopy with standard fluorescent probes. *Nat Protoc* **6**, 991-1009 (2011).

222. Tian H, Furstenberg A, Huber T. Labeling and Single-Molecule Methods To Monitor G Protein-Coupled Receptor Dynamics. *Chem Rev*, (2016).

223. Delgado-Peraza F, Nogueras-Ortiz C, Acevedo Canabal AM, Roman-Vendrell C, Yudowski GA. Imaging GPCRs trafficking and signaling with total internal reflection fluorescence microscopy in cultured neurons. *Methods Cell Biol* **132**, 25-33 (2016).

224. Sungkaworn T, Jobin ML, Burnecki K, Weron A, Lohse MJ, Calebiro D. Single-molecule imaging reveals receptor-G protein interactions at cell surface hot spots. *Nature* **550**, 543-547 (2017).

225. Treppiedi D*, et al.* Single-Molecule Microscopy Reveals Dynamic FLNA Interactions Governing SSTR2 Clustering and Internalization. *Endocrinology* **159**, 2953-2965 (2018).

226. Hern JA*, et al.* Formation and dissociation of M1 muscarinic receptor dimers seen by total internal reflection fluorescence imaging of single molecules. *Proc Natl Acad Sci U S A* **107**, 2693-2698 (2010).

227. Sungkaworn T, Rieken F, Lohse MJ, Calebiro D. High-resolution spatiotemporal analysis of receptor dynamics by single-molecule fluorescence microscopy. *J Vis Exp*, e51784 (2014).

228. Keppler A, Gendreizig S, Gronemeyer T, Pick H, Vogel H, Johnsson K. A general method for the covalent labeling of fusion proteins with small molecules in vivo. *Nat Biotechnol* **21**, 86-89 (2003).

229. Kasai RS*, et al.* Full characterization of GPCR monomer-dimer dynamic equilibrium by single molecule imaging. *J Cell Biol* **192**, 463-480 (2011).

230. Iino R, Koyama I, Kusumi A. Single molecule imaging of green fluorescent proteins in living cells: E-cadherin forms oligomers on the free cell surface. *Biophys J* **80**, 2667-2677 (2001).

231. Seefeldt B*, et al.* Fluorescent proteins for single-molecule fluorescence applications. *J Biophotonics* **1**, 74-82 (2008).

232. Ambrose EJ. A surface contact microscope for the study of cell movements. *Nature* **178**, 1194 (1956).

233. Sun X*, et al.* Development of SNAP-tag fluorogenic probes for wash-free fluorescence imaging. *Chembiochem* **12**, 2217-2226 (2011).

234. Dorsch S, Klotz KN, Engelhardt S, Lohse MJ, Bunemann M. Analysis of receptor oligomerization by FRAP microscopy. *Nat Methods* **6**, 225-230 (2009).

235. Kaech S, Banker G. Culturing hippocampal neurons. *Nat Protoc* **1**, 2406-2415 (2006).

236. Wolter S*, et al.* rapidSTORM: accurate, fast open-source software for localization microscopy. *Nat Methods* **9**, 1040-1041 (2012).

237. Kiskowski MA, Hancock JF, Kenworthy AK. On the use of Ripley's K-function and its derivatives to analyze domain size. *Biophys J* **97**, 1095-1103 (2009).

238. Ester M, Kriegel H-P, Sander J, Xu X. A density-based algorithm for discovering clusters in large spatial databases with noise. . *In: Proceedings of the 2nd International Conference on Knowledge Discovery and Data Mining, Menlo Park, CA: AAAI, 226–231*, (1996).

239. Manders EMM, Verbeek FJ, Aten JA. Measurement of Colocalization of Objects in Dual-Color Confocal Images. *J Microsc-Oxford* **169**, 375-382 (1993).

240. Ibach J*, et al.* Single Particle Tracking Reveals that EGFR Signaling Activity Is Amplified in Clathrin-Coated Pits. *PLoS One* **10**, e0143162 (2015).

241. Pageon SV, Nicovich PR, Mollazade M, Tabarin T, Gaus K. Clus-DoC: a combined cluster detection and colocalization analysis for single-molecule localization microscopy data. *Mol Biol Cell* **27**, 3627-3636 (2016).

242. Corti C, Aldegheri L, Somogyi P, Ferraguti F. Distribution and synaptic localisation of the metabotropic glutamate receptor 4 (mGluR4) in the rodent CNS. *Neuroscience* **110**, 403-420 (2002).

243. Mateos JM, Azkue J, Sarria R, Kuhn R, Grandes P, Knopfel T. Localization of the mGlu4a metabotropic glutamate receptor in rat cerebellar cortex. *Histochem Cell Biol* **109**, 135-139 (1998).

244. Mishina M, Uemura T, Yasumura M, Yoshida T. Molecular mechanism of parallel fiber-Purkinje cell synapse formation. *Front Neural Circuits* **6**, 90 (2012).

245. Tanabe Y, Masu M, Ishii T, Shigemoto R, Nakanishi S. A family of metabotropic glutamate receptors. *Neuron* **8**, 169-179 (1992).

246. Iversen L*, et al.* Changes in metabotropic glutamate receptor mRNA levels following global ischemia: increase of a putative presynaptic subtype (mGluR4) in highly vulnerable rat brain areas. *J Neurochem* **63**, 625-633 (1994).

247. Schlick B, Flucher BE, Obermair GJ. Voltage-activated calcium channel expression profiles in mouse brain and cultured hippocampal neurons. *Neuroscience* **167**, 786-798 (2010).

248. Rancz EA, Hausser M. Dendritic calcium spikes are tunable triggers of cannabinoid release and short-term synaptic plasticity in cerebellar Purkinje neurons. *J Neurosci* **26**, 5428-5437 (2006).

249. Kulik A*, et al.* Immunocytochemical localization of the alpha 1A subunit of the P/Q-type calcium channel in the rat cerebellum. *Eur J Neurosci* **19**, 2169-2178 (2004).

250. San Paulo A, Garcia R. High-resolution imaging of antibodies by tapping-mode atomic force microscopy: Attractive and repulsive tip-sample interaction regimes. *Biophysical Journal* **78**, 1599-1605 (2000).

251. Reth M. Matching cellular dimensions with molecular sizes (vol 14, pg 765, 2013). *Nat Immunol* **15**, 205-205 (2014).

252. Jaqaman K*, et al.* Robust single-particle tracking in live-cell time-lapse sequences. *Nat Methods* **5**, 695-702 (2008).

253. Deisz RA, Billard JM, Zieglgansberger W. Presynaptic and postsynaptic GABAB receptors of neocortical neurons of the rat in vitro: differences in pharmacology and ionic mechanisms. *Synapse* **25**, 62-72 (1997).

254. Bonanno G, Raiteri M. Multiple GABAB receptors. *Trends Pharmacol Sci* **14**, 259-261 (1993).

255. Mateos JM*, et al.* Clustering of the group III metabotropic glutamate receptor 4a at parallel fiber synaptic terminals in the rat cerebellar molecular layer. *Neuroscience Research* **35**, 71-74 (1999).

256. DM VANE, Bos E, Pawlak JB, Overkleeft HS, Koster AJ, SI VANK. Correlative light and electron microscopy reveals discrepancy between gold and fluorescence labelling. *J Microsc* **267**, 309-317 (2017).

257. Ianoul A, Grant DD, Rouleau Y, Bani-Yaghoub M, Johnston LJ, Pezacki JP. Imaging nanometer domains of beta-adrenergic receptor complexes on the surface of cardiac myocytes. *Nat Chem Biol* **1**, 196-202 (2005).

258. Abitbol K, Acher F, Daniel H. Depression of excitatory transmission at PF-PC synapse by group III metabotropic glutamate receptors is provided exclusively by mGluR4 in the rodent cerebellar cortex. *Journal of Neurochemistry* **105**, 2069-2079 (2008).

259. Borodezt K, D'Mello SR. Decreased expression of the metabotropic glutamate receptor-4 gene is associated with neuronal apoptosis. *Journal of Neuroscience Research* **53**, 531-541 (1998).

260. Lorez M, Humbel U, Pflimlin MC, Kew JNC. Group III metabotropic glutamate receptors as autoreceptors in the cerebellar cortex. *Brit J Pharmacol* **138**, 614-625 (2003).

261. Han G, Hampson DR. Ligand binding to the amino-terminal domain of the mGluR4 subtype of metabotropic glutamate receptor. *J Biol Chem* **274**, 10008-10013 (1999).

262. Kurihara H*, et al.* Impaired parallel fiber-->Purkinje cell synapse stabilization during cerebellar development of mutant mice lacking the glutamate receptor delta2 subunit. *J Neurosci* **17**, 9613-9623 (1997).

263. Napper RMA, Harvey RJ. Number of Parallel Fiber Synapses on an Individual Purkinje-Cell in the Cerebellum of the Rat. *Journal of Comparative Neurology* **274**, 168-177 (1988).

264. Somogyi P, Dalezios Y, Lujan R, Roberts JD, Watanabe M, Shigemoto R. High level of mGluR7 in the presynaptic active zones of select populations of GABAergic terminals innervating interneurons in the rat hippocampus. *Eur J Neurosci* **17**, 2503-2520 (2003).

265. Shigemoto R*, et al.* Target-cell-specific concentration of a metabotropic glutamate receptor in the presynaptic active zone. *Nature* **381**, 523-525 (1996).

266. Kinzie JM, Saugstad JA, Westbrook GL, Segerson TP. Distribution of Metabotropic Glutamate-Receptor-7 Messenger-Rna in the Developing and Adult-Rat Brain. *Neuroscience* **69**, 167-176 (1995).

267. Lafon-Cazal M*, et al.* mGluR7-like metabotropic glutamate receptors inhibit NMDA-mediated excitotoxicity in cultured mouse cerebellar granule neurons. *European Journal of Neuroscience* **11**, 663-672 (1999).

268. Nakajima Y, Mochida S, Okawa K, Nakanishi S. Ca2+-dependent release of Munc18-1 from presynaptic mGluRs in short-term facilitation. *Proc Natl Acad Sci U S A* **106**, 18385-18389 (2009).

269. Schwenk J*, et al.* Modular composition and dynamics of native GABA receptors identified by high-resolution proteomics. *Nat Neurosci*, (2015).

270. Pooler AM, McIlhinney RAJ. Lateral diffusion of the GABA(B) receptor is regulated by the GABA(B2) C terminus. *Journal of Biological Chemistry* **282**, 25349-25356 (2007).

271. Lohse MJ, Hoffmann C, Nikolaev VO, Vilardaga JP, Bunemann M. Kinetic analysis of G Protein Coupled Receptor signaling using Fluorescence Resonance Energy Transfer in living cells. *Adv Protein Chem* **74**, 167-188 (2007).

272. Lohse MJ, Nuber S, Hoffmann C. Fluorescence/bioluminescence resonance energy transfer techniques to study G-protein-coupled receptor activation and signaling. *Pharmacol Rev* **64**, 299-336 (2012).

273. Borgdorff AJ, Choquet D. Regulation of AMPA receptor lateral movements. *Nature* **417**, 649-653 (2002).

274. Blanpied TA, Scott DB, Ehlers MD. Dynamics and regulation of clathrin coats at specialized endocytic zones of dendrites and spines. *Neuron* **36**, 435-449 (2002).

275. Varela JA, Dupuis JP, Etchepare L, Espana A, Cognet L, Groc L. Targeting neurotransmitter receptors with nanoparticles in vivo allows single-molecule tracking in acute brain slices. *Nat Commun* **7**, 10947 (2016).

276. Hioki H*, et al.* Efficient gene transduction of neurons by lentivirus with enhanced neuron-specific promoters. *Gene Ther* **14**, 872-882 (2007).

277. Kugler S, Kilic E, Bahr M. Human synapsin 1 gene promoter confers highly neuron-specific long-term transgene expression from an adenoviral vector in the adult rat brain depending on the transduced area. *Gene Ther* **10**, 337-347 (2003).

11 Acknowledgments

During the past four years, many people had contributed to the success of my PhD. First of all, I would like to express my sincere gratitude to my supervisor Prof. Davide Calebiro for introducing me to the world of bio-imaging. I appreciate his excellent scientific guidance, patience, and immense knowledge. I learned a lot from him, especially, critical thinking and attention to details. I am grateful to Dr. Marie-Lise Jobin for her valuable inputs in the projects. She was always available for scientific and personal discussions and to clarify any doubts. I would like to extend my thanks to Dr. Titiwat Sungkaworn and Dr. Amod Godbole for helping me out with the microscope setups, in addition to their help in all aspects during my work. Special thanks to Christin Misigaiski for her excellent technical assistance. Her help throughout the last year was tremendous and crucial to finish my PhD on time. I would also like to thank Dr. Kerstin Bathon for helping me in sorting out variable matters related to life in Germany. Thanks to Mariam Mahmoud, Bianca Klüpfel, Ines Elsner, Kerstin Seier, and all the previous and current members of the group for their help and for the stimulating environment. It was great sharing the laboratory with all of you.

In regards to the *d*STORM project, I thank Prof. Markus Sauer for his insightful comments during the thesis committee meetings and during other discussions that helped shaping the project. Thanks to Dr. Sarah Aufmkolk for the nice collaboration on this project and for her enthusiasm. Thanks to Prof. Heckmann for his comments during committee meetings.

Thanks to my dear husband, Ibrahim, his love and unlimited support were my driving force to perform experiments and write my thesis. I am indebted to my mother (Salwa) and siblings (Sahar, Sara, and Abdulrahman) for their love, emotional support, and encouragement throughout my life. A very special gratitude goes out to the organizers of the Sudanese researchers foundation. Especially to Dr. Rasha Elbasheir, Dr. Hisham Y. Hassan, Dr. Mohamed Hassan, Dr. Hisham Musa, Prof. Suad Elbdry, and Dr. Anwer Dafallah. Organizing variable activities and events with you was such a pleasure and so much fun. I have also learned a lot from all of you.

Thanks to the Graduate School of Life Sciences for the financial support. I am especially grateful to Dr. Gabriele Blum-Öhler, for her continuous support and kindness.

This thesis is dedicated to my father, senior engineer, Siddig Gamil.
I hope this work will honour the time that he spent in raising and teaching us. He is the reason I understand the value of hard work. I also dedicate this thesis to my precious bundle of joy, Nour, the sweat new addition to my family.